

HIGH-POWER OPTICALLY PUMPED SEMICONDUCTOR LASERS FOR NEAR
INFRARED WAVELENGTHS

by

Tsuei-Lian Wang

A Dissertation Submitted to the Faculty of the

DEPARTMENT OF OPTICAL SCIENCES

In Partial Fulfillment of the Requirements
For the Degree of

DOCTOR OF PHILOSOPHY

In the Graduate College

THE UNIVERSITY OF ARIZONA

2012

THE UNIVERSITY OF ARIZONA
GRADUATE COLLEGE

As members of the Dissertation Committee, we certify that we have read the dissertation
prepared by Tsuei-Lian Wang

entitled High-Power Optically Pumped Semiconductor Lasers for Near Infrared
Wavelengths

and recommend that it be accepted as fulfilling the dissertation requirement for the
Degree of Doctor of Philosophy

_____ Date: 08/03/12
Dr. Jerome V. Moloney

_____ Date: 08/03/12
Dr. R. Jason Jones

_____ Date: 08/03/12
Dr. Robert A. Norwood

Final approval and acceptance of this dissertation is contingent upon the candidate's
submission of the final copies of the dissertation to the Graduate College.

I hereby certify that I have read this dissertation prepared under my direction and
recommend that it be accepted as fulfilling the dissertation requirement.

_____ Date: 08/03/12
Dissertation Director: Jerome V. Moloney

STATEMENT BY AUTHOR

This dissertation has been submitted in partial fulfillment of requirements for an advanced degree at the University of Arizona and is deposited in the University Library to be made available to borrowers under rules of the Library.

Brief quotations from this dissertation are allowable without special permission, provided that accurate acknowledgment of source is made. Requests for permission for extended quotation from or reproduction of this manuscript in whole or in part may be granted by the author.

SIGNED: Tsuei-Lian Wang

ACKNOWLEDGEMENTS

It is a great pleasure to give respect to those who made this thesis possible.

First and foremost I would like to thank God for giving me strength and wisdom during this research and throughout my life.

I would like to express my sincere gratitude to my advisor, Prof. Jerome V. Moloney for his support and advice. His guidance helped me in all the time of research and writing of this dissertation.

I am also extremely indebted to Dr. Yushi Kaneda and Dr. J. M. Yarborough for their insightful comments and encouragements. They offer suggestions and helps whenever I need them. They are my teachers, mentors and friends.

I wish to thank all my colleagues, Dr. Jörg Hader, Dr. David Mathine, Dr. Colm Dineen, Dr. Alexandre Laurain, and Dr. Maik Scheller for the insights and experiences they shared. I would also like to thank Prof. Stephan W. Koch, Prof. Wolfgang Stolz, Dr. Bernardette Kunert, Celina Becker in Philipps University Marburg, Germany and Prof. Ganesh Balakrishnan and Dr. Chris Hains in University of New Mexico for all the helps.

My gratitude also goes to my dissertation committee: Prof. R. Jason Jones and Robert A. Norwood for their comments and advice on this dissertation.

I would like to thank Olli Nordman, Roxanne Pizano, Lacey Singh and Gail Varin for their assistance.

I would like to thank all my friends in “Calorie Community” for all the support, especially for letting me steal your birthday wishes. I thank my roommate, Yi-Ying for taking care of me in the last four years. I am grateful to Edward Chun-Neng Huang, who has inspired me in many ways for bringing me so many joys and encouragements.

Last but not the least, my deepest gratitude goes to my parents and my sister for their never-ending love and support throughout my life.

DEDICATION

To

My father Hsing-Hsung Wang

and

My mother Huei-Chin Kuo

TABLE OF CONTENTS

LIST OF FIGURES	8
LIST OF TABLES	13
ABSTRACT.....	14
CHAPTER 1 INTRODUCTION	16
1.1 History of OPSLs	17
1.2 The Principle of OPSLs	19
1.3 Types of OPSLs	23
1.3.1 Top emitters and bottom emitters	23
1.3.2 High power OPSLs and power scaling OPSLs.....	24
1.3.3 Long wavelength OPSLs and frequency converting OPSLs	26
1.3.4 Mode locked OPSLs	26
1.4 Dissertation Outline	28
CHAPTER 2 OPSL STRUCTURE DESIGN AND DEVICE FABRICATION	31
2.1 OPSL Structure	31
2.1.1 DBR	32
2.1.2 Active region.....	35
2.1.3 Micro-cavity.....	41
2.2 Device Fabrication	50
2.2.1 Bonding.....	50
2.2.2 Chemical wet etching.....	54
2.2.3 Structure characterization	57
CHAPTER 3 TEMPERATURE EFFECTS, THERMAL ANALYSIS AND OPTIMIZATION OF OPSLS.....	62
3.1 Power limiting mechanism.....	62
3.1.1 Temperature dependent effective gain of OPSLs	63
3.1.2 Auger recombination	65
3.1.3 Optical and thermal damage	67
3.2 Introduction of heat transfer in OPSLS	69
3.2.1 Heat transfer in solids (conduction).....	69
3.2.2 Convection.....	72
3.3 Thermal simulations.....	76
3.3.1 System geometry and boundary conditions	77
3.3.2 Heat source	79
3.3.3 Thermal optimization of high power OPSL devices	81
CHAPTER 4 HIGH POWER MULTI-TRANSVERSE MODE OPSLS.....	88
4.1 Experimental setup.....	88
4.1.1 Pump laser profile.....	89

TABLE OF CONTENTS - *Continued*

4.1.2 Ratio of pump beam spot size to laser TEM ₀₀ mode size.....	92
4.1.3 Double-pass/single pass gain	93
4.2 Room temperature detuning.....	95
4.3 Power scaling OPSLs.....	99
CHAPTER 5 EFFICIENCY IMPROVEMENT OF OPSLS.....	103
5.1 Double Pass Pump Design	103
5.2 Pump Anti-reflection Coating (PARC).....	108
CHAPTER 6 HIGH PEAK POWER OPERATION OF OPSLS	117
6.1 Experimental Setup	118
6.2 Results and Discussion.....	120
CHAPTER 7 HIGH POWER TEM ₀₀ MODE OPERATION	124
7.1 Optical Resonator Design	124
7.2 Experimental Setup	132
7.3 Results and Discussion.....	134
CHAPTER 8 CONCLUSION AND OUTLOOK.....	137
REFERENCES	142

LIST OF FIGURES

FIGURE 1.1 OPSL structure and principle of OPSLs.....	20
FIGURE 1.2 Schematic set-up of an OPSL.....	22
FIGURE 1.3 A V-shaped cavity with nonlinear crystal for frequency doubling.	22
FIGURE 1.4 Structures of a surface emitter and a bottom emitter.....	24
FIGURE 1.5 Schematic set-up of (a) an passively mode locked OPSL and (b) a MIXSEL	28
FIGURE 2.1 Two DBR designs for 1040 nm OPSL	34
FIGURE 2.2 (A) AlAs/GaAs DBR (B)AlAs/AlGaAs DBR	35
FIGURE 2.3 Band gap energy and optical intensities of the pump and the laser within the active region of the in-well pumped structure.	36
FIGURE 2.4 OPSL structure for 1040 nm laser operation.....	38
FIGURE 2.5 Left: computed gain with varied carrier densities at 300 K; Right: computed gain at varied structure temperature with carrier density $3.1 \times 10^{12} \text{ cm}^{-1}$	41
FIGURE 2.6 (a) Transmission and reflection at an interface. (b) Propagation through a layer.....	42
FIGURE 2.7 (a) computed reflectivity spectrum without excitation; (b) computed reflectivity spectrum with varied carrier densities at 325 K.....	48
FIGURE 2.8 Blue: calculated QW absorption. Green: the confinement factor. Red: Reflectivity spectrum. The temperature of the structure is at 325 K and the carrier density is $0.05 \times 10^{12} \text{ cm}^{-1}$	48
FIGURE 2.9 Longitudinal mode and the refractive index distribution inside the OPSL structure.....	49
FIGURE 2.10 Flow diagram of the fabrication processes.....	49

LIST OF FIGURES - *Continued*

FIGURE 2.11 Ultrasound imaging of bonded chip. (a) voids in solder junction (b) void-free solder junction	51
FIGURE 2.12 Vacuum bonding station.....	52
FIGURE 2.13 Temperature setting for semiconductor-heat spreader bonding	52
FIGURE 2.14 OPSL device soldered on the copper submount.....	53
FIGURE 2.15 Stirring fixture	54
FIGURE 2.16 (a) Surface profile of substrate removed semiconductor chip. (b) 1-D surface height plot.....	55
FIGURE 2.17 Reflectivity spectrum measured at 120 °C. The dip wavelength of the OPSL structure vs. etching time after the GaAs substrate is totally removed as an inset is shown.	56
FIGURE 2.18 TDR of 1010 nm OPSL device	57
FIGURE 2.19 (a) Measured sPL and calculated sPL for OPSL at 10 °C and low carrier density. The calculated material PL and the filter function are also shown. (b) Measured sPL and calculated sPL for OPSL at 10 °C and 40 °C.....	60
FIGURE 3.1 Mechanisms of Auger recombination processes: (a) CHCC process and (b) CHHH process.	65
FIGURE 3.2 Carrier loss currents per well at 275 K (black) and 375 K (grey) divided by the density squared. The thick dashed lines represent Auger recombination loss.....	66
FIGURE 3.3 (a) Solder voids and thermal damage (b) crossed-crack damage	68
FIGURE 3.4 Water heat sink. Left: heat sink body without the copper submount. Right: heat sink with the copper submount and an OPSL device.....	73
FIGURE 3.5 Flow regimes associated with impingement of a circular submerged jet....	74

LIST OF FIGURES - *Continued*

FIGURE 3.6 Geometry and standard parameters used for thermal simulations.....	76
FIGURE 3.7 Transverse profiles of heat sources. (a) Normalized Gaussian, super-Gaussian and uniform pump profile with a radius of 250 μm (b) Heat flux profiles of Gaussian, super-Gaussian and uniform pump source with a power of 100 W	79
FIGURE 3.8 Radial temperature distribution of OPSL devices pumped by uniform beam, super-Gaussian beam and Gaussian beam	80
FIGURE 3.9 Simulated pump spot size dependent center temperature. The pump power density is fixed at 191 W/mm^2 for all pump sizes.	82
FIGURE 3.10 Simulated pump spot size dependent center temperature. (a) Center temperature in OPSL devices with various diamond widths (b) Center temperature in OPSL devices with various diamond thicknesses.....	83
FIGURE 3.11 Simulated pump size dependent temperature in devices with different indium solder thickness.....	84
FIGURE 3.12 Simulated pump size dependent temperature in OPSL devices soldered on the copper submount for different thicknesses of the indium solder	85
FIGURE 3.13 Simulated pump size dependent temperature in OPSL devices soldered on copper submount with various thicknesses and temperature in the OPSL device soldered on a copper submount with side cooling design.	87
FIGURE 3.14 Copper submount with a recess for side cooling.....	87
FIGURE 4.1 Schematic setup of OPSLs	89
FIGURE 4.2 (a) Intensity profile of Apollo laser. (b) Left: intensity profile of DILAS laser. Right: Intensity profile of DILAS laser with fiber bending	90
FIGURE 4.3 Power performance of the OPSL device pumped by two lasers with different contribution. (a) Before altering intensity profile of the DILAS laser. (b) After altering intensity profile of the DILAS laser.	91

LIST OF FIGURES - *Continued*

FIGURE 4.4 Power performance of OPSLs with different ratios of the pump radius to the mode radius.....	93
FIGURE 4.5 A V-shaped cavity for double passing the OPSL gain.....	94
FIGURE 4.6 Maximum output power achieved using different output coupling.	95
FIGURE 4.7 Temperature dependent reflectivity of three OPSL devices from three different wafers.	97
FIGURE 4.8 Output performance of the OPSL devices with different amount of detuning.	98
FIGURE 4.9 (a) Power scaling of 1040 nm OPSLs. Solid bold lines: experiment; thin dashed line: theory. (b) Power density curves in W/mm^2	101
FIGURE 4.10 Output performance of the over-etched OPSL device pumped by a $920 \mu m$ spot from a single 808 nm fiber-coupled laser.....	102
FIGURE 5.1 Left: calculated power characteristic curves for OPSLs with 80% and 100% pump absorption in the active region. Right: calculated power characteristic curves of OPSLs with different numbers of QWs.....	104
FIGURE 5.2 The OPSL structure with the double pass pump design.....	106
FIGURE 5.3 Output performance of OPSL devices with/without the double pass pump design.	107
FIGURE 5.4 Refractive index profile (blue) and 1040 nm lasing mode (red) for an OPSL operating at 1040 nm at 375 K.....	109
FIGURE 5.5 Input-output curves of an OPSL device with and without a LARC.....	111
FIGURE 5.6 Refractive index profile (blue) and 1040nm lasing mode (red) for an OPSL operating at 1040 nm at 375 K (a) with a quarter wavelength thick anti-reflection coating for the pump wavelength at 808 nm (b) with three quarter wavelength thick anti-reflection coating for the pump wavelength at 808 nm (the new PARC).....	112

LIST OF FIGURES - *Continued*

FIGURE 5.7 TDR of the OPSL device with and without the $\frac{3}{4} \lambda$ PARC.	114
FIGURE 5.8 Output characteristics versus total pump power for an OPSL device with and without the $\frac{3}{4} \lambda$ PARC. The device was tested by using an 8 cm-linear cavity with a concave output mirror with 10 cm radius of curvature. The pump spot was 820 μm in diameter and the heat sink temperature was 10 $^{\circ}\text{C}$	115
FIGURE 6.1 Experimental setup for the OPSL pumped by an alexandrite laser.	117
FIGURE 6.2 Power performance of OPSL in CW and pulsed operation.	119
FIGURE 6.3 OPSL performances for different cavity configuration. Inset: 830 ns (FWHM) pump pulse (olive), the OPSL pulsewidth is 750 ns (pink).	121
FIGURE 6.4 OPSL output with over 270 W peak power.	122
FIGURE 7.1 Linear optical resonator.	126
FIGURE 7.2 Left: Z-shaped telescopic resonator. Right: equivalent linear resonator. ...	128
FIGURE 7.3 The equivalent telescopic resonator with a thin telescope and a thin lens f_T located at the mirror 2.	129
FIGURE 7.4 The telescope mirror spacing and corresponding mode diameter vs. L for $g_1 g_2 = 0.5$. The radii of curvature for R_{T1} , R_{T2} and R_1 are 50 mm, 350 mm, and infinity, respectively.	131
FIGURE 7.5 Experimental setup for the OPSL in TEM_{00} mode operation.	132
FIGURE 7.6 Left: pump and the cavity mode profile in the x-direction. Right: pump and the cavity mode profile in the y-direction.	133
FIGURE 7.7 Input-output curves of the OPSL device with pump diameter $D_{\text{pump}} = 590, 730$ and $880 \mu\text{m}$	134
FIGURE 7.8 M^2 fitting of the 27 W OPSL beam. Inset: intensity profile of the OPSL beam.	136

LIST OF TABLES

TABLE 3.1 Parameters for heat transfer coefficient calculation.....	78
---	----

ABSTRACT

Optically pumped semiconductor lasers (OPSLs) combine features including an engineerable emission wavelength, good beam quality, and scalable output power and are desirable for a wide variety of applications. Power scaling of OPSLs requires a combination of accurate epitaxial quantum design, accurate wafer growth and good thermal management. Here a fabrication process for OPSL devices was developed to ensure efficient OPSL device cooling and minimum surface scattering. A systematic thermal analysis was performed to optimize thermal management. Strategies for optimizing power extraction were developed; including increasing the gain/micro-cavity detuning that increases the threshold but also increases the slope efficiency and the roll-over temperature, recycling the excess pump via reflection from a metalized reflector at the back of a transparent DBR, anti-reflection coating at the pump wavelength while preserving the signal micro-cavity resonance.

With optimized thermal management and the strategy of using large gain/micro-cavity detuning structure, a CW output power of 103 W from a single OPSL device was achieved. 42% optical-to-optical efficiency from the net pump power was obtained from the OPSL device with the double pass pump design and 39% optical-to-optical efficiency with respect to the total pump power was obtained with the new pump anti-reflection coating. For the fundamental mode operation, over 27 W of CW output power was achieved. To our knowledge, this is the highest 1 μm TEM₀₀ mode power reported to date for an OPSL. Finally, strategies for generating high peak power are also discussed. A

maximum peak power of over 270 W was achieved using 750 ns pump pulses.

CHAPTER 1 INTRODUCTION

Since the first demonstration of lasers, they have been used for applications in a wide variety of fields, including consumer electronics, communication, sciences, biomedical instruments, industry, entertainment, the military and many others. For example, the laser disc player (CD, DVD and Blue-ray) was the first successful laser-based consumer product and is used in almost every household. Nowadays, the Internet has become a necessity in modern society and, optical fiber networking technology using lasers enables fast data transmission. Another widespread laser application is the barcode scanner commonly seen in stores. Each of these applications requires a particular combination of laser properties, such as emission wavelength, wavelength tunability, optical power, output efficiency, beam quality and high-speed modulation. The optically pumped semiconductor laser (OPSL), a fairly recent category of semiconductor lasers, combines features including an engineerable emission wavelength which can be tailored over a wide range, good beam quality, and scalable output power and thus becomes a good candidate for a variety of applications where either continuous wave (CW) or ultra-fast pulses are required. In this chapter we give a brief introduction to OPSLs including their history, basic principles and different application types.

1.1 History of OPSLs

In the early development of semiconductor lasers the active medium, which is a homojunction structure or a heterojunction structure had very low efficiency [1, 2]. The lasing threshold was high and operation was restricted to pulsed mode at a low temperature. To solve this problem, a double heterostructure (DHS) was proposed [3]. The DHS is a structure with a layer of low bandgap material sandwiched between two high bandgap layers. This structure provides for carrier confinement and optical confinement meaning that the injected electrons and holes are confined in a narrow region where the optical field is also confined. Therefore, much lower threshold current is required in DHS lasers and continuous wave operation at room temperature was achieved. The next milestone in the history of the development of semiconductor laser structures is the invention of quantum well (QW) structures [4]. It was found that if the active layer was thin enough the electron levels would be split apart. By changing the thickness of the active layer, the wavelength of QW lasers can be tuned, thus bringing a most advantageous property to recent semiconductor lasers.

In terms of emission direction, conventional semiconductor lasers have two general configurations that require different growth approaches: edge emitters (in-plane lasers) and surface emitters. In the edge emitter, light is confined by an optical waveguide in the growth direction and index-guided or gain guided in the lateral direction [5]. The output of an edge-emitter is asymmetric and highly divergent. In order to obtain single transverse mode operation, a small waveguide dimension is required which leads to a limited output power of a few hundred milliwatts. In addition, such a small area creates a

high optical power density at the emitting facet leading to catastrophic optical damage (COD) [6]. By using wide-strip lasers, the output power can be scaled up to tens of watts but only with highly multi-transverse modes. In contrast, vertical cavity surface emitting lasers (VCSELs) emit optical output in the growth direction and the output of VCSELs is symmetric and much less divergent than for edge-emitters. Similar to edge-emitters, the output power of VCSELs is limited by the small output diameter that is required for single transverse mode operation. Novalux extended-cavity surface-emitting laser (NECSEL) technology [7], on the other hand, uses an extended cavity/an external output mirror to control the optical mode so it enables a laser beam diameter of hundreds of microns which is an order-of magnitude larger than for traditional VCSEL designs. The large diameter of the output beam also prevents the semiconductor chip from COD. Although an external mirror can control the laser transverse mode for a larger output beam diameter, uniformly injecting current over such a large area is very difficult. The output power in single transverse mode operation is only about 500 mW from a single NECSEL device [8]. Therefore, in brief, it is very difficult to simultaneously achieve high power and circular, single transverse mode output with conventional edge-emitters or NECSELs.

OPSLs, which were first demonstrated in 1997 [9], are not limited in this respect since optical pumping provides scalable, uniform pump power while the external cavity controls the laser mode leading to a high power output (tens of watts) with near-diffraction-limited beam quality. Moreover, the semiconductor materials in the OPSL structure are undoped so the optical loss due to free carrier absorption is reduced. Thanks

to the broad absorption band of semiconductors, the optical pump source needs can adopt a broad wavelength range. The flexible wavelength choice of the pump laser gives the OPSL a big advantage compared to conventional solid state lasers. The latter only can be efficiently pumped by a wavelength that matches an absorption band. Many of these advantages make the OPSL a suitable laser choice for a wide variety of applications. For example, the circular output beam with a small divergence angle and large continuous mode-hop free tuning range make OPSLs suitable for intra-cavity laser absorption spectroscopy (ICLAS) [10, 11]. The OPSL is also an excellent choice for laser cooling as it provides a wide range of wavelength choices for energy transitions of different atomic systems [12, 13]. In life science applications, the OPSL is a good light source for flow cytometry, microscopy, diagnostic imaging or genomics because of its good beam quality and low noise [14]. High brightness green or blue light generated by frequency doubling a NIR-OPSL is a good candidate for display or light show purposes [15]. OPSLs have been improved over the last decade and have showed the world their unique, remarkable properties. It is believed that the future OPSL will be able to provide wider emission wavelength coverage, a higher CW output power up to hundreds of watts, faster output pulses with higher average power and still maintain excellent beam quality. There is no doubt that OPSL will be a major laser source in the future.

1.2 The Principle of OPSLs

The three important components in a laser are the gain medium, the pump source and the optical resonator. In the OPSL system, the gain medium is the active region

inside the OPSL structure. The active region consists of the quantum wells placed between the pump-absorbing barrier layers which have higher bandgap energy than the QWs. Usually, the separation of QWs is a half wave of the laser wavelength so that QWs are at the standing wave antinodes of the laser wavelength. This structure is referred to as a resonant periodic gain (RPG) structure [16]. In this case, gain is wavelength selective and is enhanced because of an enhanced light field-QWs interaction. Fig. 1.1 shows an OPSL system and the basic principle of operation [17]. Since the barriers are much thicker than the quantum wells, most of pump energy is absorbed in the barriers. This pumping technique is referred to as barrier pumping and details are discussed in chapter 2. The electron-hole pairs created in the barriers diffuse and recombine, emitting photons in the quantum wells.

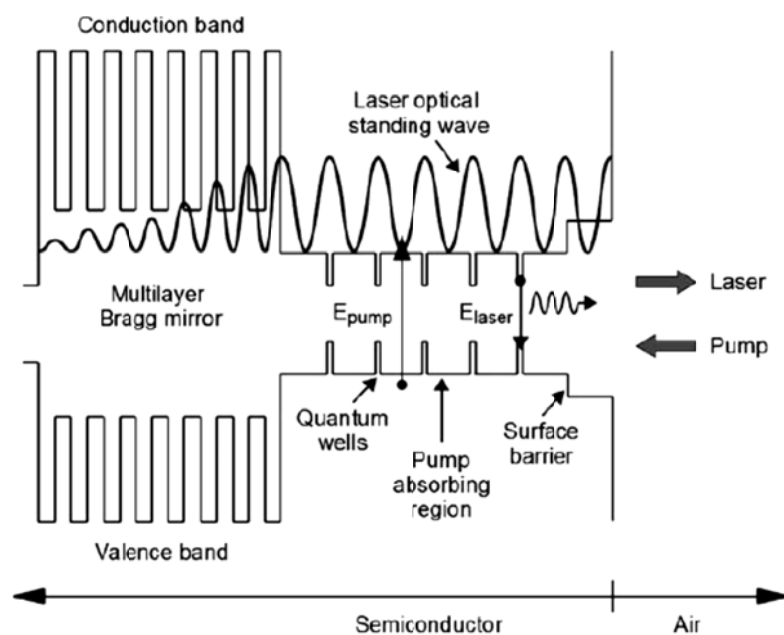


FIGURE 1.1 OPSL structure and principle of OPSLs

The common pump configuration of the OPSL is a fiber-coupled pump beam from a multi-mode fiber-coupled diode stack expanded and imaged onto the OPSL device at a small angle of incidence (Fig. 1.2). The pump optics usually contains a collimator lens and an imaging lens. The pump spot size on the OPSL device can be easily scaled by changing the focal length of the imaging lens. As mentioned earlier, the wide absorption band of the barrier layer enables a flexible choice of pump lasers, but usually the barrier is designed and engineered to absorb a specific laser wavelength which is cheap, and easily accessible.

The optical resonator in the OPSL system is formed between the distributed Bragg reflector (DBR) inside the OPSL structure and one or more external mirrors as shown in Fig. 1.2 and Fig. 1.3. The DBR consists of layer pairs of quarter wavelength layers with high and low refractive index resulting in a high reflectivity at the designed wavelength. The output coupling of the OPSL system is determined by the external mirror while the laser beam quality is determined by the aperture size of the pump area and the resonator geometry. The fundamental transverse mode size is chosen to match the pump spot size on the OPSL chip to achieve single transverse mode operation. Optical resonator configurations having more than one external mirror, such as V-shaped and Z-shaped cavities provide flexibility for inserting intra-cavity elements [18-20]. Fig. 1.3 shows an example of a V-cavity with a nonlinear crystal for frequency doubling. Inside the first arm of the V-cavity are a birefringent filter and an etalon for wavelength selection. In the other arm, the nonlinear crystal is placed close to the flat end mirror so that the resonator mode size is ideally small resulting in large optical intensity inside the

crystal for efficient conversion.

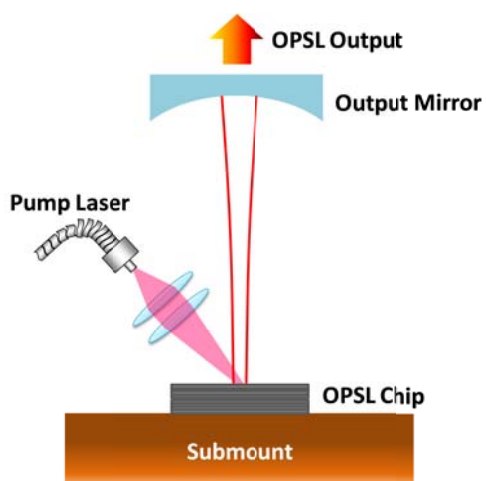


FIGURE 1.2 Schematic set-up of an OPSL

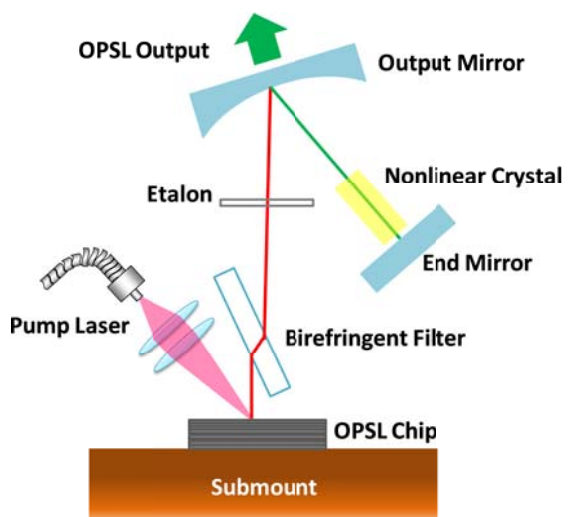


FIGURE 1.3 A V-shaped cavity with nonlinear crystal for frequency doubling.

1.3 Types of OPSLs

For different applications, OPSLs provide many key advantageous properties, including high power output, operating wavelength from UV to NIR, and ultra-fast short pulsed operation. In this section, the various forms of OPSLs are introduced and discussed and recent progress is reviewed.

1.3.1 Top emitters and bottom emitters

Based on the growth order of the epitaxial layers, OPSLs are of two types: top emitters or bottom emitters. If the DBR is the first layer grown on the substrate (bottom), followed by the active region and cap layer, this structure is called a top emitter (Fig. 1.4). On the other hand, if the cap layer or the etch-stop layer is first grown on the substrate, followed by the active region and the DBR, this structure is referred to as a bottom emitter. Usually, top emitters and bottom emitters require different fabrication processes in order to efficiently remove the dissipated heat which is the major parameter limiting the OPSL output power. In the bottom emitter geometry, the semiconductor chip is first bonded to a heat spreader which has high thermal conductivity, and then the substrate is removed by chemical etching; the processed bottom emitter device has a thickness of few microns. During laser operation, the heat transfer path is through the DBR and the heat spreader to the heat sink. For top emitters, the additional processing for removing the entire substrate is not necessary. The common thermal management used for top emitters is capillary bonding or directly contacting a transparent heat spreader to the cap layer which has a thickness of a few hundred nanometers. In this case, the heat transfer

pathway is much shorter than the case in bottom emitters so the heat removal efficiency should be better in top emitters. However, so far, the reported output performance of bottom emitters is much better than top emitters, indicating relatively poor contact between the semiconductor and the heat spreader, potential degradation of the contact at high power densities and relatively poor heat sinking due to reduced heat sink volume. In addition, the additional dielectric layer causes multiple reflections inside the heat spreader and also changes the standing wave pattern inside the semiconductor structure. Consequently, the output performance of OPSLs may be affected.

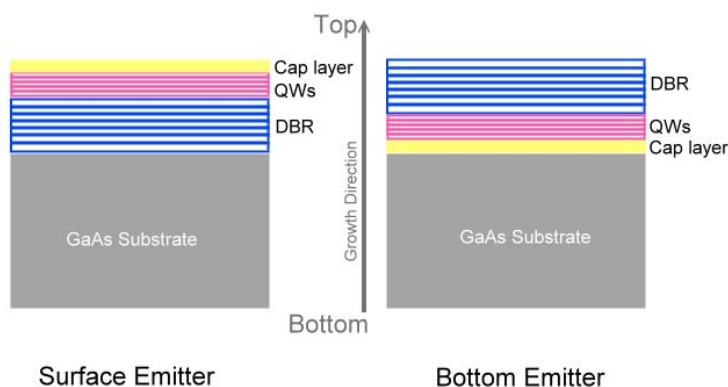


FIGURE 1.4 Structures of a surface emitter and a bottom emitter

1.3.2 High power OPSLs and power scaling OPSLs

The first demonstrated high power OPSL showed $>0.5\text{W CW}$, near diffraction limited output and power scalability. The concept of power scaling is to increase the pump area while maintaining a constant power density to obtain a higher output power.

The uniform optical pumping and the optical resonator geometry enable scaling of the pump and the laser mode size separately leading to a high power output with good beam quality. In semiconductor lasers, the output performance is usually limited by heating and catastrophic optical damage. Since the pump size is usually much larger than the OPSL structure thickness, the major heat flow direction is vertically through the thin OPSL structure to the heat sink at its back. Nearly one-dimensional heat transfer in the direction perpendicular to the pump plane enables enlarging the pump area without affecting the cooling efficiency. With good thermal management, OPSL output scaling from a pump spot over several hundred microns has been demonstrated [21-25]. Chilla et al. demonstrated nearly 30 W of CW output power from a single OPSL chip in 2004 [21]. This laser was running with an M^2 around 3 and of wavelength of 980 nm and 920 nm. In 2008, Rudin et al. used a 480 μm diameter pump spot to achieve over 20 W of CW output power in a fundamental transverse mode ($M^2 < 1.1$) at 960 nm [24]. However, the heat sink temperature in this system was at $-20\text{ }^\circ\text{C}$.

When further power scaling is limited by excess heating, higher output power can be achieved by increasing the number of OPSL chips in the optical resonator [26-28]. In this scenario, each OPSL device is cooled separately so the cooling efficiency is improved. Moreover, the thermal lensing effect in OPSL is negligible [23] and hence positioning multiple OPSL chips in one optical resonator can be easily achieved. In 2007 Chilla et al. achieved over 50 W output at 532 nm by using three OPSL chips [23]. The output beam quality was excellent with M^2 less than 1.3. Multimode output power exceeding 60 W was also shown in this geometry.

1.3.3 Long wavelength OPSLs and frequency converting OPSLs

Research activities in OPSLs are mainly focused on InGaAs/AlGaAs based structures emitting around 1 μm . There is also some interest in InGaNAs and InGaPAs based OPSLs emitting at 1.3 μm and 1.5 μm for optical fiber communication [29, 30]. A Sb-based material system enables OPSL to access the 2-2.5 μm region which is of particular interest for eye-safe remote sensing [31-33]. However, the output power is much lower compared to InGaAs/AlGaAs based structure. Recently, OPSLs emitting at longer wavelength (4.5-5 μm) using narrow bandgap IV-VI (lead-chalcogenide) materials have also been reported [34, 35]. CW power over 16 mW was demonstrated [34].

OPSLs can further expand their spectral coverage by intra-cavity frequency conversion. For example, it is important to use “real” red–green–blue (RGB) wavelengths of 620, 532, and 460 nm, respectively, for displays. Therefore, green and blue lasers obtained from intra-cavity second harmonic generation of 1064 and 920nm InGaAs/GaAs based OPSLs have been developed very intensely over the past few years [15, 36]. Moreover, frequency doubling of 976 nm OPSLs can replace the inefficient Argon laser at 488 nm [21, 37, 38]. OPSLs are also the best candidate of efficient yellow-orange lasers around 580-590 nm where no effective light sources are available [19].

1.3.4 Mode locked OPSLs

Ultrafast lasers provide enormous potential for applications in science and technology. Particular applications include optical clocking of microprocessors [39, 40], throughputs in computer interconnects [41], sensing and imaging of biological processes,

and metrology. Currently, most of these applications rely on Ti-sapphire lasers that require a pump wavelength in the green spectral range making the laser system complex and expensive. The passively mode-locked OPSL which has a semiconductor saturable absorber mirror (SESAM) in the optical resonator to generate self-starting mode-locked pulses has been proposed as a new candidate ultrafast laser source. The first demonstration of a passively mode-locked OPSL in 2000 reported 21.6 mW in 22-ps pulses at a repetition rate of 4 GHz [42]. This mode-locked laser emits at 1030 nm. Since then, improvements in thermal management and SESAM design have been made. In 2012, our group demonstrated a passively mode-locked OPSL emitting at 1030 nm with 682 fs duration at 1.71 GHz with 5.1 W average output power which is the highest average power reported so far [43]. In this case, we found an irrecoverable reduction of output power due to the damage of the SESAM. Further improvements are expected by using a larger laser mode size on the SESAM to keep optical intensity below damage threshold of the SESAM.

The idea of integration of both the laser gain and saturable absorber into a single semiconductor structure was proposed in 2007 (Fig. 1.5) [44]. This new device is referred as a MIXSEL (mode-locked integrated external-cavity surface emitting laser). In the latest report, 28-ps pulses at a repetition rate of 2.5 GHz with 6.4 W average output power at 959 nm was achieved [45]. The output beam of this system also showed very good transverse mode quality ($M^2 < 1.05$). From the review above, the mode-locked OPSL has shown itself to be a candidate for a new generation of ultrafast lasers that are sufficiently compact, robust, reliable and cost-effective to enjoy widespread use.

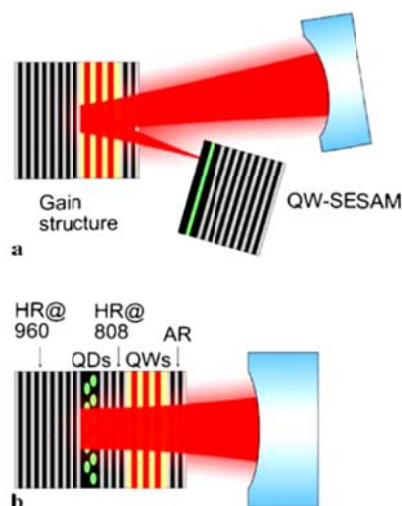


FIGURE 1.5 Schematic set-up of (a) an passively mode locked OPSEL and (b) a MIXSEL

1.4 Dissertation Outline

In chapter 1, the key features and the applications of OPSELs are introduced. The basic principles of OPSEL operation are discussed. We then review the progress of different OPSEL characteristics including high power OPSELs, long wavelength OPSELs, frequency-doubled OPSELs and ultrafast OPSELs.

Chapter 2 focuses on structure design, gain modeling, and device fabrication of OPSELs. The OPSEL structure used in this dissertation is introduced. The full microscopic design and theoretical modeling are discussed. We then discuss in detail the process of semiconductor chip-flip bonding and substrate removal, which are both critical to high power operation. In the final part of this chapter, the OPSEL structure is analyzed using temperature dependent reflectivity (TDR) spectra, and surface photoluminescence

spectrum (sPL).

Chapter 3 focuses on temperature effects on OPSL performance and thermal management for a high power OPSL. The power limiting mechanism and the power scalability of OPSLs are discussed. We then look in detail at the parameters affecting thermal management and present the thermal management scheme used here for high power operation and power scaling.

In chapter 4, the experimental setup and the optical resonator design for high power multi-transverse mode operation are discussed. The influence of room temperature detuning on the OPSL performance is investigated. The characteristics of three OPSL structures with different amounts of detuning are shown and their lasing threshold, optical power, and output efficiency are compared. Experimental results of power scaling OPSLs are presented.

Chapter 5 presents approaches for improving the optical efficiency and external efficiency of OPSLs. A double-passed pump scheme is used for improving differential efficiency and the structure is described. The output performance of structures with and without double-passing pump design is compared. The effects of anti-reflection (AR) dielectric coating on the surface of the OPSL on laser performance are also discussed in this chapter. Characteristics of OPSL devices with two different AR coating designs are introduced and their lasing performance is compared.

In Chapter 6, we present an OPSL with high peak power operation. The OPSL device is pumped by a 755 nm alexandrite laser. The optimization strategies for extracting high peak power pulses and the limitation of output power are discussed.

Chapter 7 presents a high power OPSL in single transverse mode operation. The experimental setup and the optical resonator design are discussed. Experimental results of power scaling OPSLs in the fundamental transverse mode are presented.

Chapter 8 concludes the dissertation, summarizes the achievements and provides the possible optimizations.

CHAPTER 2 OPSL STRUCTURE DESIGN AND DEVICE FABRICATION

An OPSL structure is essentially a complex multi-layer semiconductor structure with three functional regions: the distributed Bragg reflector (DBR), the active region, and the cap layer having high band-gap energy to prevent non-radiative recombination at the structure surface. The semiconductor materials, the thickness, the number of layers and the relative position of each layer in the OPSL structure determine the OPSL characteristics including the absorption/gain, emission wavelength, and the effective gain. The fabrication of an OPSL device, which is a substrate-removed OPSL structure mounted on a heat spreader, usually includes two major processes: flip-chip bonding and chemical etching. Both processes are important to OPSL performance since the solder junction between the semiconductor chip and the heat spreader affects the heat removal efficiency which is the key to high power generation. The surface quality and the thickness of the cap layer after chemical etching affects the surface scattering loss and the emitting wavelength. In this chapter the structure design, fabrication, and characterization of OPSL devices are discussed.

2.1 OPSL Structure

The OPSL structure discussed here is an InGaAs/GaAs based structure for high power generation at a near-infrared wavelength (1 μm). The factors affecting the structure design include increasing efficiency, maximizing the optical gain at the desired wavelength and minimizing the optical loss at the DBR. Three important aspects of the

OPSL structure design are usually followed for efficient OPSL operation:

1. DBR needs to have high reflectivity ($> 99\%$) at the designed laser wavelength.
2. Quantum wells are placed at the standing wave antinodes of the designed laser wavelength inside the OPSL structure.
3. The resonance of the micro-cavity formed between the DBR and the semiconductor-air interface matches to the quantum well gain peak at the designed wavelength and temperature for effective gain enhancement.

Based on these three concepts, the design and theoretical modeling of OPSL structures used in this dissertation are introduced in the following sections.

2.1.1 DBR

The DBR serving as a mirror in the OPSL resonator consists of an alternating sequence of high and low refractive index layers with quarter wavelength thickness. The mirror reflectivity, R is affected by the number of high and low refractive index layer pairs and the index contrast between the two materials. The refractive index contrast also determines the bandwidth of reflectivity of the stopband, $\Delta\lambda_{\text{DBR}}$ [46]:

$$R = \frac{\left[1 - \left(\frac{n_e}{n_o}\right) \left(\frac{n_{low}}{n_{high}}\right)^{2N}\right]^2}{\left[1 + \left(\frac{n_e}{n_o}\right) \left(\frac{n_{low}}{n_{high}}\right)^{2N}\right]} \quad (2.1)$$

$$\Delta\lambda_{DBR} = \frac{4\lambda_c}{\pi} \sin^{-1} \left(\frac{1 - \left(\frac{n_{low}}{n_{high}}\right)}{1 + \left(\frac{n_{low}}{n_{high}}\right)} \right) \quad (2.2)$$

n_o , n_e , n_{low} and n_{high} are the refractive indices of the original material (the material in front of the first layer of the DBR), exiting material (the material next to the last layer of the DBR), and two DBR materials. N is the number of repeated pairs of two alternating materials and λ_c is the designed central wavelength of the stopband. From (2.1), increasing the number of periods leads to a higher DBR reflectivity. However, it also increases the entire DBR thickness resulting in a longer heat transfer path thereby reducing heat removal efficiency. As a result, a minimum number of periods is usually desired to achieve a given reflectivity.

Fig. 2.1 shows the DBR designed for a 1040 nm OPSL used in this study. We use different material combinations for the DBR in two separate structure designs. The first design uses 20 AlAs ($n=2.95$) and GaAs ($n=3.49$) pairs. The AlAs layers and GaAs layers are with thickness:

$$d_{AlAs} = \frac{1040 \text{ nm}}{4 \times n_{AlAs}} = 88.1 \text{ nm}$$

$$d_{GaAs} = \frac{1040 \text{ nm}}{4 \times n_{GaAs}} = 74.3 \text{ nm}$$

The second design uses 20 AlAs ($n=2.95$) and AlGaAs ($n=3.46$) pairs. The $\text{Al}_{0.2}\text{Ga}_{0.8}\text{As}$ layers have thickness:

$$d_{\text{AlGaAs}} = \frac{1040 \text{ nm}}{4 \times n_{\text{AlGaAs}}} = 75 \text{ nm}$$

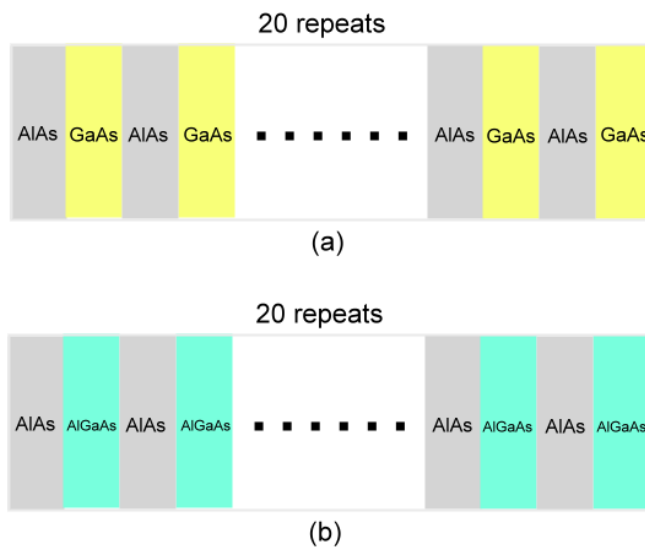


FIGURE 2.1 Two DBR designs for 1040 nm OPSL

Fig. 2.2 shows the simulated reflectivity spectrum of two DBR designs. A DBR structure with higher index contrast has higher reflectivity so the AlAs/GaAs DBR has higher reflectivity than the AlAs/AlGaAs DBR for the same number of periods. However, GaAs absorbs pump light at 808 nm resulting in heating and a lower output efficiency. The OPSL performance of the OPSL with an AlAs/AlGaAs DBR for the double pass

pump scheme is discussed in detail in the chapter 5.

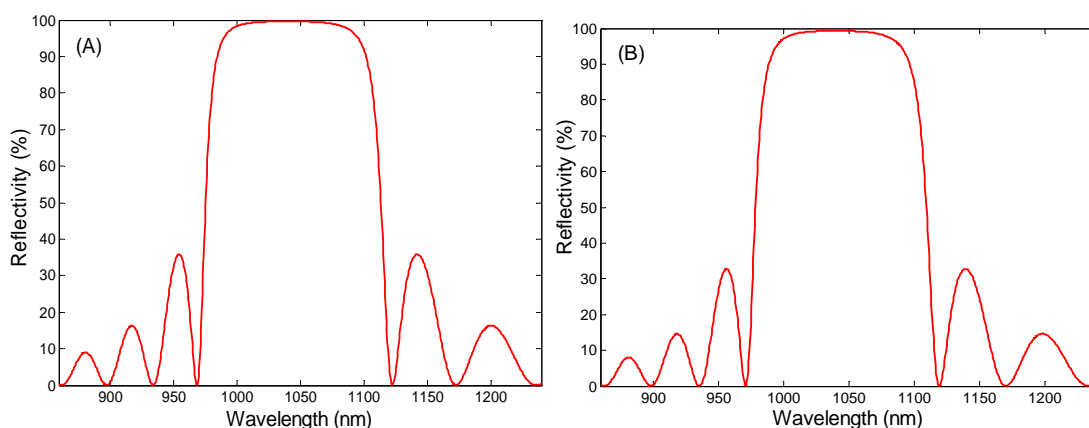


FIGURE 2.2 (A) AlAs/GaAs DBR (B) AlAs/AlGaAs DBR

2.1.2 Active region

The active region is the functional region where pump-laser energy conversion involving pump absorption, carrier production and carrier recombination takes place. There are two active region configurations in terms of the pumping approaches: in-well pumping and barrier pumping. For in-well pumping, pump light is absorbed in the QWs creating electron-hole pairs that also recombine in the QWs. In this case, the pump photon energy is very close to the laser energy so the quantum defect is very small ($<20\%$) and the generated heat is reduced resulting in a high optical efficiency [47-49]. This approach has been demonstrated to achieve 25% optical efficiency for an OPSL device emitting at $2.3 \mu\text{m}$, which is the highest efficiency reported so far for an OPSL emitting beyond $2 \mu\text{m}$ [49]. However, the pump absorption in the thin QW layers is fairly small.

For example, 10-nm of InGaAs only absorbs about 1-2 % of incident pump radiation and a 10-QWs structure absorbs less than 20 % of the pump radiation in a single pass. Consequently, the in-well pumped structure needs careful design optimization of the interaction of the QWs with the pump field. One way to increase the pump absorption is to carefully choose the pump laser wavelength, the pump incident angle and the separation of the QWs so that each QW is at the standing wave anti-node of both the pump and the laser field. This also means that the DBR structure needs to have high reflectivity at both the pump and laser wavelengths. In ref. [49], the in-well pumped OPSL structure has sets of QWs placed in regions of maximum spatial overlap between the pump and the laser standing wave pattern (see Fig. 2.3). Moreover, the different sets of QWs contain varying number of QWs, designed according to the spatial overlap between the pump and the laser standing wave pattern. This complicated structure design together with optimization of the wavelength and the incident angle of the pump achieve

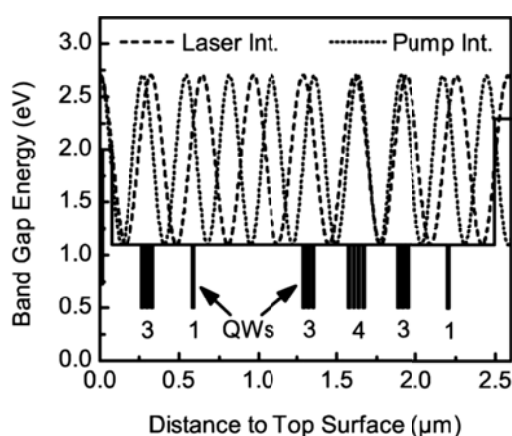


FIGURE 2.3 Band gap energy and optical intensities of the pump and the laser within the active region of the in-well pumped structure.

a resonant pump absorption amounting to over 60%, which is still low compared to the barrier pumped structure which, on the other hand, absorbs the pump in thick barrier layers, resulting in a higher single-pass absorption (>80%). For the barrier pumping structure, the carriers produced in the barrier layers diffuse and are trapped in the QWs which have a smaller band gap energy. Although the quantum efficiency of the barrier pumped structure is smaller than the in-well pumped structure, to date, however, the barrier pumped structure performs much better than the in-well pumped structure in terms of output power for OPSLs emitting at 1 μm . The standard number for the quantum defect is about 20%-30% for 1 μm OPSLs using 808 nm pump sources while the quantum defect is about 50% for 2 μm OPSLs using a 980 nm pump source. The original smaller quantum defect plus a much better pump absorption efficiency make the barrier pumped structure the obvious choice for high power OPSLs emitting at 1 μm .

The OPSL structure we use is a barrier pumped, bottom emitter (Fig. 2.4). The active region consists of 10 InGaAs quantum wells placed between GaAs buffer layers and strain compensating GaAsP barrier layers resulting in 80% pump absorption in a single pass. For obtaining a stable structure, the strain compensating layers are used to reduce structure stress caused by the strained quantum wells which are commonly used to improve operating characteristics.

The QW gain, which depends on the semiconductor composition and the thickness of QWs determines the laser characteristics and performance. To accurately calculate the gain, we use fully microscopic many-body models which have been demonstrated to reproduce and agree well with experimental observations. Unlike

GaAs	73.97nm	DBR	} X20
AlAs	87.87nm	DBR	
GaAs	5nm	Buffer layer	} X9
GaAs _{97.7} P _{2.3}	135.59nm	Strain compensating barrier	
GaAs	5nm	Buffer layer	
In _{19.8} Ga _{80.2} As	8 nm	QW	
GaAs	5nm	Buffer layer	
GaAs _{97.7} P _{2.3}	131.39nm	Strain compensating barrier	
GaAs	5nm	Buffer layer	
In _{19.8} Ga _{80.2} As	8nm	QW	
GaAs	5nm	Buffer layer	
GaAs _{97.7} P _{2.3}	135.59nm	Strain compensating barrier	
GaAs	5nm	Buffer layer	
In ₄₉ Ga ₅₂ P	159.82nm	Caplayer	
GaAs		Substrate	

FIGURE 2.4 OPSSL structure for 1040 nm laser operation

traditional models, the dephasing of the polarization is calculated in this model by solving a Boltzmann-like equation for electron-electron and electron-phonon scattering instead of adopting a constant dephasing time, which is usually obtained from experimental data [50]. This fully microscopic many-body model can truly provide predictive gain properties and laser performance since it does not require fitting parameters; the only inputs are the layer thickness and compositions. This approach is based on the semiconductor Bloch equation which is formed from carrier distribution functions, $f^{e(h)}$ and the equation of motion for the microscopic polarizations [51]. The equation of motion for the microscopic polarizations P_k^{ij} is derived using the many-body Hamiltonian in the Heisenberg picture [52]:

$$\frac{d}{dt} P_k^{ji} = \frac{1}{i\hbar} \left\{ \sum_{i',j'} [\varepsilon_{j,j',k}^h \delta_{i,i'} + \varepsilon_{i,i',k}^e \delta_{j,j'}] P_k^{j'i'} + [1 - f_k^{e,i} - f_k^{h,j}] \mathcal{U}_{i,j,k} \right\} - \Gamma_k^{ji,d} P_k^{ji} + \sum_{i',j',q} \Gamma_{k,q}^{i'j'} P_q^{j'i'} \quad (2.3)$$

where

$$\varepsilon_{i,i',k}^e = \varepsilon_k^{e,i} \delta_{i,i'} - \sum_{i',q} V_{k-q}^{ii''i'i''} f_q^{e,i''} \quad (2.4)$$

$$\varepsilon_{j,j',k}^h = \varepsilon_k^{h,j} \delta_{j,j'} - \sum_{j',q} V_{k-q}^{jj''j'j''} f_q^{h,j''} \quad (2.5)$$

$$\mathcal{U}_{i,j,k} = -\mu_{ij,k} E(t) - \sum_{i',j',q} V_{k-q}^{ij'j'i'} P_q^{j'i'} \quad (2.6)$$

here $i, i'/j, j'$ are subband indexes for electron/holes and k, q are in-plane wavevectors, ε is the single particle energy and μ are the interband dipole matrix elements. In eq. (2.4)-(2.6), V denotes the Coulomb potential, while ε and \mathcal{U} are the renormalized single

particle energies and the renormalized field. The renormalizations due to the Coulomb effect describe the bandgap energy which is carrier density dependent and the renormalized Rabi frequency which leads to Coulomb enhancement of absorption/gain and excitonic resonances [52]. The last two terms in (2.3) denote the microscopic electron-electron and electron-phonon scattering which lead to the dephasing of the macroscopic polarization.

The optical spectra are determined by summing up the microscopic polarization to obtain the macroscopic polarization P :

$$P = V^{-1} \sum_k \mu_k P_k^{ji} , \quad (2.7)$$

where V is the volume of medium. The optical susceptibility $\chi(\omega)$ is then derived by taking the Fourier transform of the macroscopic polarization into frequency space. The real part of the optical susceptibility gives the refractive index and the imaginary part gives the absorption/gain spectrum which can be computed under different carrier density and temperature conditions. Fig. 2.5 is the computed gain of the 1040 nm OPSL structure illustrated in Fig. 2.4. This gain modeling is carried out using SimuLaseTM, which is a semiconductor laser modeling software developed based on fully microscopic modeling that we discussed above [53]. The left plot of Fig. 2.5 shows the modal gain at 300K with carrier density from $0.9 \times 10^{12} \text{ cm}^{-3}$ to $3.1 \times 10^{12} \text{ cm}^{-3}$. With increasing carrier density, the gain amplitude increases, and the gain peak is blue shifted due to band filling and

Coulomb enhancement. The right plot in Fig. 2.5 illustrates the modal gain at different structure temperatures. The gain peak shifts to longer wavelength with increasing temperature and, the gain intensity reduces at higher temperatures. The effects need to be considered in the structure design to achieve OPSL performance with the desired properties.

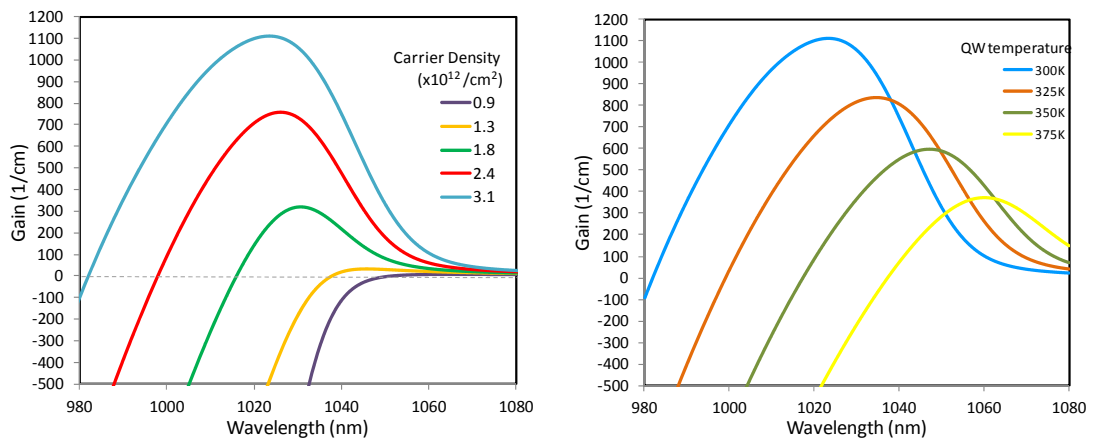


FIGURE 2.5 Left: computed gain with varied carrier densities at 300 K; Right: computed gain at varied structure temperature with carrier density $3.1 \times 10^{12} \text{ cm}^{-1}$

2.1.3 Micro-cavity

The micro-cavity of the OPSL structure is formed between the DBR and the interface between air and the semiconductor structure surface, which is the InGaP cap layer in our structure illustrated in Fig. 2.4. The optical gain spectrum and the reflectivity spectrum strongly depend on the electric field amplitude inside the OPSL micro-cavity, [54, 55] which can be calculated using the transfer matrix method. Fig. 2.6(a) shows

wave propagation through the i th interface and Fig. 2.6(b) shows wave propagation through the i th layer of a multilayer structure. We first build the individual transfer matrix for the two conditions and then calculate the complete transfer matrix by multiplying all individual transfer matrices.

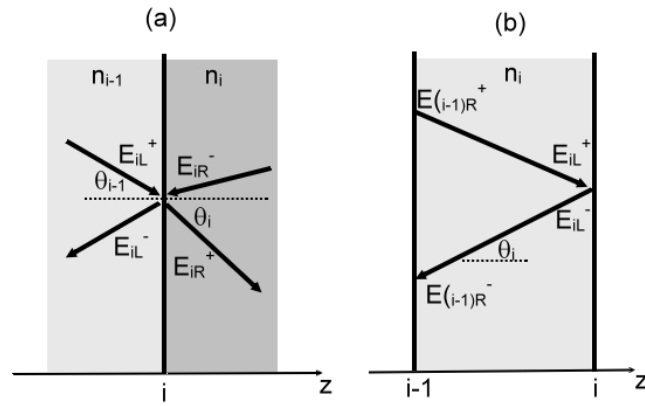


FIGURE 2.6 (a) Transmission and reflection at an interface. (b) Propagation through a layer.

For wave propagation through an interface, the amplitudes of the forward (E_i^+) and backward waves (E_i^-) just at the left (E_{iL}) and at the right (E_{iR}) of the i th interface are related by:

$$E_{iR}^+ = t_{(i-1)i} E_{iL}^+ + r_{i(i-1)} E_{iR}^- \quad (2.8)$$

$$E_{iL}^- = r_{(i-1)i} E_{iL}^+ + t_{i(i-1)} E_{iR}^- \quad (2.9)$$

where $r_{(i-1)i}$ and $t_{(i-1)i}$ are the complex reflection and transmission coefficients given by:

for TE wave:

$$r_{(i-1)i} = \frac{E_{iL}^-}{E_{iL}^+} = \frac{k_{i-1} - k_i}{k_{i-1} + k_i} = \frac{n_{i-1} \cos \theta_{i-1} - n_i \cos \theta_i}{n_{i-1} \cos \theta_{i-1} + n_i \cos \theta_i} \quad (2.10)$$

$$t_{(i-1)i} = \frac{E_{iR}^+}{E_{iL}^+} = 1 + r_{(i-1)i} = \frac{2k_{i-1}}{k_{i-1} + k_i} = \frac{2n_{i-1} \cos \theta_{i-1}}{n_{i-1} \cos \theta_{i-1} + n_i \cos \theta_i} \quad (2.11)$$

and for TM wave:

$$r_{(i-1)i} = \frac{E_{iL}^-}{E_{iL}^+} = \frac{n_{i-1}^2 k_i - n_i^2 k_{i-1}}{n_{i-1}^2 k_i + n_i^2 k_{i-1}} = \frac{n_i \cos \theta_{i-1} - n_{i-1} \cos \theta_i}{n_i \cos \theta_{i-1} + n_{i-1} \cos \theta_i} \quad (2.12)$$

$$t_{(i-1)i} = \frac{E_{iR}^+}{E_{iL}^+} = \frac{n_{i-1}}{n_i} (1 + r_{(i-1)i}) = \frac{2n_{i-1} \cos \theta_{i-1}}{n_i \cos \theta_{i-1} + n_{i-1} \cos \theta_i} \quad (2.13)$$

where k_i is the z component of the wave vector in the i th layer defined as $k_i = n_i \frac{2\pi}{\lambda}$, with n_i the complex refractive index of the i th layer material.

Since the laser wave is usually at perpendicular incidence for the OPSL operation, there is no difference between the TE and TM case. Equation (2.8) and (2.9) can be rearranged to a relation between the forward and the backward propagating wave:

$$\begin{bmatrix} E_{iL}^+ \\ E_{iL}^- \end{bmatrix} = \frac{1}{t_{(i-1)i}} \begin{bmatrix} 1 & r_{(i-1)i} \\ r_{(i-1)i} & 1 \end{bmatrix} \begin{bmatrix} E_{iR}^+ \\ E_{iR}^- \end{bmatrix} = M_{(i-1)i} \begin{bmatrix} E_{iR}^+ \\ E_{iR}^- \end{bmatrix} \quad (2.14)$$

where $M_{(i-1)i}$ denotes the transfer matrix for wave propagation through the i th interface.

Next, we build the transfer matrix for wave propagation through the i th layer (Fig. 2.6b) by the following relations:

$$E_{iL}^+ = E_{(i-1)R}^+ e^{-ik_i d_i \cos \theta_i} \quad (2.15)$$

$$E_{(i-1)R}^- = E_{iL}^- e^{-ik_i d_i \cos \theta_i} \quad (2.16)$$

where d_i is the thickness of layer i . After rewriting equations (2.15) and (2.16), the transfer matrix for wave propagation through the i th layer is obtained:

$$M_i = \begin{bmatrix} e^{ik_i d_i \cos \theta_i} & 0 \\ 0 & e^{-ik_i d_i \cos \theta_i} \end{bmatrix} \quad (2.17)$$

Thus, the complete transfer matrix of the electric field propagation through the multilayer structure can be obtained by multiplication of all individual transfer matrixes:

$$\begin{bmatrix} E_{0L}^+ \\ E_{0L}^- \end{bmatrix} = M \begin{bmatrix} E_{(N-1)R}^+ \\ E_{(N-1)R}^- \end{bmatrix} \quad (2.18)$$

where

$$M = M_{01} M_1 M_{12} M_2 \cdots M_{(N-1)} M_{(N-1)N} \quad (2.19)$$

We now assume a plane wave with amplitude, E_{L0}^+ , incident on the multilayer structure and calculate the reflectivity spectrum of the OPSL structure using the equations described above. First, the individual transfer function can be obtained using the complex refractive index of semiconductor materials calculated using a fully microscopic model. As there is no light coming from the right side of the entire structure, we have $E_{(N-1)R}^- = 0$. Thus, the resulting matrix formulation is:

$$\begin{bmatrix} E_{0L}^+ \\ E_{0L}^- \end{bmatrix} = \begin{bmatrix} M_{11} & M_{12} \\ M_{21} & M_{22} \end{bmatrix} \begin{bmatrix} E_{(N-1)R}^+ \\ 0 \end{bmatrix} \quad (2.20)$$

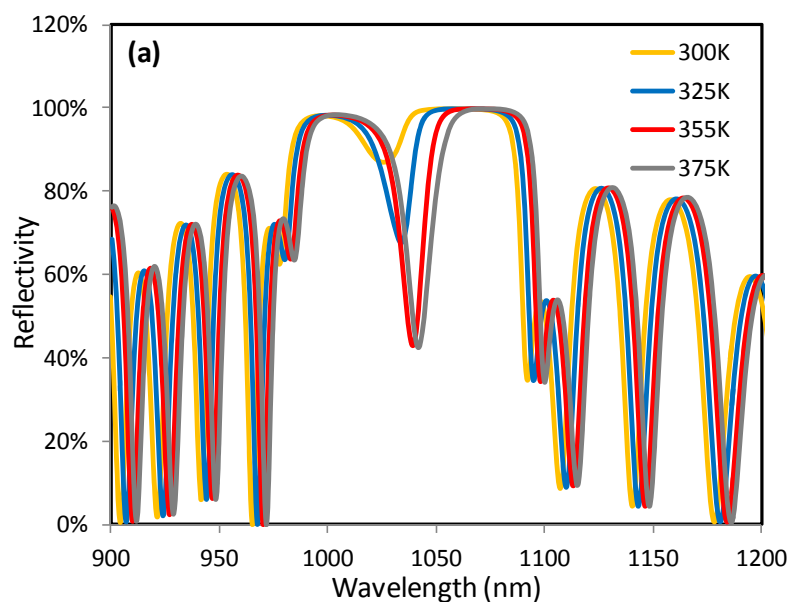
The reflectivity of the structure is given by:

$$R = \left(\frac{E_{0L}^-}{E_{0L}^+} \right)^2 = \left(\frac{M_{21}}{M_{11}} \right)^2 \quad (2.21)$$

Since the imaginary part of the complex refractive index obtained from the fully microscopic model is temperature, carrier density and wavelength dependent, the calculated reflectivity is also temperature, carrier density and wavelength dependent. Fig. 2.7 shows the computed reflectivity spectra of the OPSL structure at different temperature and carrier density conditions. Compared to the computed reflectivity spectrum of the DBR shown in Fig. 2.2, the reflectivity spectrum of the OPSL structure in Fig. 2.7 shows a dip/dome inside the reflectivity stop band. The dip/dome denotes the QW absorption/gain enhanced by the micro-cavity resonance and the depth/height of the dip/dome denotes how well the QW absorption/gain and the micro-cavity resonance are aligned. Fig. 2.8 shows the reflectivity (red), QW absorption (blue), and the longitudinal confinement factor (green), which peaks at the micro-cavity resonance for the OPSL structure at 325 K and carrier density $0.05 \times 10^{12} \text{ cm}^{-3}$. At this temperature, the absorption is at a shorter wavelength than the micro-cavity resonance is. The reflectivity dip is located at the wavelength at which the QWs have the strongest absorption after the micro-cavity resonance enhancement. Therefore, it is not always at the exact wavelength of the absorption peak or the micro-cavity resonance. For example, at 325 K, the dip is at the wavelength between the absorption peak and the micro-cavity resonance. The temperature dependence of the absorption dip is shown in Fig. 2.7(a). With the same carrier density, the reflectivity spectrum and the micro-cavity resonance enhanced QW

absorption shift to longer wavelength with the increasing temperature. Moreover, the depth of the dip also depends on the structure temperature because of temperature dependent spectral overlap between the QW absorption and the micro-cavity resonance. From Fig. 2.7(b), the dip at the center of the stop band becomes a dome indicating a QW “gain” when the carrier density is increased to $2.4 \times 10^{12} \text{ cm}^{-1}$.

The transfer matrix method also can be used to calculate the electric field distribution inside the OPSL micro-cavity. Fig. 2.9 shows the refractive index profile and the standing wave pattern at 1040 nm and 375 K. At this temperature, the standing wave antinodes of the cavity propagating mode coincide with the QWs, leading to resonant periodic gain.



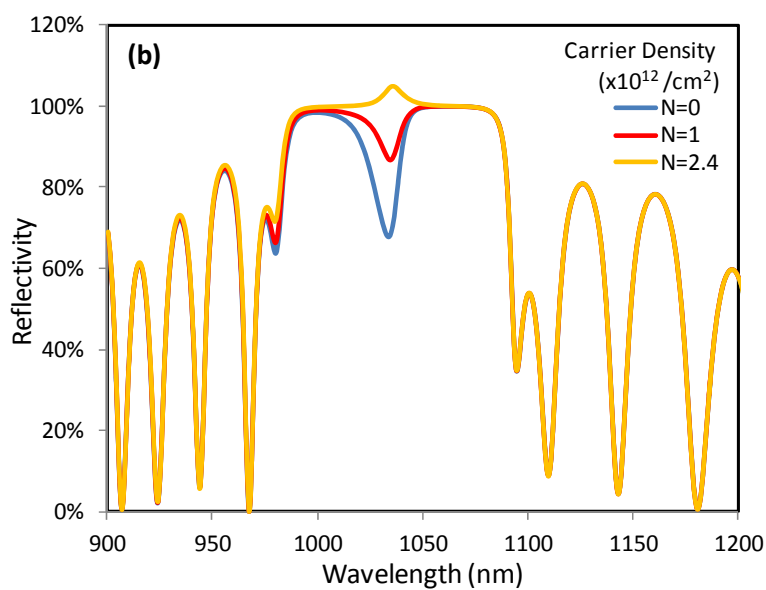


FIGURE 2.7 (a) computed reflectivity spectrum without excitation; (b) computed reflectivity spectrum with varied carrier densities at 325 K.

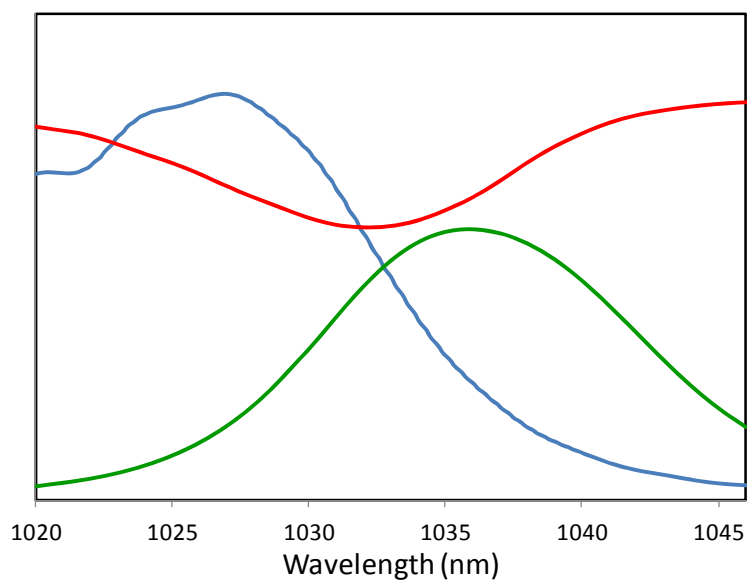


FIGURE 2.8 Blue: calculated QW absorption. Green: the confinement factor. Red: Reflectivity spectrum. The temperature of the structure is at 325 K and the carrier density is $0.05 \times 10^{12} \text{ cm}^{-1}$.

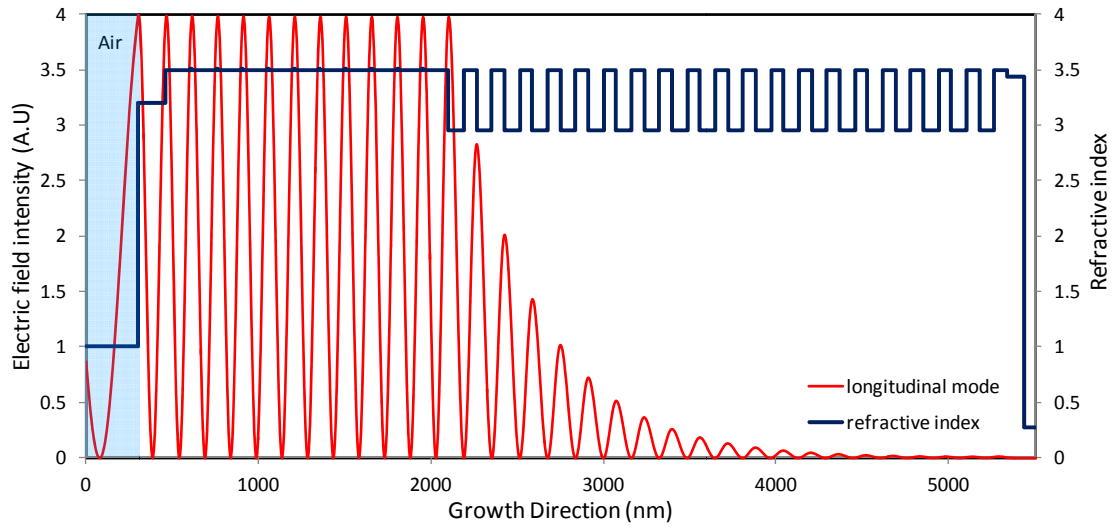


FIGURE 2.9 Longitudinal mode and the refractive index distribution inside the OPSL structure

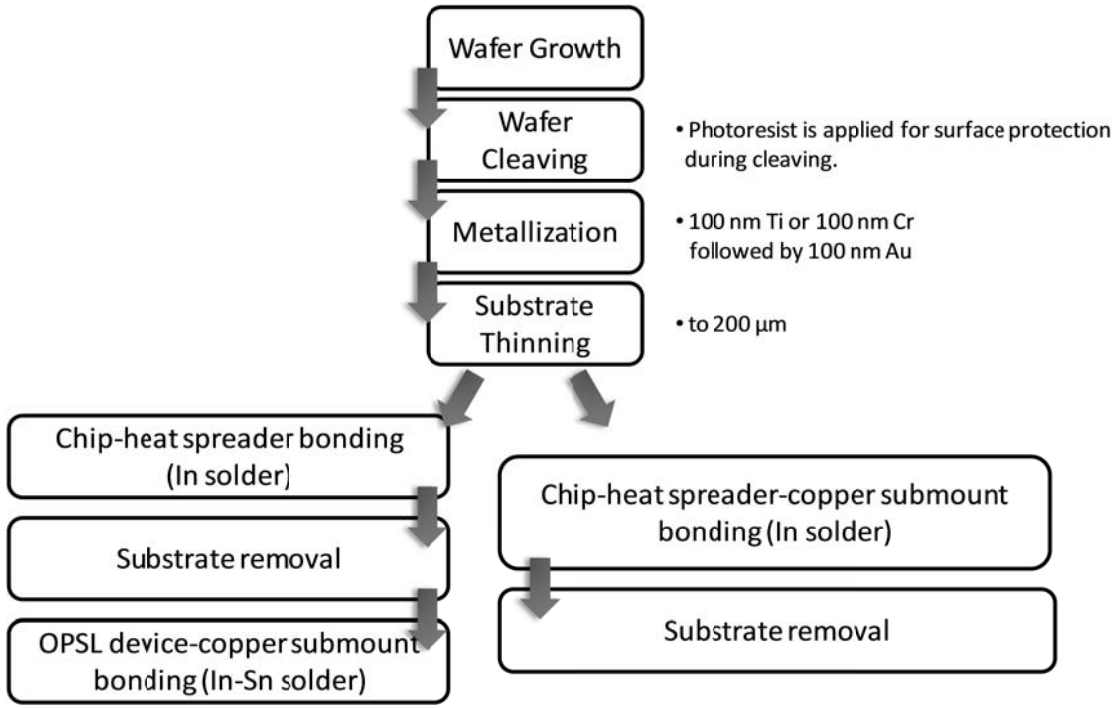


FIGURE 2.10 Flow diagram of the fabrication processes

2.2 Device Fabrication

For our high power OPSL devices, we use the bottom emitter configuration for the OPSL structure. The flow diagram of the fabrication processes is shown in Fig. 2.10. The fabrication includes two major processes: heat spreader attachment and substrate removal. The details of each process are discussed in this section.

2.2.1 Bonding

The first processing step for a bottom emitter structure is soldering the semiconductor chip onto a heat spreader. In this step, the material of the solder layer and the heat spreader need to be carefully chosen by considering their thermal conductivity and thermal expansion coefficient. For our OPSL devices, we use indium solder to bond the semiconductor chip with a diamond heat spreader with a thickness varying from 500 μm to 1 mm. Before the bonding process, both semiconductor chips and diamond heat spreaders are metalized with 100 nm titanium (Ti) or chromium (Cr) followed by 100 nm gold (Au) layer. The Ti layer is used to improve the adhesion of the Au layer which forms an alloy with the indium solder layer during the bonding process. In the early stage of processing development, a 50- μm thick indium film was used as the solder layer and the bonding process was done in the atmosphere without prevention of indium oxidation. An ultrasound image of a processed OPSL is shown in Fig. 2.11(a). The high-intensity area in the ultrasound image denotes solder voids which are air gaps/bubbles inside the solder junction. These air gaps block the heat transfer pathway leading to high local temperature and hence early thermal roll-over or burning of the chip. Consequently, the

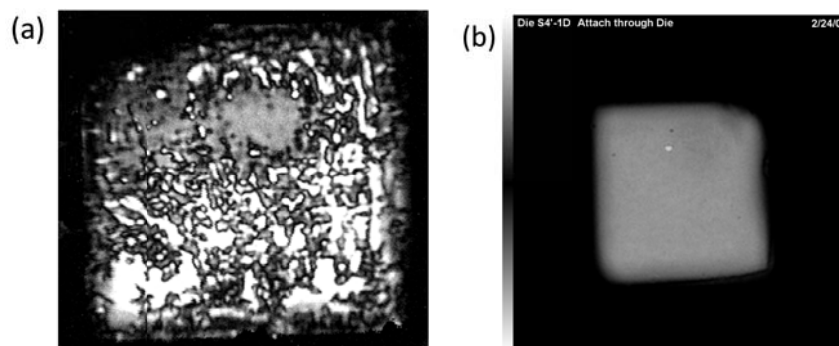


FIGURE 2.11 Ultrasound imaging of bonded chip. (a) voids in solder junction (b) void-free solder junction

highest achievable output power was limited.

To improve thermal management, the 50- μm thick indium film was replaced by a 6- μm thick evaporated indium layer to reduce the heat transfer path. A vacuum chamber is used in the improved bonding process as described below. Before the bonding process, the GaAs substrate of the semiconductor chips is carefully lapped down to a thickness of 200 μm . The thinned semiconductor chip is then soldered onto a diamond heat spreader in a vacuum chamber as illustrated in Fig. 2.12. As shown in this figure, a brass rod applying about 0.9 N of force is placed on a glass force spreader which homogeneously distributes the applied force to the semiconductor chip. The pressure inside the bonding chamber is kept below 21 kPa for the entire bonding process to prevent indium oxidation. Fig. 2.13 shows the temperature ramping recipe used for our bonding process. A much higher temperature (260 $^{\circ}\text{C}$) than the melting temperature of indium at 156 $^{\circ}\text{C}$ is found to work better to obtain a void-free solder junction. In addition, the slow cooling process prevents chip cracking due to different thermal expansion coefficients of the

semiconductor chip, the solder layer and the diamond heat spreader.

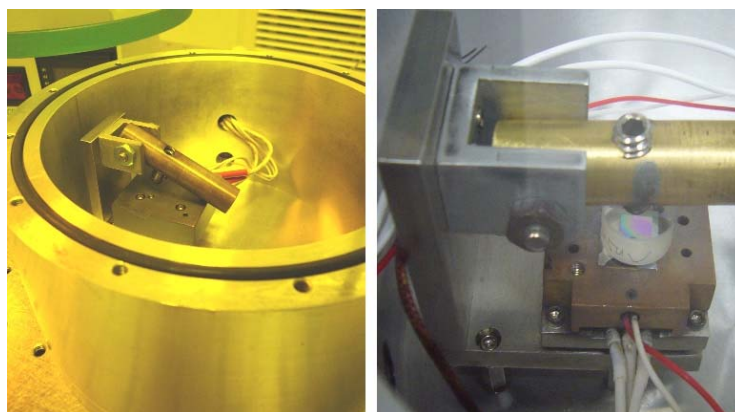


FIGURE 2.12 Vacuum bonding station

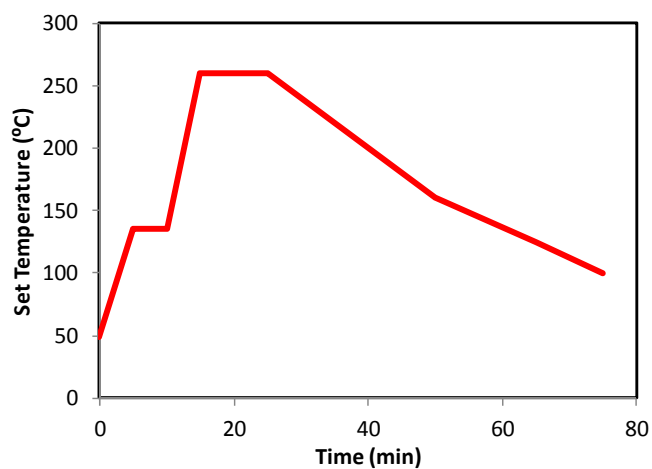


FIGURE 2.13 Temperature setting for semiconductor-heat spreader bonding

To confirm the quality of the solder junction using the bonding procedure described above, the processed OPSL device is investigated by ultrasound imaging (Fig. 2.11(b)). The ultrasound image shows a nearly void-free junction of the processed OPSL device indicating the successful development of bonding procedure for high power OPSL

devices. For better cooling efficiency, some of our OPSL devices are soldered on the Ti-Au metalized copper submount which is a part of the water heat sink using indium or indium-tin solder film (Fig. 2.14). If indium film is used, all the components including the semiconductor chip, the diamond heat spreader, the indium film and the copper submount are properly aligned and bonded all together at once. On the other hand, the semiconductor device can be bonded on copper submount separately using lower soldering temperature (140 °C) if indium-tin film is used for soldering. Although indium has higher thermal conductivity (81 W/m·K) than indium-tin alloy (34 W/m·K), the indium-tin soldering process provides a more flexible way for fitting OPSL devices on different water heat sink geometries because of the separate soldering process.

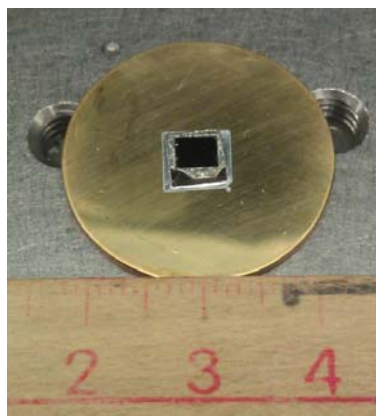


FIGURE 2.14 OPSL device soldered on the copper submount



FIGURE 2.15 Stirring fixture

2.2.2 Chemical wet etching

After thinned semiconductor chips are bonded on diamond heat spreaders, the substrate of the semiconductor chip is removed by chemical wet etching. The choice of etchant for this step depends on the substrate material and the etch-stop layer material. High etching selectivity, i.e. the etching rate ratio of the substrate material to the stop layer material, is required for properly terminating the etching reaction on the etch-stop layer. For our semiconductor chips, the InGaP cap layer in the epitaxial structure also serves as the etch-stop layer, which has an etching rate of 5 nm/min in pH 8.5 hydrogen peroxide and ammonium hydroxide mixture, while the GaAs substrate is etched at 6 $\mu\text{m}/\text{min}$ in this etchant. Since the temperature of the etchant affects the etching rate and the pH value, the temperature during the etching process needs to be well controlled and fixed at 27 °C. Fig. 2.15 shows the stirring fixture we used for the etching process. The two arms of the machine rotate 65 degrees back and forth so the surface of the GaAs

substrate is always perpendicular to the direction of etchant flow resulting in a uniform etching reaction. The final etched semiconductor surface not only affects the scattering loss of OPSLs but also determines the largest working area and pump spot size that can be used. Fig. 2.16(a) is a surface profile picture using a Veeco optical interferometer and the surface roughness profile and parameters are shown in Fig. 2.16(b). The scanning image shows a 1.3 mm diameter aperture with clear and smooth surface for optical pumping. The 1-D surface plot shows the root-mean-square deviation of about 5-6 nm indicating a homogeneous and smooth surface which ensures minimum scattering loss during laser operation. Based on this information, a uniform output performance can be expected across this area.

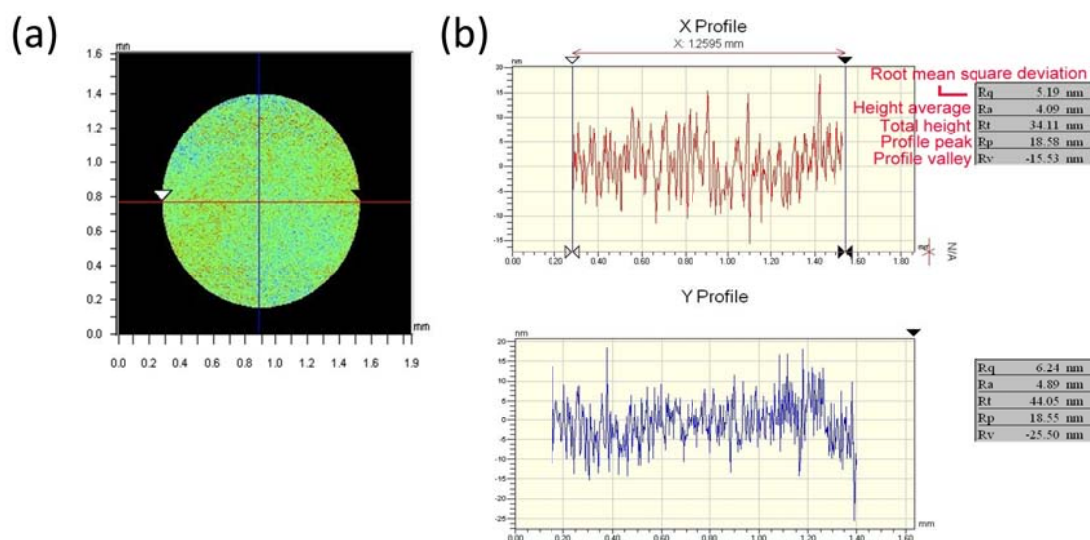


FIGURE 2.16 (a) Surface profile of substrate removed semiconductor chip. (b) 1-D surface height plot.

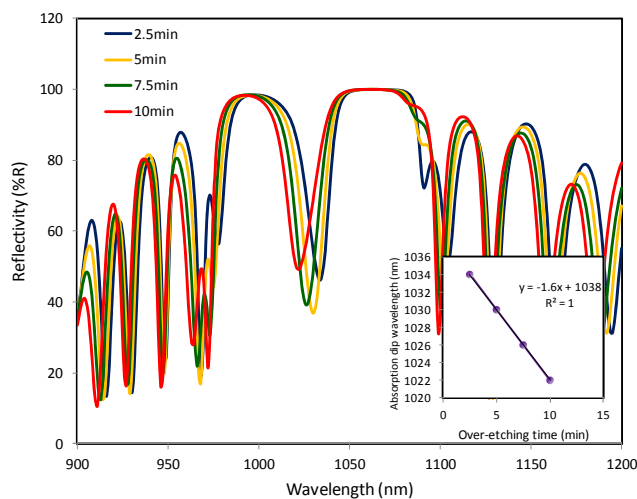


FIGURE 2.17 Reflectivity spectrum measured at 120 °C. The dip wavelength of the OPSL structure vs. etching time after the GaAs substrate is totally removed as an inset is shown.

The etching process also affects the spectral position of the micro-cavity resonance and hence, the laser operation wavelength. The etching process does not completely stop at the etch-stop layer but etches the stop layer slowly. The final thickness of the cap layer, which is also the etch-stop layer in our case, together with other layers in the OPSL structure determine the micro-cavity resonance, which determines the lasing wavelength. Fig. 2.17 shows the 120 °C reflectivity spectra of an OPSL structure with different amount of over-etching. The absorption dip becomes 1.6 nm shorter with every minute of over-etching which means the laser runs at a shorter wavelength if the OPSL device is over-etched. As the result, it is very important to control the etching process to prevent lasing wavelength deviation from the original design. One may carefully control the over-etching to change the laser operation wavelength if a little shorter wavelength is

desired.

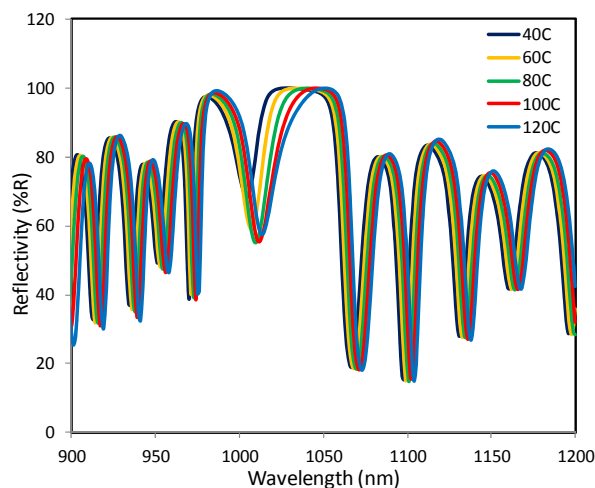


FIGURE 2.18 TDR of 1010 nm OPSL device

2.2.3 Structure characterization

Before we build optical resonators and test the power performance of our OPSL devices, we measure the temperature dependent reflectivity (TDR) spectrum and surface photoluminescence (sPL) for device characterization. Due to the temperature dependent QW absorption and temperature dependent refractive index of semiconductor materials, both the QW gain and the micro-cavity resonance shift to longer wavelength but with different shift rates. By observing the spectral position and the depth of the absorption dip in TDR, information about the dynamic relationship between the QW gain and the micro-cavity resonance can be obtained. Thus, the behavior of the OPSL, such as the related lasing threshold, the optimal operation temperature, and the lasing wavelength can be deduced. For example, Fig. 2.18 shows TDR spectra of an OPSL structure with a QW

absorption designed at a shorter wavelength than the micro-cavity resonance at room temperature. This design is referred to as the negative detuning design.

Since the QW absorption is shorter than the micro-cavity resonance at room temperature, the partial overlap between them leads to a shallower absorption dip in the reflectivity spectrum measured at 40 °C. The depth change from 40 °C to 120 °C reflects the process of QW absorption catching up to the micro-cavity resonance and then running away since the absorption peak shifts faster than the micro-cavity resonance. The temperature where the TDR has the deepest dip is the temperature where the absorption and the micro-cavity resonance align. Without excitation, the actual QW detuning can be calculated by multiplying the difference of this temperature and room temperature with the spectral shift rate difference of the QW absorption and the micro-cavity resonance. Under laser operation where carrier density is much higher than the condition in which TDR is measured, the QW “gain” peak is at a longer wavelength than the QW “absorption” at a given temperature, so the temperature at which TDR has the deepest dip is not exactly the temperature at which the QW “gain” and the micro-cavity align. Although the optimal laser operation temperature is not directly obtained from the TDR, we still can get an approximate idea about relative threshold and roll over behavior among different structures by comparing the temperature where their TDR has the deepest dip. Another thing that can be obtained from TDR is the lasing wavelength, which pretty much follows the micro-cavity resonance. The lasing wavelength of an OPSL that is operated at the optimal working condition can be deduced accordingly. Moreover, the information on deviations, such as layer thickness and semiconductor

composition can be obtained by comparing the measured reflectivity spectrum with a computed one using fully microscopic modeling [56]. Thus, the measured TDR together with the simulated reflectivity spectrum provide a useful tool for OPSL structure diagnostics.

Surface photoluminescence (sPL), which is the PL spectrum measured in the direction perpendicular to the surface of OPSL devices using low optical excitation, is another common tool for OPSL device characterization. Although the experimental setup is easy, and the measurement is done quickly, sPL is a complex multi-peak spectrum containing features that cannot be directly related to optical properties of OPSL devices. The spectral position and the amplitude of peaks in the sPL spectrum are not the same as the PL signal detected from the QW emission in free space. The PL signal emitted from the QWs is modified by a filter function resulting from the dielectric environment of each layer of the OPSL structure. In addition, the temperature dependent PL and refractive index of each layer inside the OPSL structure make sPL temperature sensitive. In order to correctly analyze the sPL, we should compare the experimental sPL data measured at a given temperature with the computed sPL at the same temperature. The computed sPL is calculated as the product of the QW PL and the filter function described in [57]. The QW PL is calculated by solving the semiconductor luminescence equations (SLE) [58, 59]. Fig. 2.19(a) shows a measured sPL spectrum, a computed sPL spectrum, a computed PL and the filter function at 10 °C [56]. It is obvious that the peaks in the sPL are not at the same wavelength as the material PL peak nor the filter function. The linewidth and the shape of sPL spectrum is not only determined by the spectral shape of the QW PL and the

filter function but also is determined by the overlap of the PL spectrum and the filter function. The peak around 1017 nm in the sPL spectrum is from the material PL while the peak around 1030 nm is from the filter function. The short wavelength tail of the PL spectrum and the filter function feature at 982 nm cause an obvious peak in the sPL spectrum. As for the reflectivity spectrum, sPL strongly depends on the device temperature.

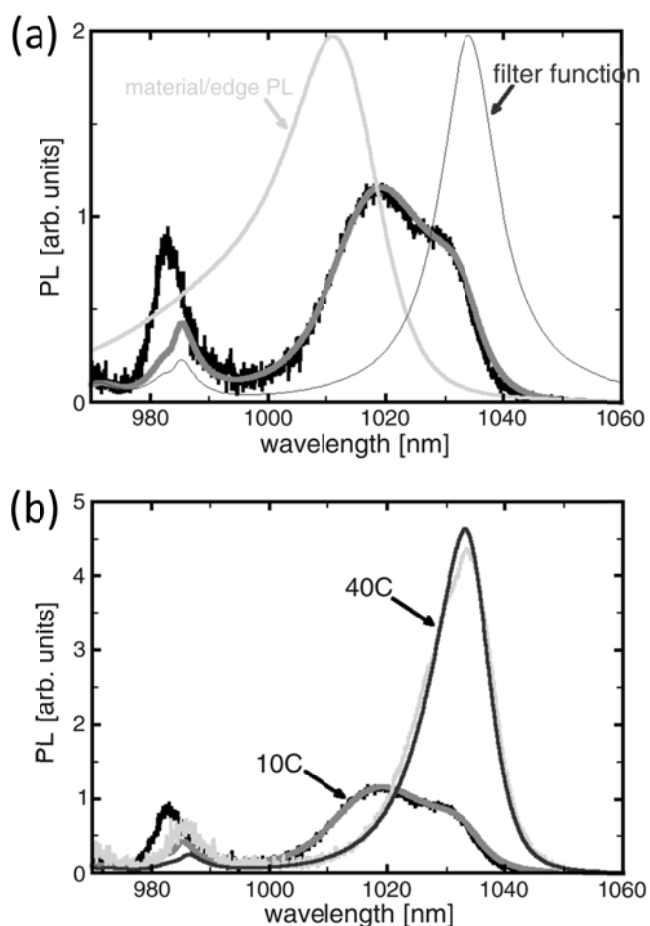


FIGURE 2.19 (a) Measured sPL and calculated sPL for OPSSL at 10 °C and low carrier density. The calculated material PL and the filter function are also shown. (b) Measured sPL and calculated sPL for OPSSL at 10 °C and 40 °C.

Fig. 2.19(b) shows the measured and calculated sPL at 10 °C and 40 °C. The good agreement between theory and experiment is found at both temperatures. The calculated sPL at 40 °C was obtained only by changing the temperature parameter in the simulation which is based on the fully microscopic model. No inputs or assumptions were implemented additionally or differently for predicting sPL at 10 °C and 40 °C. Again, the fully microscopic model needs no specific experimental inputs for fitting measurement conditions. Therefore, the calculated sPL can be obtained for over wide ranges of temperature without additional measurements.

Comparing the experimental data to the computed sPL spectrum or reflectivity spectrum allows us to derive the inhomogeneous broadening, experimental carrier density, and actual structure parameters like layer thickness and material composition. With this information, we can then simulate actual gain spectra at high carrier density for laser performance prediction.

CHAPTER 3 TEMPERATURE EFFECTS, THERMAL ANALYSIS AND OPTIMIZATION OF OPSLs

OPSLs have been proven to be capable of high power operation due to their power scalability. Theoretically, power scaling is achieved by increasing the pump spot size while maintaining a fixed pump power density to keep the heat flux constant. However, the temperature rise increases with the pump spot size and hence limits the power scalability. Therefore, reducing the thermal impedance is an important key to high power generation in OPSLs.

In this chapter, the mechanisms of temperature effects limiting OPSL output power are discussed and the temperature inside the QWs during laser operation is modeled. We analyze the influence of different parameters on the temperature rise in the QWs using commercial COMSOL Multiphysics 4.2 finite element analysis software and develop heat management strategies accordingly.

3.1 Power limiting mechanism

During laser operation, only a portion of the incident pump is converted to the laser output. The quantum defect, which is the photon energy difference between the pump and the laser, together with other lasing inefficiencies, such as non-radiative carrier recombination, are dissipated as heat from the active region. The dissipated heat in the active region induces a peak wavelength shift and reduction of the gain magnitude. In addition, the effective gain is determined by the temperature dependent spectral overlap

between the QW gain and the micro-cavity resonance. The dissipated heat eventually causes spectral mismatch between the QW gain and the micro-cavity resonance leading to reduction of the effective gain. When the effective gain becomes smaller or eventually less than the threshold condition, thermal roll-over occurs and the laser shuts off. Moreover, the local high temperature may also cause permanent damage, especially when a defect is in the pump area.

3.1.1 Temperature dependent effective gain of OPSLs

In a multi-QW structure, the gain is localized in each QW. The total effective gain, G_e is proportional to the material gain G and the intensity of the electric field at each QW location described by the longitudinal confinement factor Γ_z as [60]:

$$G_e \propto G\Gamma_z \quad (3.1)$$

$$\Gamma_z = \frac{\sum_w |E_{i_w}^+ + E_{i_w}^-|^2}{|E_0^+|^2 + |E_0^-|^2} \quad (3.2)$$

where E_{i_w} is the electric field in the w th QW at the i_w th layer inside the OPSL structure. The “+” and “-” sign denote wave propagation in the forward and the backward directions, respectively. Since both the material gain and the longitudinal confinement factor are temperature dependent, the effective gain is also temperature dependent. Let us

start with the temperature effect on the material gain G_0 . In Chapter 2, we showed how the peak intensity and the spectral position of G_0 depend on the QW temperature in Fig. FIGURE 2.5. With increasing temperature, the bandgap of the QWs shrinks and the gain peak shifts to longer wavelength with a rate of approximately 0.3~0.4 nm/K for InGaAs based 1 μm material. The second effect that temperature has on the material gain is temperature dependent gain magnitude which is also shown in Fig. 2.5. It is clear to see that the gain decreases with increasing temperature. This effect will not be further discussed in this section. More detailed and comprehensive discussions can be found in ref. [61].

The second way that temperature rise influences the effective gain is through the longitudinal confinement factor, which has a spectral peak at the wavelength of the micro-cavity resonance. Due to the temperature induced refractive index change of the semiconductor layers, the resonance wavelength shifts to longer wavelength at a rate of 0.1 nm/K. As a result of the different thermally induced shift rates, the material gain and the micro-cavity resonance only align at a certain temperature. Beyond this temperature, the material gain passes the micro-cavity resonance and the effective gain drops. Because the gain of the laser is clamped at the threshold gain, higher carrier density is required to achieve this gain at high temperatures due to the temperature effects mentioned above [62]. Eventually, the laser turns off in a thermal roll-over process which is the major mechanism that limits output power in OPSLs.

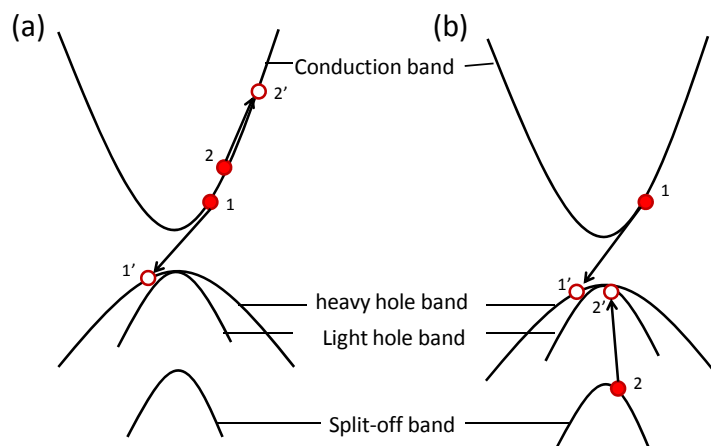


FIGURE 3.1 Mechanisms of Auger recombination processes: (a) CHCC process and (b) CHHH process.

3.1.2 Auger recombination

The pump-laser conversion in OPSLs is a process of pump absorption, carrier production and carrier recombination. The output characteristics of OPSLs, such as lasing threshold, output efficiency and thermal rollover are deeply affected by the carrier recombination process. It is necessary to understand the dependence of carrier losses in OPSLs on the rising temperature during laser operation.

The carrier loss rate is usually modeled using a simple “ABC” power law, where the dependence on temperature can be included in the temperature dependent A, B, C coefficients which are usually determined from experimental data [63]. On the other hand, the microscopic approach provides a fully predictive tool to investigate the carrier losses and a detailed discussion can be found in [64]. Here, we give a short introduction to Auger recombination which is usually the dominant effect in non-radiative carrier recombination.

Fig. 3.1 illustrates two mechanisms of Auger recombination processes: the CHCC process (a) and the CHHH process (b) [65]. In the CHCC process, an electron and a hole (1 and 1' in the figure) recombine and the released energy is transferred to another electron in the form of kinetic energy (2 to 2' in Fig. 3.1(a)) without moving to another energy band, while the released energy is transferred between holes in the CHHH process. Both processes create excited carriers which lose their excess energy in the form of thermal vibrations. In other words, the Auger recombination process is one of the heating mechanisms during OPSL operation. Meanwhile, the Auger recombination rate is affected by heating. The microscopic modeling based Auger recombination calculation for the OPSL structure is shown in Fig. 3.2 [56]. From the figure, Auger recombination (thick dashed line) is found to be more significant at a higher temperature, leading to increased heating. As the result, the increase of device temperature increases carrier recombination induced by the Auger process and vice versa.

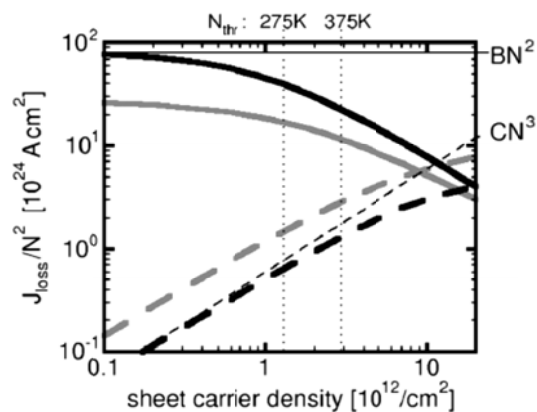


FIGURE 3.2 Carrier loss currents per well at 275 K (black) and 375 K (grey) divided by the density squared. The thick dashed lines represent Auger recombination loss.

3.1.3 Optical and thermal damage

Catastrophic optical damage (COD) is one of the common power limiting mechanisms of semiconductor lasers. COD occurs when the semiconductor material absorbs too much light leading to recrystallization at the laser facet. Since the pump spot size used in OPSLs is usually several hundred microns in diameter, the pump power density at the semiconductor surface is much lower than the damage threshold of COD which is normally between 10 to 20 MW/cm². Nevertheless, permanent damage is still observed in OPSLs. The causes of the permanent damage are usually due to thermal issues. In high power OPSL experiments, two types of permanent damage induced by local heating are observed. The first type of damage is observed when a local solder void exists at the solder junction. This kind of damage usually occurs at a low pump power density and is in the form of a burned hole. Sometimes when the air void is large, the damage process creates a lot of semiconductor particles, contaminating the device surface and leading to high scattering loss. On the other hand, the smaller solder voids can be observed by illuminating with low power pump light before they are burned. Fig. 3.3(a) shows voids under illumination from a 840 μm diameter pump spot. The solder voids appear as high intensity features on the CCD camera. If the pump power increases, the local temperature increases rapidly due to the blocked heat transfer path caused by the solder voids. As a consequence, the area where the void is located leads to burning and leaves a hole precluding laser operation.

The second type of thermal damage usually occurs at the center of the pump spot and is observed around laser rollover. During high power operation, the temperature rise

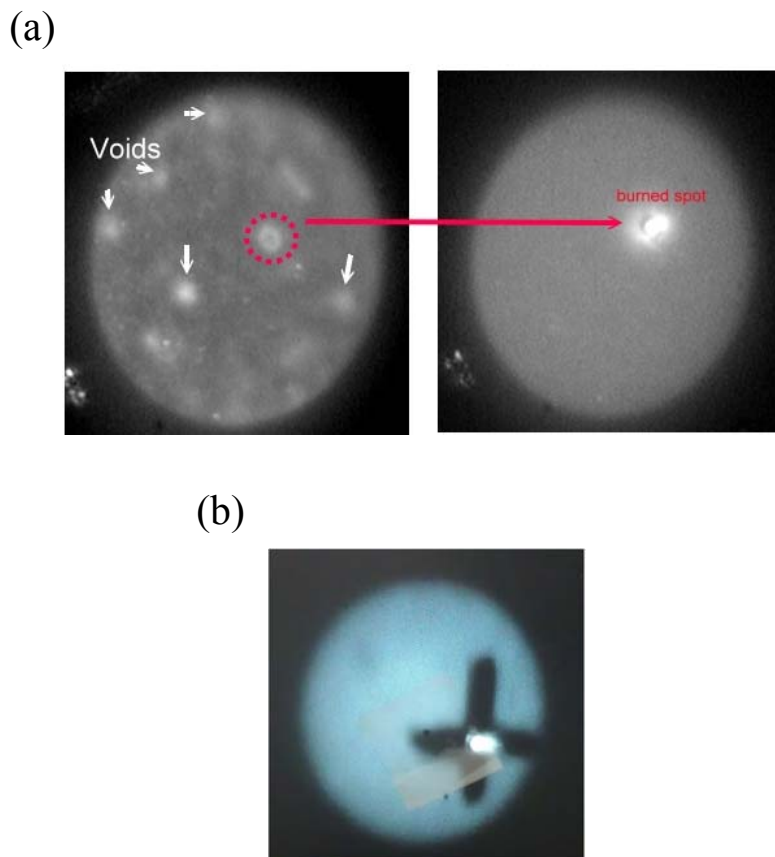


FIGURE 3.3 (a) Solder voids and thermal damage (b) crossed-crack damage

at the pump spot center is usually much higher than that at the edge. The laser may shut off at the center but still be working at the pump spot edge before thermal rollover of the output power. As the pump power keeps increasing, the central temperature is so high that the semiconductor cracks as shown in Fig. 3.3(b). This damage manifests itself as dark lines that differ in appearance from solder void induced thermal damage. Sometimes the semiconductor is cracked only in one direction so the damage looks like a dark line. This kind of damage also happens when a local structure defect is present.

3.2 Introduction of heat transfer in OPSLs

For our OPSL device, which is a thinned semiconductor structure soldered on a diamond heat spreader, the major cooling is accomplished a heat sink that is cooled by a water circulating chiller. The major heat path is from the active region to the heat sink through the DBR, the solder layer, the heat spreader and the copper submount. Two major heat exchange mechanisms are involved in this heat transfer process, conduction and convection.

3.2.1 Heat transfer in solids (conduction)

Heat transfer in solids is through conduction which is a mode of energy transfer due to a temperature gradient. Conduction is described by Fourier's law:

$$Q = -k_{th}A\nabla T \quad (3.3)$$

or

$$q_h = -k_{th}\nabla T \quad (3.4)$$

where Q is heat flow rate (SI units, W), q_h is heat flux (SI units, W/m²), k_{th} is thermal conductivity (SI units, W/m·K), and T is temperature. Fourier's law states that the rate of heat conduction is proportional to the area (A) normal to the direction of heat flow and to the temperature gradient (∇T). One can derive a general conduction equation (3.5) using

equation (3.3) and applying a Taylor series expansion using the principle of conservation of energy which states that the rate of change of internal energy equals the summation of the internally generated heat (Q_i) and the heat flow rate into and out from a volume element [66].

$$\rho C \frac{\partial T}{\partial t} = \nabla \cdot (k_{th} \nabla T) + Q_i \quad (3.5)$$

In equation (3.5), ρ is density (kg/m^3) and C is specific heat capacity ($\text{J/kg}\cdot\text{K}$). For a material where the thermal conductivity is constant, i.e. both independent of temperature and invariant throughout the medium, the steady state conduction equation without internal heat generation can be expressed as Laplace's equation:

$$\nabla^2 T = 0 \quad (3.6)$$

To solve the conduction equation, boundary conditions must be adopted and these can be formulated in several different ways. The first kind of boundary condition commonly used for solving the heat conduction equation consist of defining the temperature on the boundary explicitly. In the water cooled OPSL system, this boundary condition is usually applied at the heat sink water interface where the temperature at this boundary is set at the same value as the water temperature. The second kind of boundary

condition is through specifying an explicit value for the heat flux which is related to the temperature gradient via Fourier's law (3.4). This kind of boundary condition is also used in the middle of active region to supply the heat source for solving the temperature inside the OPSL device. A boundary condition of a third kind specifies an external heat transfer coefficient h , which is related to the temperature gradient (assuming heat flow is in the x direction) through the boundary temperature T_b and the reference fluid temperature T_{ref} by [66]:

$$-k_{th}\left(\frac{\partial T}{\partial x}\right)_{boundary} = h(T_b - T_{ref}) \quad (3.7)$$

The third kind of boundary condition describes heat transfer between a solid medium and external mobile fluids (liquids or gases). This kind of heat transfer is referred to as convection and is discussed in the next section.

Given the boundary conditions, the exact temperature at any point in an analyzed solid system can be obtained by analytically solving the conduction equation. However, solving the partial differential conduction equation analytically is usually complicated even for simple systems. Real systems like water cooled OPSL devices are usually composed of different components with various thermal properties and shapes and the actual boundary conditions tend to be complicated making solution of the conduction equation even more difficult. Numerical techniques, on the other hand, give approximate solutions to partial differential equations at "mesh points" providing a good tool for

efficiently solving partial differential equations over complicated domains. In the thermal analysis discussed in 3.2.3, we use simulation software based on finite element analysis, one of the numerical techniques used to determine the temperature inside the OPSL device. The details of the system geometry and the boundary conditions are also described in 3.2.3.

3.2.2 Convection

Convection is the form of heat transfer that takes place in moving fluids (liquids or gases). If the motion of fluids is generated by external means such as a pump or a fan, it is referred to as forced convection. If the fluid motion is created by density variations induced by temperature differences, it is referred to as natural convection. In convective heat transfer, the heat flow rate Q from a solid surface to an adjacent moving fluid is expressed as:

$$Q = hA(T_b - T_{ref}) \quad (3.8)$$

or

$$q = h(T_b - T_{ref}) \quad (3.9)$$

The equations (3.8) and (3.9) look very simple, but complexities are hidden in the convective heat transfer coefficient h (SI units, W/m^2K). The convective heat transfer

coefficient is not a thermal property like thermal conductivity but depends on the velocity of the fluids, the presence of turbulence or laminar flow, surface geometry and fluid properties like density, viscosity, and thermal conductivity. As a result, not only the configuration of the OPSL device itself but also the specification of the external chiller, heat sink geometry, and coolant types affect the thermal impedance of OPSLs during laser operation.

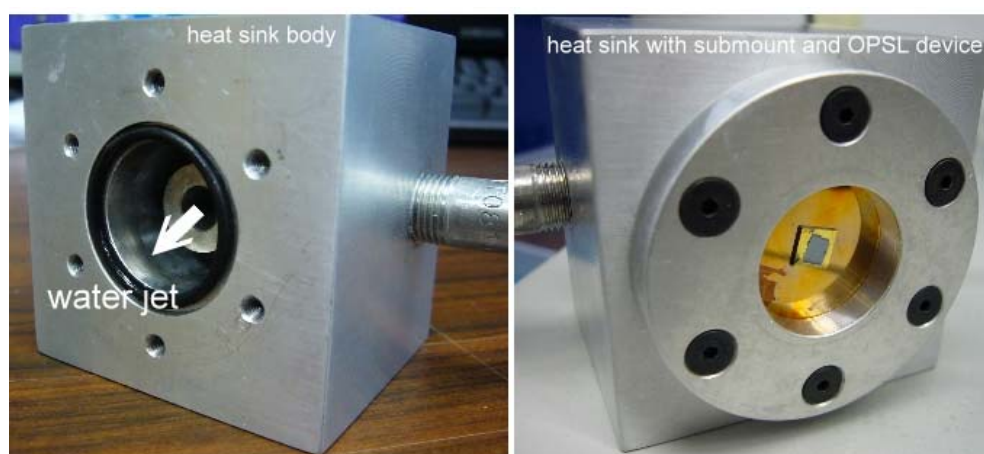


FIGURE 3.4 Water heat sink. Left: heat sink body without the copper submount. Right: heat sink with the copper submount and an OPSL device

It is important to assume convective heat transfer for the boundary condition at the heat sink surface contacting with the coolant instead of using a fixed temperature when analyzing temperature rise in OPSLs to identify opportunities for thermal management improvement. Fig. 3.4 shows the water heat sink that we used for cooling our OPSL devices. This cooling system is based on forced convective cooling using an

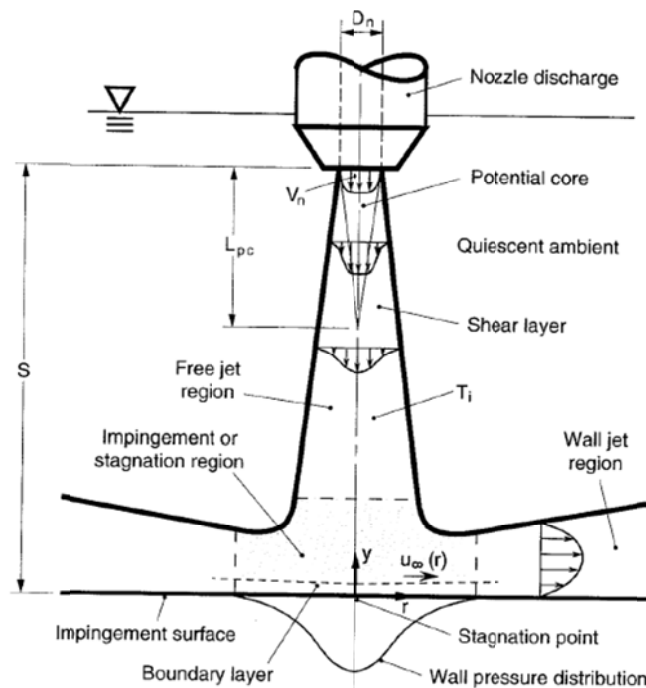


FIGURE 3.5 Flow regimes associated with impingement of a circular submerged jet.

impinging liquid jet. In general, an impinging liquid jet may be classified according to whether it is a circular or planar jet based on the jet cross section, and whether it is a free surface jet or a submerged jet. A free-surface jet is discharged into an ambient gas, whereas a submerged jet is discharged into liquid of the same type. The impinging jet in our heat sink is a submerged, circular jet which is illustrated in Fig. 3.5 [67]. As shown in the figure, the impinging jet is subdivided into three regions, a free jet, an impingement jet (stagnation zone) and a wall jet. The heat transfer coefficient is found to be formulated differently according to the region where heat transfer takes place. In addition, the heat transfer coefficient depends on the turbulence intensity of the impingent jet and the radial velocity in an impingement through the Nusselt number N_u :

$$h = N_u \frac{k_f}{L_t}, \quad (3.10)$$

where k_f is thermal conductivity of the coolant fluid and L_t is the length of the cooling target. In general, the Nusselt number depends on the Reynolds number R_e , the ratio of nozzle-to-target distance to the nozzle diameter (S/D_n), and the ratio of radial distance to the nozzle diameter (r/D_n). A larger Reynolds number gives a larger heat transfer coefficient. The Reynolds number R_e is of the form:

$$R_e = \frac{V_f L_t}{\nu_f}, \quad (3.11)$$

where V_f is the fluid velocity inside the nozzle and ν_f is the kinematic viscosity of fluid. From (3.11), one can see that the Reynolds number depends on the fluid velocity inside the nozzle which is determined by the chiller pump and the diameter of the nozzle (D_n). The other parameters, S/D_n and r/D_n also depend on D_n [67]. The details of the effects upon the impingent jet from the two parameters, S/D_n and r/D_n , are not discussed here but a rule of thumb is to use S/D_n close to 6 and to use as small on r/D_n as possible [67-70]. In the next section, we calculate the heat transfer coefficient for an improved heat sink design based on the discussion above.

3.3 Thermal simulations

As described earlier, thermal issues are detrimental to the OPSL performance in several ways and thus optimization of thermal management is essential for high power OPSLs. In this section, we model the temperature rise at the center of the QWs in different device cooling formats to optimize and improve thermal management by using commercial COMSOL Multiphysics 4.2 finite element software. Parameters such as the pump intensity profile, materials and geometries of the heat spreader, solder layers and the heat sink submount are considered in detail here.

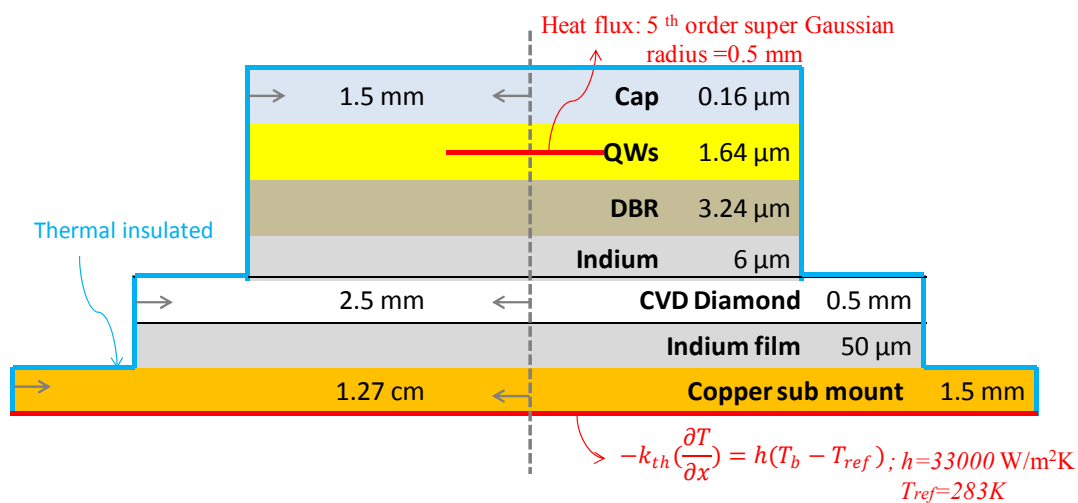


FIGURE 3.6 Geometry and standard parameters used for thermal simulations

3.3.1 System geometry and boundary conditions

Improvement and optimization of thermal management focuses on three areas, convective cooling of the water heat sink, the heat source, and conduction in the OPSL device. Fig. 3.6 shows the system geometry and parameters to be optimized. In the modeling, an axially symmetric device is assumed and all thermal conductivities are kept constant. Since convective cooling at the water-heat sink interface is one of the boundary conditions, we start with strategies for improving convective cooling and the formulation of this boundary condition.

In 3.2.2 we introduced the impinging jet based water heat sink we use for cooling our OPSLs and the dependency of the heat transfer coefficient on nozzle geometry. Several parameters affecting the Nusselt number are not easily altered for improvement, such as coolant properties and the chiller pump characteristics. Here, the improvement is only based on one parameter, the nozzle diameter (D_n), which affects the fluid velocity inside the nozzle and the ratios S/D_n and r/D_n . A previous water heat sink design has a 6 mm diameter nozzle giving S/D_n of 1.9 ($S=11.5$ mm) and maximum of r/D_n 0.42 if a 5×5 mm diamond heat spreader is used. The improved design has $D_n = 4$ mm and the new S/D_n and r/D_n are 2.9 and 0.6, respectively. The Nusselt number for the old and the improved design can be calculated using (3.11) by [71]:

$$\begin{aligned} N_u &= 1.29 R_r^{0.5} P_r^{\frac{1}{3}} = 402 \text{ (for } D_n = 4 \text{ mm)} \\ &= 329 \text{ (for } D_n = 6 \text{ mm)} \end{aligned} \quad (3.12)$$

where P_r is the Prandtl number. The values of the parameters used for this calculation are

listed in Table 3.1. The heat transfer coefficients calculated using (3.10), and (3.12) for the two designs are around 33000 W/m²K for $D_n = 4$ mm and 27000 W/m²K for $D_n = 6$ mm. More than a 20% increase in the heat transfer coefficient is obtained by simply reducing the nozzle diameter. This improvement reflects a 3~4 °C reduction of the OPSL temperature in the center of the active region when the standard system geometry (Fig. 3.6) is used for the simulation. Further reducing the nozzle diameter can further increase the fluid velocity and thus the Reynolds number, but it also increases r/D_n which causes a dramatic decrease in the Nusselt number. The other boundary conditions used in the simulation include a boundary heat source with a 5th order super Gaussian profile ($\propto \exp(-r/w)^5$) located in the middle of the quantum wells, and thermally insulated boundaries imposed on all other surfaces except for the axis of symmetry and the bottom surface of the copper submount.

TABLE 3.1
Parameters for heat transfer coefficient calculation

V_f	the fluid velocity inside nozzle	= 10 m/s for $D_n = 4$ mm = 4.4 m/s for $D_n = 6$ mm
ν_f	the kinematic viscosity of fluid (50% Ethylene glycol)	4.81×10^{-6} m ² /s [ref]
L_t	width of OPSL device	5 mm
P_r	Prandtl number	40
k_f	thermal conductivity of 50% ethylene glycol	0.42 W/m-K

3.3.2 Heat source

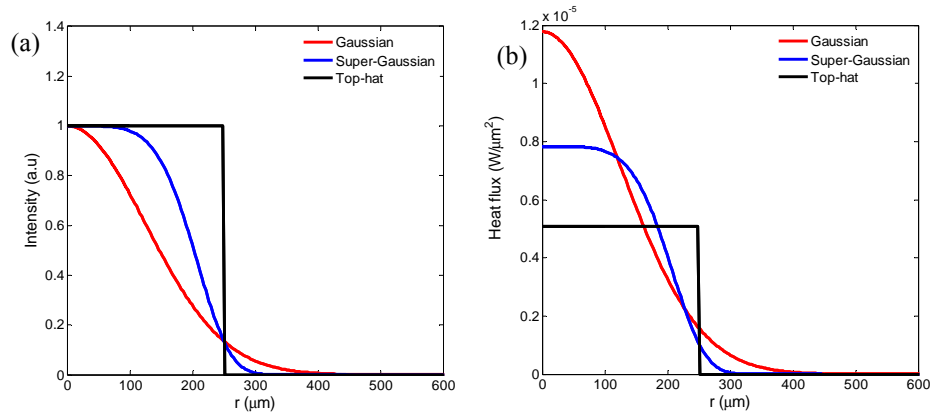


FIGURE 3.7 Transverse profiles of heat sources. (a) Normalized Gaussian, super-Gaussian and uniform pump profile with a radius of 250 μm (b) Heat flux profiles of Gaussian, super-Gaussian and uniform pump source with a power of 100 W

The transverse intensity profile of the boundary heat source in a system has a large influence on the temperature distribution and the maximum local temperature at thermal equilibrium. Therefore, the maximum temperature of the pump area can vary considerably when it is pumped by lasers with different transverse intensity profiles. Fig. 3.7(a) shows a Gaussian, a 5th order super-Gaussian and a top-hat (or uniform) pump profile. All three pumps have a radius of 250 μm where the intensities of the Gaussian and the super-Gaussian drop to $1/e^2$ of the peak value. The heat flux profiles of the three heat sources with 100 W of dissipated power are shown in Fig. 3.7(b). One can see that a Gaussian pump has a much higher local heat flux at the center of the pump beam. This high heat flux can therefore induce high local temperatures leading to thermal rollover in OPSL operation. Fig. 3.8 shows the radial temperature distribution across the center of the active region. As shown in the figure, the central temperature in the active region of

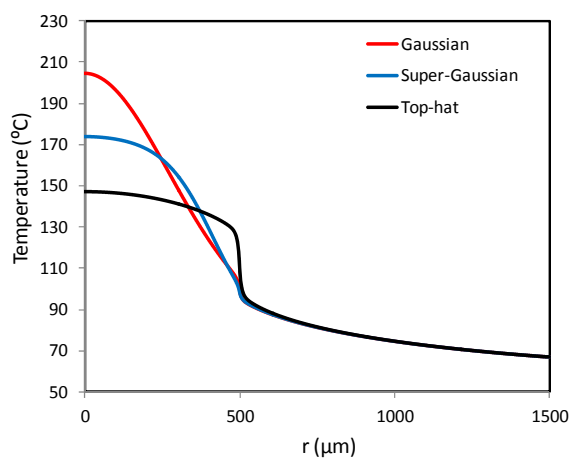


FIGURE 3.8 Radial temperature distribution of OPSL devices pumped by uniform beam, super-Gaussian beam and Gaussian beam

the device pumped by a Gaussian profile beam has much higher value compared to the temperature rise caused by the other two pump profiles. Since thermal rollover depends on a local temperature value, the device would have thermal rollover at a lower pump power if it is pumped by a Gaussian distributed beam. In addition, the temperature difference between the center and the edge of the pump area is larger for devices pumped by a Gaussian profile beam. As the central temperature reaches the rollover temperature, the output power from the pump spot center decreases and eventually shuts off. However, the temperature at the pump spot edge is still low so the laser is operating normally in multi-mode operation. The total output power contributed from the center and the edge of the pump spot may not show reduction at some points even if the center area has shut off. Thus, continued pumping in this area may cause permanent thermal damage at the center before a total output power roll-over is observed (Fig. 3.3b). On the other hand, the center temperature and the temperature difference are much lower in the device pumped by a

top-hat like beam. Therefore, the top-hat like beam is most suitable for high power OPSL operation.

3.3.3 Thermal optimization of high power OPSL devices

To obtain high power output from a single OPSL device, the common method is to scale the pump area with a constant pump power density so that the output power is scaled with the pump area. In the previous thermal analysis, we compared the 3D heat flux from the active region of the OPSL chip when pumped by a 500 μm and a 1 mm spot ($1/e^2$ diameter) [72]. The larger pump spot displays a quasi-1D heat extraction near center signifying a path to power scaling via pump spot increase. However, the absolute temperature inside the active region was higher from the larger pump spot due to the reduction of heat spreading at the center of the pump. The temperature rise increases with the pump spot size and hence limits the power scalability of OPSLs. Fig. 3.9 shows the central temperature in the active region of an OPSL device pumped by a 5th order super-Gaussian beam with a diameter from 500 μm to 1200 μm . The pump power density is fixed at 191 W/mm^2 for all pump sizes. Although the heat flux is fixed, the center temperature is not a constant. As we discussed earlier, thermal rollover occurs when the local temperature exceeds the rollover temperature. When a larger pump spot is used, the rollover temperature is reached at a lower pump power. Thus, the power scaling of OPSLs is limited.

For improving the power scalability of OPSLs, we optimized the device geometry and tried to minimize the slope of the pump size dependent temperature curve (Fig. 3.9).

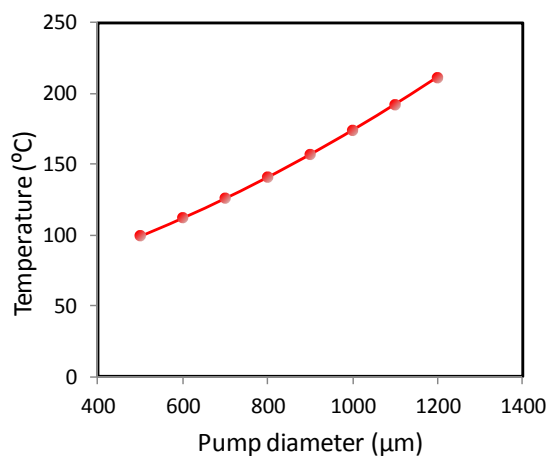


FIGURE 3.9 Simulated pump spot size dependent center temperature. The pump power density is fixed at 191 W/mm^2 for all pump sizes.

Each parameter is analyzed independently meaning that only one variable is used in one simulation and other structure parameters are unchanged using the values shown in Fig. 3.6. The first factor discussed here is the thickness and the width of the heat spreader. Many papers have discussed the importance of material selection for the heat spreader and CVD diamond is considered the best material for heat spreading and heat sinking due to its high thermal conductivity. Here, CVD diamond with a thermal conductivity of $1800 \text{ W/m}\cdot\text{K}$ is used as the heat spreader. The influence of the diamond width and thickness on the temperature are plotted in Fig. 3.10(a) and (b). With the increase of the diamond thickness/width, the degree of heat spreading increases and hence a lower temperature rise is calculated. In addition, the slope of the pump size dependent temperature curve is reduced when the diamond dimension increases. This influence becomes less significant when the diamond width is larger than 7 mm and the thickness is larger than $500 \mu\text{m}$. Therefore, the best diamond dimension for power scaling is about $7 \times 7 \times 0.5 \text{ mm}$

considering the device cost and the cooling efficiency.

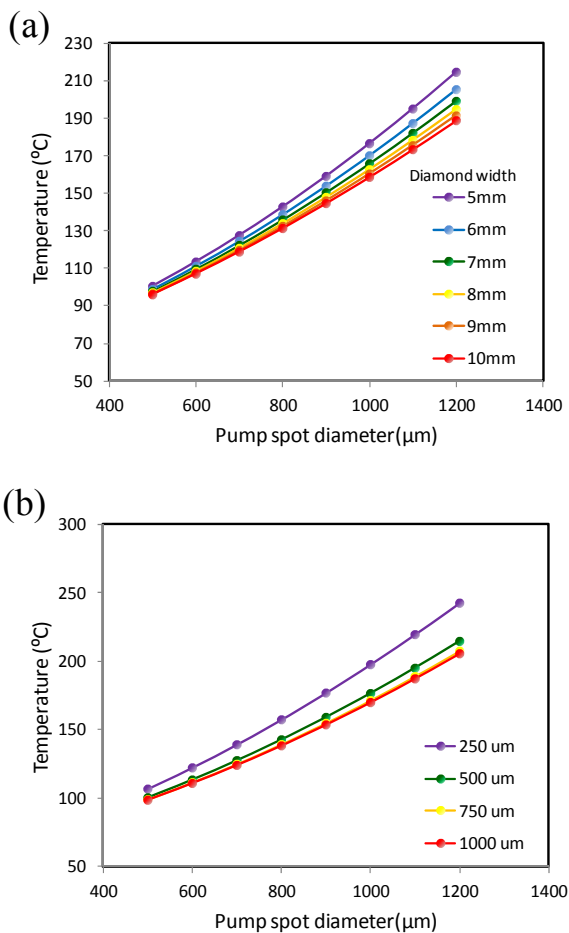


FIGURE 3.10 Simulated pump spot size dependent center temperature. (a) Center temperature in OPSL devices with various diamond widths (b) Center temperature in OPSL devices with various diamond thicknesses.

The second parameter we analyze is the thickness of the indium solder between the semiconductor chip and the diamond heat spreader. Fig. 3.11 illustrates the center temperature for different pump spot sizes when different thicknesses of the indium solder are used. Although the slopes of the pump size-temperature curves in the figure are

almost the same, the absolute temperature in the active region increases significantly with increasing solder thickness. Every 2 μm decrease in solder thickness reduces the temperature by approximately 7 $^{\circ}\text{C}$. However, bonding weakness, which could cause thermal damage or early thermal rollover, is observed if the thickness of the indium solder is reduced too much. To achieve both a good bonding junction and effective cooling, we use a thickness of 6 μm for high power OPSL operation.

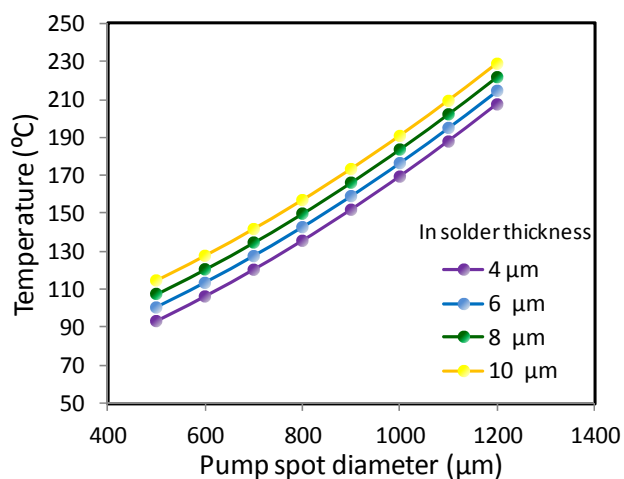


FIGURE 3.11 Simulated pump size dependent temperature in devices with different indium solder thickness

There is another indium layer in our OPSL device/cooling system. This indium layer bonds the OPSL device and a copper submount together. In the early version of the OPSL device/heat sink setup, the two components were not soldered together but only contacted to one another. Mounting irregularities sometimes cause an air gap between the copper submount and the OPSL device and hence affect OPSL output performance.

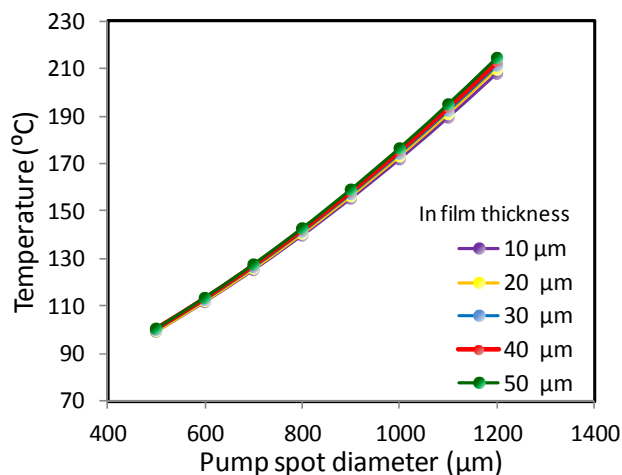


FIGURE 3.12 Simulated pump size dependent temperature in OPSL devices soldered on the copper submount for different thicknesses of the indium solder

We now solder OPSL devices onto the copper submount to make OPSL performance more reproducible and unaffected by the mounting condition. The influence of the submount solder thickness on power scaling is also analyzed for further optimization. Fig. 3.12 shows the temperature at the center of active region in OPSL devices soldered on the copper submount with different thicknesses of the indium solder. Unlike the indium layer between the diamond and the OPSL chip, the indium layer between the OPSL device and the copper submount has less influence on the temperature rise in the active region. The dependence of the temperature on solder thickness is insignificant, with the temperature about 1 °C lower for every 10 μm reduction in indium thickness. Moreover, the indium layer used between the copper submount and the OPSL device is in the form of a metal film which is soft and difficult to handle when it is too thin. Therefore for easier processing, most of our OPSL devices are bonded on the copper submount by a 50 μm thick indium solder film.

The final structure that we analyze is the copper heat sink submount. As shown in Fig. FIGURE 2.14, this structure is a 1 inch diameter copper disc for fitting into the heat sink body. For thermal optimization, we calculate the temperature in the active region by changing the thickness of the copper submount; the results are shown in Fig. 3.13. From the figure, we observe a slight temperature drop for the device bonded on a thicker copper submount, especially from 1.5 mm to 2 mm (about 5 K for a spot size larger than 1000 μm). This result indicates that this copper submount not only exchanges heat from the OPSL device to the external pumped coolant, but also spreads the heat from the OPSL device. Therefore, the thicker copper submount can lead to a lower temperature in the active region.

Except for the copper thickness, we made some geometry changes to the copper submount for increasing the area that the diamond heat spreader contacts the copper submount. The new version of the copper submount is shown in Fig. 3.14. A rectangular recess is drilled at the center of copper disc for an OPSL device to fit in and indium-tin solder is used for filling the gap between the diamond and the copper. We anticipate that this new copper submount can provide additional cooling at the sides so that temperature in the active region will be further reduced. In order to investigate this, we calculated the pump spot size dependent temperature and compare this result to the simulated result we discussed earlier in Fig. 3.13. It is found that the temperature in the active region is much lower when the new version of the copper submount is used. Increasing the area of diamond contacting the cold copper block helps to spread the produced heat so the maximum temperature is reduced in the system.

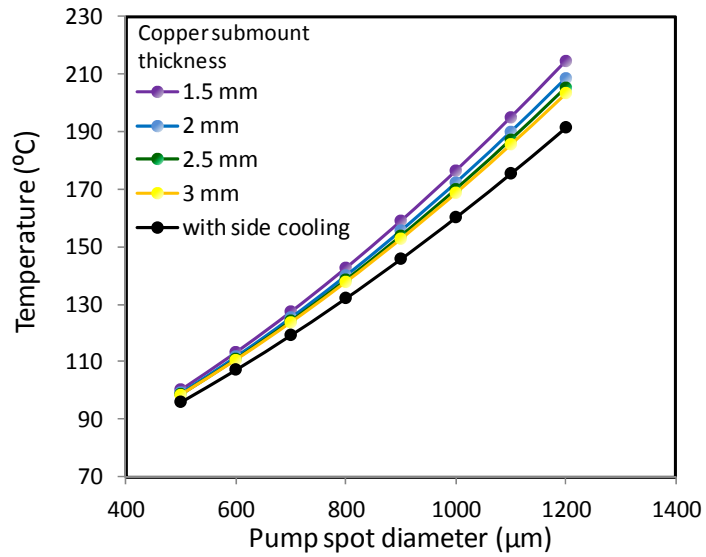


FIGURE 3.13 Simulated pump size dependent temperature in OPSL devices soldered on copper submount with various thicknesses and temperature in the OPSL device soldered on a copper submount with side cooling design.

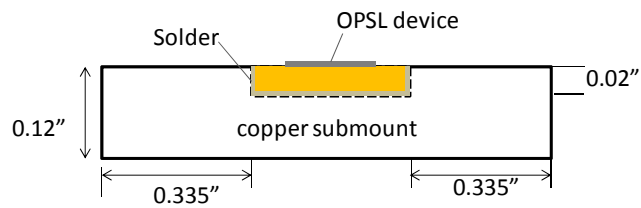


FIGURE 3.14 Copper submount with a recess for side cooling.

CHAPTER 4 HIGH POWER MULTI-TRANSVERSE MODE OPSLS

High-power semiconductor lasers are of particular interest in applications such as pump sources for diode-pumped solid-state lasers (DPSSLs) and high-energy Q-switched Nd:YAG lasers since the emission wavelength of the semiconductor lasers can be designed to fit the pump wavelength that the solid state lasers require. For traditional single element semiconductor lasers, edge emitters are usually preferred for high power applications because they deliver tens of watts of output power at high conversion efficiencies. However, the output beam of edge emitters is highly elliptical and highly divergent, while the output beam of OPSLS is circular and symmetric. Moreover, uniform optical pumping over few hundred microns is achievable so output power of several tens of watts can be realized from a single OPSL device [23, 73]. In the last two chapters, the theoretical and practical basics for the development of high power OPSLS have been discussed. Here we demonstrate over 100 W of CW power from a single OPSL device as a stepping stone to developing a kW-level OPSL system.

4.1 Experimental setup

The OPSL experimental setup is illustrated in Fig. 4.1. The processed device was mounted on a water heat sink with the coolant kept at 10 °C or lower. One or two 808-nm pump beams from multi-mode, fiber-coupled diode stacks are expanded and imaged onto the OPSL device at a small angle of incidence. A simple linear cavity was used for high power multi-transverse mode OPSL experiments. The concave output coupler has a 10

cm radius of curvature. With the configuration shown in Fig. 4.1, the optimal transmission of the output coupler was found to be between 4.5% to 5% for the uncoated OPSL devices used in this research.

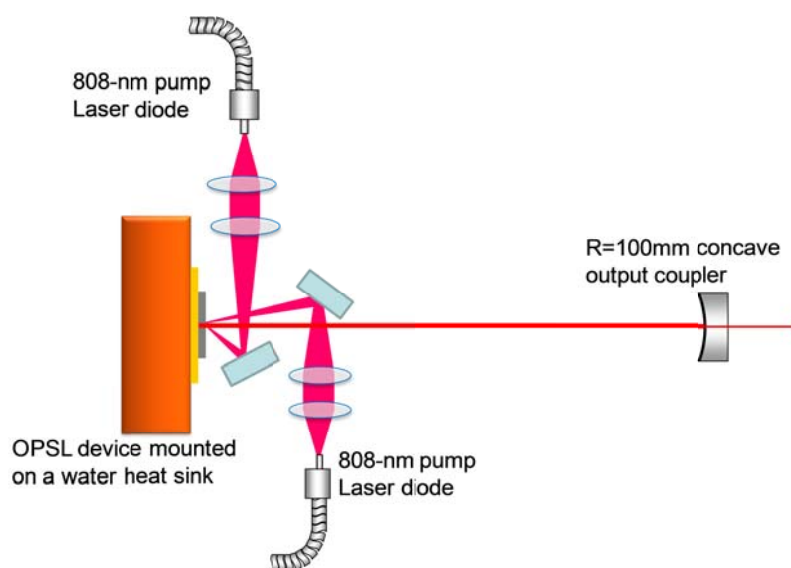


FIGURE 4.1 Schematic setup of OPSLs

4.1.1 Pump laser profile

To obtain sufficient pump power for pumping a large area of an OPSL device, two different lasers are used to pump the OPSL device simultaneously. The first pump laser is a 200 W fiber-coupled (200 μm core) diode laser from Apollo Instruments Inc. and the intensity profile is illustrated in Fig. 4.2. The intensity profile looks like a high order super Gaussian on top of a top-hat beam. The center intensity is a bit higher than the side but the intensity distribution has sharp edges which can reduce the temperature

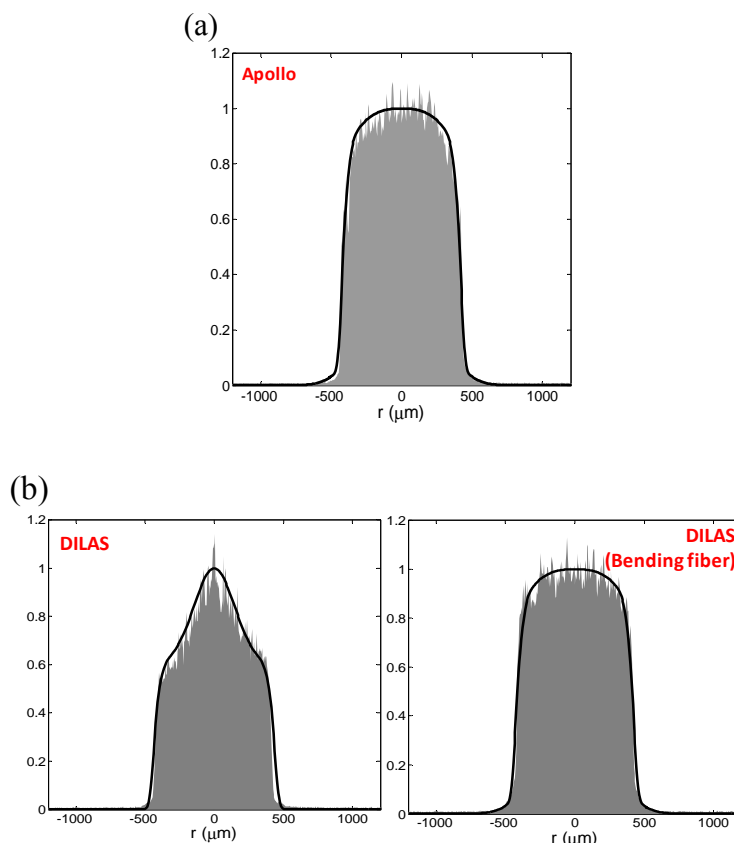


FIGURE 4.2 (a) Intensity profile of Apollo laser. (b) Left: intensity profile of DILAS laser. Right: Intensity profile of DILAS laser with fiber bending

difference across the pump area. The second pump laser is a 200 W fiber-coupled (400 μm core) diode laser from DILAS which has an intensity distribution close to a Gaussian beam on top of a top-hat profile. The center intensity is much higher than the edge so it is likely to cause thermal rollover at a pump power lower than that which causes thermal rollover by the Apollo laser. To investigate this, we pumped an OPSL device using the two pump lasers in different combinations and the OPSL power curves are shown in Fig. 4.3(a). Curve A denotes output performance of an OPSL device pumped by a 132 W

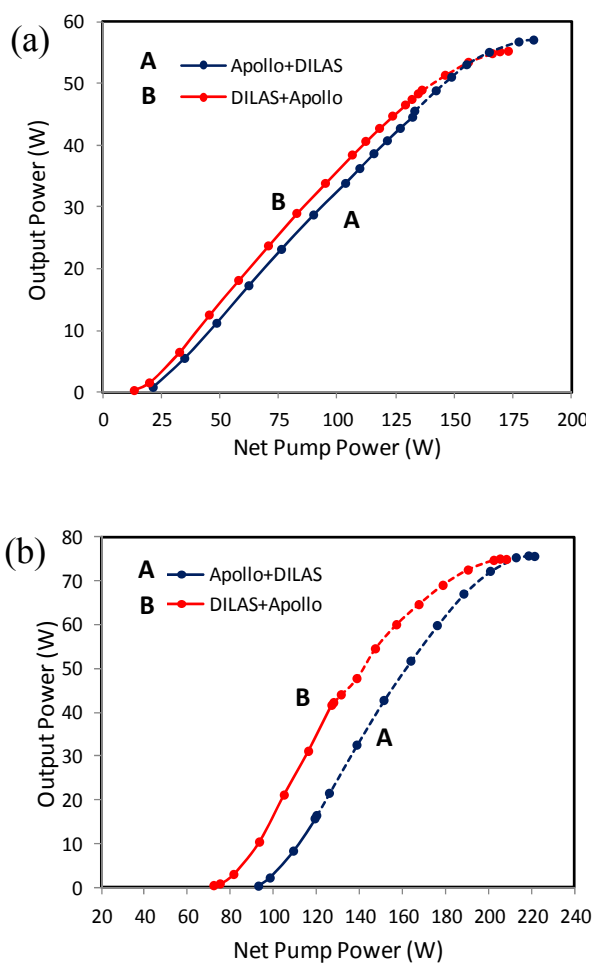


FIGURE 4.3 Power performance of the OPSL device pumped by two lasers with different contribution. (a) Before altering intensity profile of the DILAS laser. (b) After altering intensity profile of the DILAS laser.

Apollo laser (solid line) and 52 W DILAS laser (dashed line) while curve B denotes output performance of OPSL device pumped by 135 W DILAS laser (solid line) and 38 W Apollo laser (dashed line). When the OPSL device is pumped dominantly from the Apollo laser (curve A in the plot), the maximum achieved output power is 57 W. On the other hand, the maximum achievable output power is 55 W when the major pump power

is from the DILAS laser. The smaller achievable output power obtained from curve B indicates an inferior heating condition due to the high central intensity in the intensity profile of DILAS laser.

To address this issue, we altered the intensity profile of the DILAS laser by bending the output fiber and obtained the intensity profile shown in Fig. 4.2(b). By doing this, we are able to get an intensity profile close to what Apollo laser has. Fig. 4.3(b) shows the power performance of an OPSL device pumped by two lasers with different contributions. Curve A is primarily pumped by the Apollo whereas curve B is primarily pumped by the DILAS laser. No matter which laser contributes more pump power, the same maximum achievable output power is obtained. The two lasers are not an ideal top-hat profile, but they also don't have very high intensity at the center which can lead to premature thermal rollover.

4.1.2 Ratio of pump beam spot size to laser TEM₀₀ mode size

The cavity length of an optical resonator determines the fundamental transverse mode radius of the laser. For single transverse mode operation, the cavity is chosen so that the cavity mode size matches the pump spot size. On the other hand, the OPSL operates in multi-transverse mode if the cavity mode size is smaller than the pump spot size. In this case, a higher output power can be extracted.

Fig. 4.4 shows OPSL output performance for several cavity lengths. The OPSL device is pumped in the same area for the three power curves, and the three curves use the same output mirror which has 30 cm radius of curvature. By changing the cavity

length from 290 mm to 150 mm, the fundamental laser mode diameter changes from 267 μm to 445 μm resulting in changing the pump-to-mode size ratio from 3.15 to 1.88. From the power curves, the pump-to-mode size ratio of 3.15 gives the highest output power at 140 W net pump power and shows no sign of thermal rollover. On the other hand, the pump-to-mode size ratio of 1.88 has the lowest output power and the power curve starts bending at 130 W of net pump power indicating thermal rollover. As the result, a large ratio of the pump radius to the mode radius is favored for high power multi-transverse mode OPSLs.

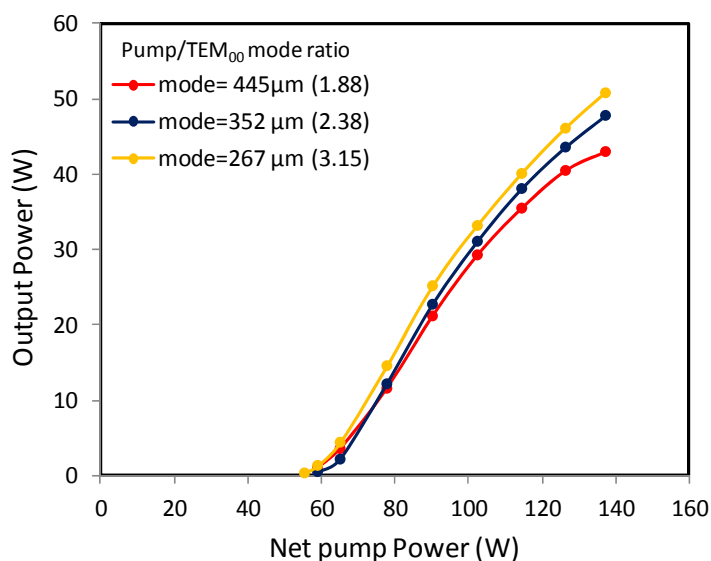


FIGURE 4.4 Power performance of OPSLs with different ratios of the pump radius to the mode radius.

4.1.3 Double-pass/single pass gain

In the previous section, we investigated how the pump-to-mode size ratio affects the power performance of OPSLs. In this section, we investigate the influence of double

passing the OPSL on the output performance. A V-shaped cavity with an OPSL device as a folding mirror for passing the OPSL twice per round trip is illustrated in Fig. 4.5. In this condition, the optimal output coupling is expected to be higher than that of the single pass configuration. To investigate the power performance and the optimal output coupling of an OPSL with double pass gain, several combinations of the two end mirrors with different reflectivities are used to obtain different output coupling. Fig. 4.6 shows the maximum achieved output power versus the output coupling. We see the maximum output power increases quickly with increasing output coupling from 4% to 7% and slowly increases from 7% to 10%. The best output coupling from the available mirror combinations is about 9.6% and the maximum output power is about 47 W. Conversely, a maximum output power of 47.5 W was achieved when a linear cavity (single passing the OPSL) is used. The optimal output coupling in this case is approximately 4.5%. A much higher optimal output coupling is needed for the OPSL with the double pass gain and a similar output power level is obtained. Since there is no difference in power performance, we use a linear cavity for simplicity.

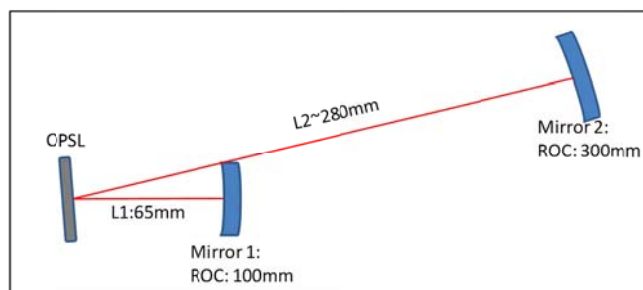


FIGURE 4.5 A V-shaped cavity for double passing the OPSL gain

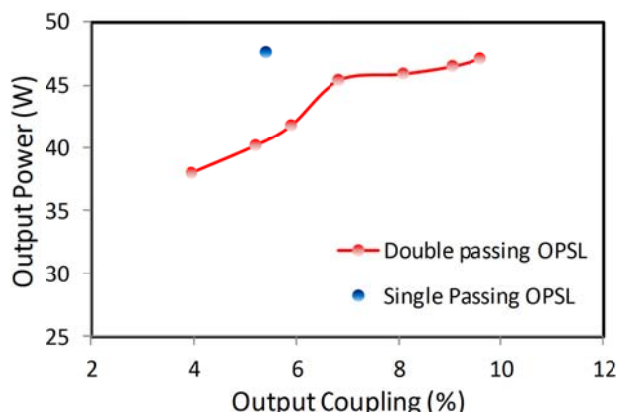


FIGURE 4.6 Maximum output power achieved using different output coupling.

4.2 Room temperature detuning

Careful design of the detuning between the quantum well absorption and the corresponding gain and the cavity resonance at room temperature is important for taking advantage of the enhanced gain provided by the micro-cavity effect. Based on the simulation shown in [56], a larger negative detuning at room temperature results in more pump power being needed to achieve enough effective gain to reach the laser threshold because of the spectral misalignment between the quantum well gain and the micro-cavity of the cold device. A larger negative detuning also leads to a higher optimal operation temperature and a higher temperature at roll-over. This increases the high-temperature tolerance of the device so a higher output power is expected. In this section, we discuss the influence of room temperature detuning on the power performance of OPSLs.

We used three OPSL devices processed from three different wafers that have a different amount of negative detuning at room temperature. Before the laser experiment, we measured the temperature dependent reflectivity (TDR) to understand their detuning characteristics. Fig. 4.7 shows the TDR spectrum of the three devices. As discussed earlier in Chapter 2, the center wavelength of the dip represents the strongest absorption wavelength enhanced by the micro-cavity resonance and the depth of the dip indicates the overlap between the quantum well absorption and the micro-cavity resonance. The optimal temperature for the electric field-quantum well interaction can be accordingly known from the temperature at which the TDR has the deepest dip. However, for a given temperature, the quantum well “gain” peak under high carrier density conditions is about 8-10 nm longer than the “absorption” peak at low carrier density and hence the optimal temperature for the light-quantum well interaction is about 30 K lower than the temperature at which the TDR has the deepest dip. From Fig. 4.7, we can see that the temperature at which the TDR has the deepest dip is around 100 °C, 120 °C, and > 120 °C for the three devices, so the optimal temperature for laser operation is about 70 °C, 90 °C and > 90 °C respectively. The room temperature detuning can be determined by multiplying the difference of spectral shift rates between the quantum well gain and the micro-cavity resonance by the difference between room temperature and the optimal temperature for operation. The calculated room temperature detuning for the three devices is about 12 nm, 18 nm and greater than 18 nm. Since a temperature higher than 120 °C was not applied in the TDR measurement to prevent indium solder softening, the exact value of the detuning cannot be deduced from the TDR. In fact, the room

temperature detuning of the last wafer is designed to be 34 nm.

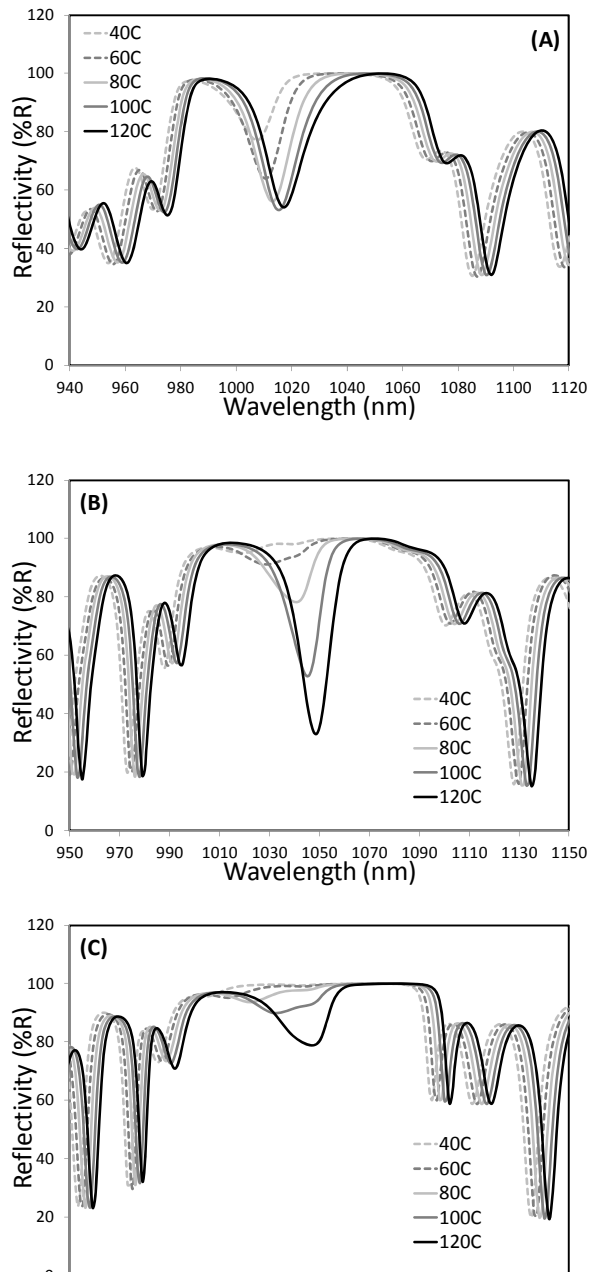


FIGURE 4.7 Temperature dependent reflectivity of three OPSL devices from three different wafers.

Fig. 4.8 shows the input-output curves of the three devices. Although much higher threshold pump power is required for the device with 34 nm of negative detuning, the output power increases rapidly with increasing pump power. The maximum achieved output power obtained from this device is 73 W, which is much larger than 57 W and 23 W obtained from the devices with 18 nm detuning and 12 nm detuning respectively. By comparing their lasing wavelength to the dip wavelength in the TDR spectrum, the temperature at the thermal roll-over can be determined. A roll-over temperature of over 120 °C is found in device with the largest detuning while it is about 95 °C in the device with 12 nm detuning. The device with a fairly large negative room temperature detuning shows a better high-temperature tolerance and is capable of high power generation.

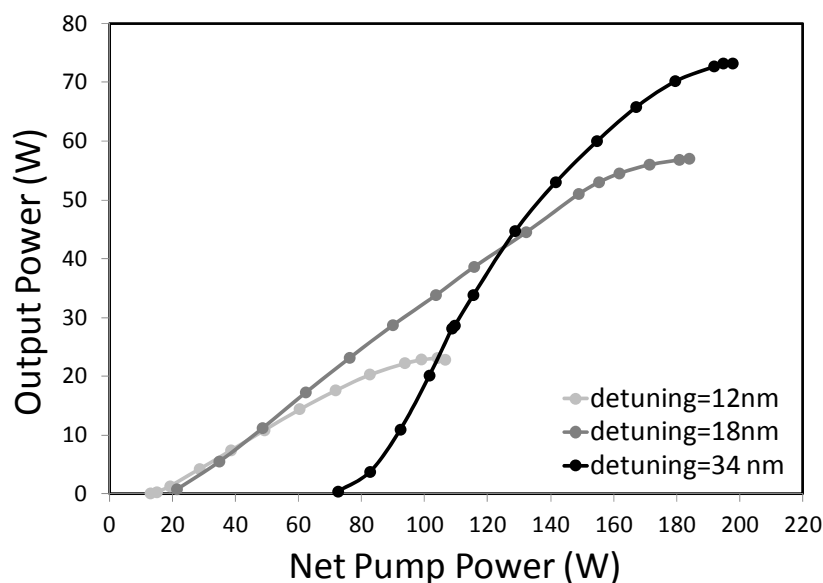


FIGURE 4.8 Output performance of the OPSSL devices with different amount of detuning.

4.3 Power scaling OPSLs

The major limitation to power scaling OPSLs is the heating issue which we discussed in Chapter 3. We analyzed the influence of the heat sink geometry, dimension of the diamond heat spreaders, the solder thickness and the geometry of the copper submount on the temperature rise in the QWs. Based on the simulation results and the discussions in the previous sections, an OPSL device including a 3.5×3.5 mm semiconductor chip (structure C) and a $8 \times 8 \times 0.6$ mm diamond heat spreader soldered on a new version of copper submount, is used for a power scaling experiment. The water temperature in the heat sink was set at 10°C . With several magnifications of the pump imaging optics, we scaled the pump spot diameter from $750\ \mu\text{m}$ to $1170\ \mu\text{m}$ ($1/e^2$). The OPSL device was pumped by the Apollo laser with a pump spot diameter of $750\ \mu\text{m}$. For a pump diameter larger than $750\ \mu\text{m}$, two pump lasers (Apollo and “bent” DILAS) are used to provide sufficient pump power. An 8.5 cm linear cavity having a concave output coupler with 10 cm radius of curvature gave a fundamental lasing mode diameter of $217\ \mu\text{m}$ on the OPSL device that was used under all pumping conditions.

This structure emits in the wavelength range between 1032 nm and 1040 nm from the lasing threshold to thermal rollover. The power curves of the OPSL pumped with different pump spot size are plotted in Fig. 4.9 (a) [72]. Due to the different core diameter and the availability of optics, the $750\ \mu\text{m}$ pump size is only available from the Apollo laser and the power curve shows a pump-limited output power of 60 W. An output power of 78 W was achieved by using $880\ \mu\text{m}$ pump diameter and 95 W was achieved by scaling the pump size to $1170\ \mu\text{m}$. A pump limited output power of 93 W was obtained

by further scaling the pump spot to 1500 μm (not shown here) and no indication of thermal rollover was observed. When the water temperature was set to 0 $^{\circ}\text{C}$, we achieved 103 W using a 1170 μm -diameter pump spot without damaging the OPSL device. Fig. 4.9 (a) also shows the corresponding theoretical output characteristics (dashed lines). One parameter required to generate these curves is the thermal impedance (R_{th}) of the OPSL device, which depends on the pump spot size according to the thermal simulation results we showed in Chapter 3. Consequently, based on the simulation data, we use a spot-size dependent but temperature independent value for R_{th} . The regions of the plots in Fig. 4.9 (a) closer to threshold that show deviations from the theory are likely due to lateral amplified spontaneous emission (ASE) or even lasing. From these power scaling results, we see that the output power increases with the pump area, but the output power is not linearly proportional to the pump area. Fig. 4.9 (b) shows the output power density versus the pump power density. It is clear that the output power from the larger pump beam shows rollover at lower pump intensities than that from the smaller beam although it gives a higher gross output power. In addition, we see that the threshold pump power density decreases with the pump beam size, indicating a higher temperature is induced by the same amount of pump power density in a larger spot size. The current OPSL device has a large amount of spectral detuning between the QW gain and the micro-cavity resonance and hence it requires more heating to achieve sufficient gain for the threshold condition. From Chapter 3, we know that a large pump beam causes a higher temperature at a constant pump power density, so threshold is easier to achieve when using a larger pump beam.

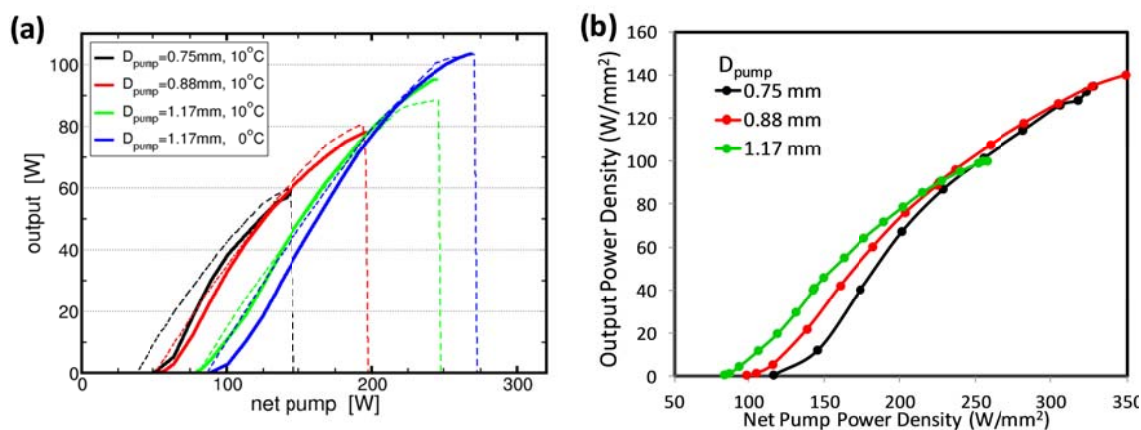


FIGURE 4.9 (a) Power scaling of 1040 nm OPSLs. Solid bold lines: experiment; thin dashed line: theory. (b) Power density curves in W/mm^2 .

In Chapter 2, we showed that reduction of the cap layer thickness can shift the micro-cavity resonance to a shorter wavelength and hence reduces the room temperature detuning between the QW gain and the micro-cavity resonance. Fig. 4.10 presents the output characteristics of an OPSL chip from structure C but with the InGaP cap layer further etched 40 nm for three heat sink temperatures [74]. The device now emits at 1019 nm at lasing threshold and 1028 nm at thermal rollover. The over-etched OPSL chip was pumped by a 920 μm diameter pump beam (FWHM) from a 808 nm fiber coupled laser with 600 μm diameter. From Fig. 4.9 and Fig. 4.10, we can clearly see that the lasing threshold is greatly reduced from 90 W to about 50 W and that the slope efficiency is also reduced due to reduction of room temperature detuning. The maximum achieved output power of 106 W was obtained at a heat sink temperature of 3°C , indicating of good thermal management and no significant surface degradation after over-etching.

In this chapter we have demonstrated over 100 W of power from a single OPSL device. We believe an OPSL with kilowatts of power may possibly be realized by scaling OPSL devices. Further improvements in beam quality, pump efficiency and external efficiency are discussed in the following chapters.

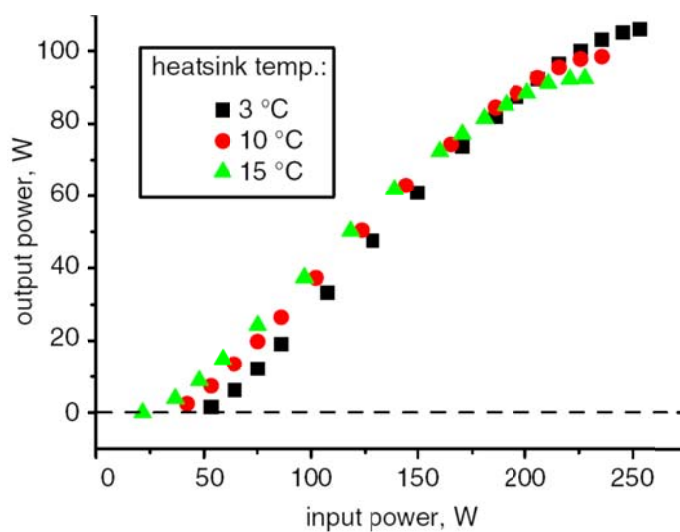


FIGURE 4.10 Output performance of the over-etched OPSL device pumped by a 920 μm spot from a single 808 nm fiber-coupled laser.

CHAPTER 5 EFFICIENCY IMPROVEMENT OF OPSLS

In addition to optical power, high optical conversion efficiency is also a desired laser property. In this chapter, we use two separate approaches to improve optical efficiency and external efficiency of high power OPSLS.

5.1 Double Pass Pump Design

For standard barrier pumped, InGaAs-based 1- μm OPSLS, single-pass pump absorption is about 80%, depending on the number of QWs. The remaining pump light propagates through the DBR and is absorbed in it or in the metallization layers behind the DBR, or both. In our high power OPSL devices discussed in Chapter 4, the DBR structure is composed of GaAs/AlAs which has substantially high absorption at the 808 nm pump wavelength. The single-pass pump absorption in our structure is about 80% and the residual pump (20%) is absorbed and converted to heat in the DBR structure. This heating in the DBR structure could reduce heat removal efficiency and therefore the laser output performance. In output performance simulations [56], we found that the maximum output power can be improved by over 100% if all net pump power is absorbed in the active region (shown in Fig. 5.1). The reduction of pump loss in the structure not only improves the optical efficiency but also reduces generated heat, leading to thermal rollover at higher pump power levels. In Fig. 5.1 we also show the calculated power characteristic curves of the OPSL structure with different numbers of quantum wells. By

increasing the number of QWs, the pump absorption in a single-pass is increased so the output performance is improved accordingly. Increasing the number of QWs from 10 to 16 increases the pump absorption in the active region from 80% to 91% resulting in 50% improvement in output power. However, we assume all QWs are pumped equally in the simulation and this might not hold for a very long active region. Not as much pump is left to be absorbed deeper in the structure, so deeper wells are not pumped as hard. Moreover, the heat transfer path is increased so that heat removal efficiency is decreased.

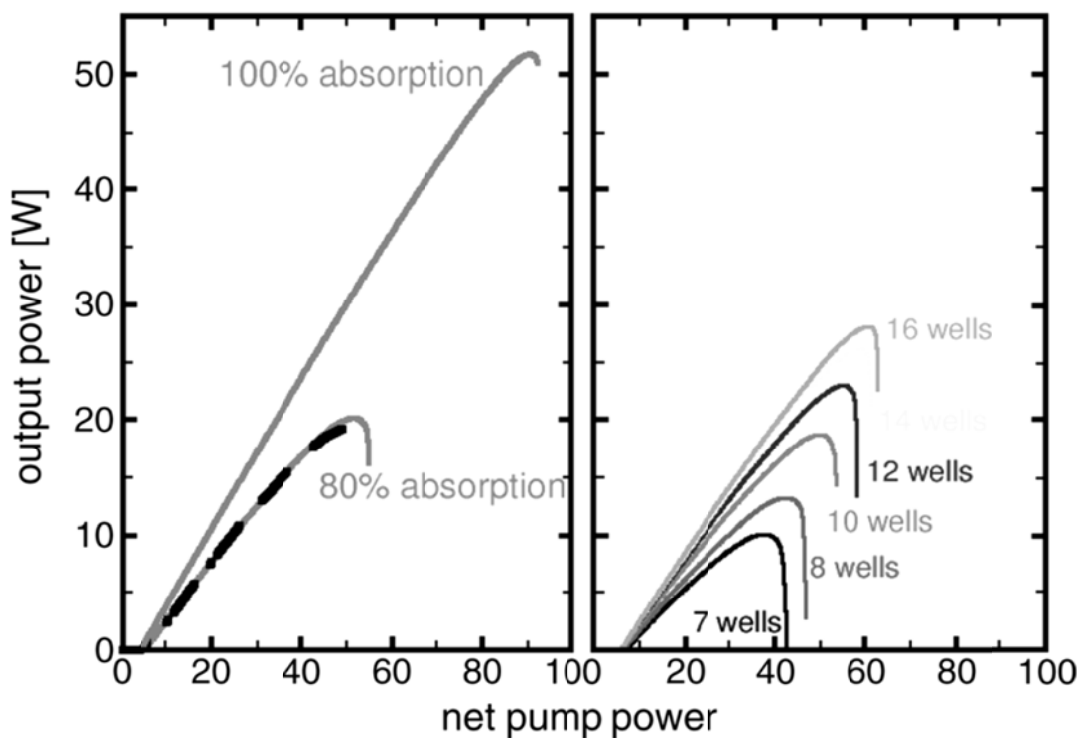


FIGURE 5.1 Left: calculated power characteristic curves for OPSLs with 80% and 100% pump absorption in the active region. Right: calculated power characteristic curves of OPSLs with different numbers of QWs.

Other approaches to improve the pump absorption efficiency in the active region include double passing the incident pump beam. This can be achieved by designing the DBR structure to have high reflection at both the pump and the laser wavelength [24, 25]. The DBR stopband shifts with the cosine of the incident angle to shorter wavelength. The incident angle of the pump can be chosen so that the cosine of the internal angle equals the ratio of the pump to the laser wavelength. Therefore, in order to achieve sufficiently high reflectivity at the pump wavelength in the DBR, the OPSL device can only be pumped at the optimized angle. This is a drawback, since a large incident angle is needed for OPSLs when the pump wavelength and the laser wavelength are far apart. In this case, extra effort is required to maintain a circular pump aperture on the device surface.

An alternate method of reflecting the pump removes the requirement for the DBR to reflect both the pump and the laser wavelength. In this approach, which we used in the results reported here, the DBR reflects the lasing wavelength and is transparent to the pump wavelength. This is done by using AlGaAs/AlAs, which is transparent at the 808 nm pump wavelength for the DBR structure. An Au-In alloy layer deposited on the back of the DBR then reflects the pump back through the structure for a second pass. As we mentioned in Chapter 2, a layer of 100 nm of Ti or Cr is used for better Au adhesion. This layer also absorbs the pump, so in order to minimize heating only 5 nm of Cr was used. This reduced the round-trip pump absorption in the Cr layer from > 99 % to 30 %. Reflecting the pump has two advantages; it reflects the pump back through the structure so that more of the pump light is absorbed, and secondly it reduces the temperature of the device since there is less heating due to absorption of the pump in the DBR.

Fig. 5.2 shows the double-pass pump scheme. 30% of the pump light is reflected from the air/semiconductor interface, of the net pump that is transmitted into the device, 80% is absorbed on the first pass through the device. We estimate that 70% of the light that reaches the metal alloy layer is reflected. Of this reflected light, 80% is absorbed in the second pass through the device. Thus the net absorption of the net pump light is $0.8 + 0.7 \times 0.2 \times 0.8 = 0.8 + 0.112$. This amounts to an increase in absorption of the pump of 14 %.

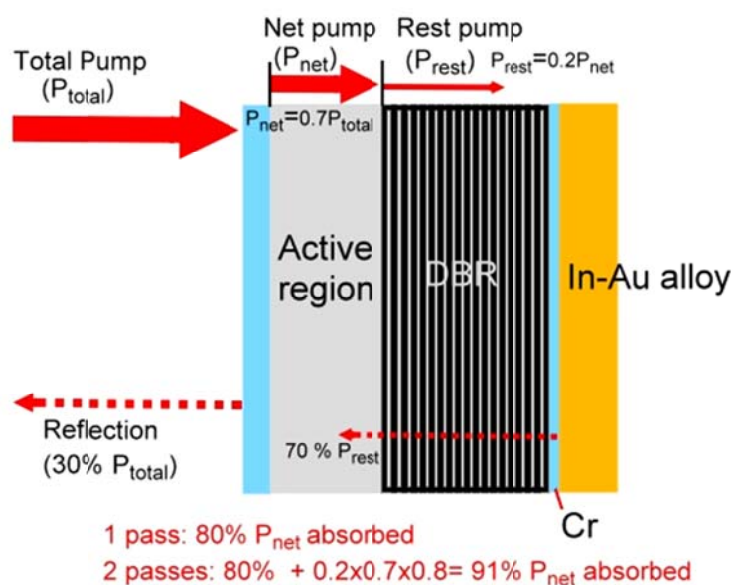


FIGURE 5.2 The OPSSL structure with the double pass pump design.

To investigate the performance improvement from the double pass pump design, two OPSSL devices with 5 nm and 100 nm Cr adhesion layer in front of the Au layer, respectively, were processed and their performance is compared in Fig. 5.3. The devices

were tested by using a 8 cm-linear cavity with a concave output mirror with 10 cm radius of curvature. The pump beam was 820 μm in diameter and the heat sink temperature was 10 $^{\circ}\text{C}$. The maximum achieved power for the device without the double pass pump design is 23 W at a net pump power of 107 W while the maximum achieved power for the device with the double pass pump design is 50 W at a net pump power of 142 W. The maximum optical conversion efficiencies of the two devices are 25% and 42%, respectively, with respect to the net pump power, defined as the incident pump power minus the reflected pump power. 10% more net pump power is absorbed in resonant periodic gain (RPG) resulting in a higher output power at the same net pump level. Moreover, with the absence of pump absorption in the DBR, less heat is produced during laser operation also improving the output performance.

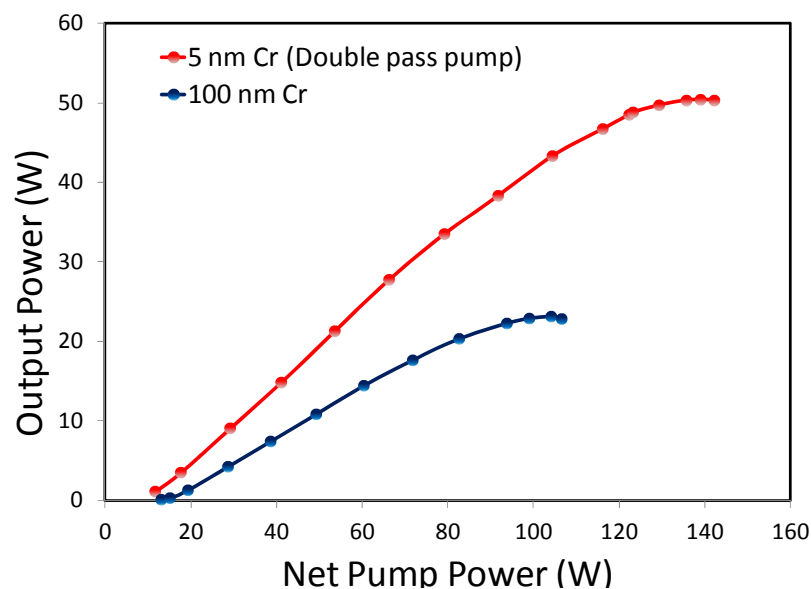


FIGURE 5.3 Output performance of OPSL devices with/without the double pass pump design.

5.2 Pump Anti-reflection Coating (PARC)

In a typical OPSL structure, quantum wells are placed at the standing wave anti-nodes of the optical field to provide RPG for maximizing gain. Since maximum amplification occurs for those modes that have the best overlap between their maxima and the QWs, the lasing wavelength is influenced by the spacing of the wells. This wavelength selection effect is more prominent when the refractive index contrast is high at the semiconductor-air interface. During laser operation, the generated heat causes refractive index changes of the semiconductor structure leading to a shift of the mode (micro-cavity resonance) and therefore, the lasing wavelength. Furthermore, the effective gain which depends on the overlap between the QW gain and the micro-cavity resonance is affected by the temperature as well. The OPSL performance is sensitive to temperature as we discussed in Chapter 3. Anti-reflection coating the semiconductor surface at the laser wavelength has been suggested as a way to decrease the micro-cavity effect, making the OPSL device more insensitive to temperature excursions. The common way to accomplish an anti-reflection coating is to deposit a layer of material with a refractive index between those of air and the semiconductor cap layer. The thickness of the coating material is usually chosen to be a quarter wavelength of the operating laser so the optical field changes its phase by 180° after double passing this layer. Thus, if the mode had a maximum at the air interface without the coating, it will have a minimum with the coating. As the result, the OPSL structure no longer has high lasing-mode selection and also operates at modes which don't have their maxima in the QWs. This leads to a reduction of the effective gain and a wider lasing spectrum. Anti-reflection coating the

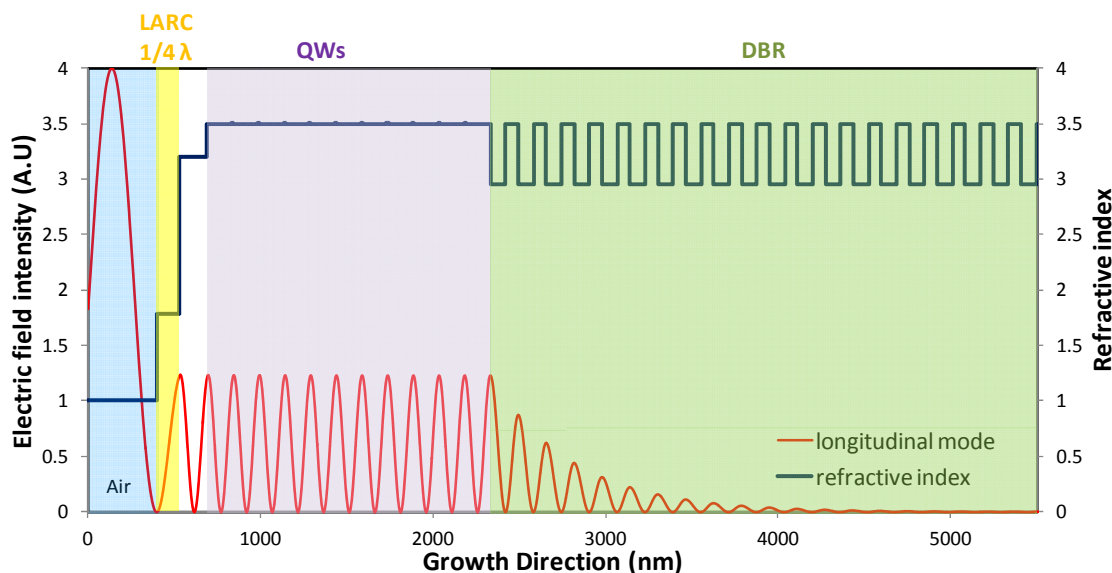


FIGURE 5.4 Refractive index profile (blue) and 1040 nm lasing mode (red) for an OPSL operating at 1040 nm at 375 K.

semiconductor surface is also commonly used for OPSL structures where the PL peak and micro-cavity resonance are misaligned. In this case, the reduction of lasing wavelength selectivity due to the anti-reflection coating improves laser performance. However, in general, OPSL structures which are well-designed and grown properly perform better without an anti-reflection coating since they can take advantage of the enhanced effective gain. Fig. 5.4 shows the refractive index profile and the standing wave pattern for an OPSL with laser wavelength anti-reflection coating (LARC) operating at 1040 nm at 375 K; the coating material used here is silicon nitride (Si_3N_4). The optical field intensity inside the active region is obviously reduced compared to the optical field intensity we show in Fig. FIGURE 2.9. The reduced optical field leads to a reduction in the effective gain. Therefore, higher carrier density/net pump power is required to reach

the lasing threshold, leading to more heating and a reduction in optical efficiency or even the maximum achievable output power. Moreover, without the enhancement of the effective gain, fairly low output coupling is required to achieve high power output resulting in a loss-sensitive cavity. Any loss due to added optical components will significantly reduce output power performance.

Fig. 5.5 presents the input-output power curves of the OPSL structure C (introduced in Chapter 4) with and without LARC. The device was tested by using a 8 cm-linear cavity with a concave output mirror with a 10 cm radius of curvature. The pump spot was 820 μm in diameter and the heat sink temperature was 10 $^{\circ}\text{C}$. As we mentioned in Chapter 4, the optimal output coupling for an uncoated OPSL device is about 4-5%. However, the output rolled over quickly when we used a 4% mirror when testing the OPSL with a LARC. The best output performance obtained from available mirrors in our lab was about 34 W with a 1.5 % out-coupling mirror. On the other hand, over 55 W of output power was achieved from the same OPSL device without a LARC by using 5 % out-coupling. From the figure, we can see that the threshold is very high for the OPSL device without a LARC. This is because of the adopted large detuning design for making device work better at high temperatures, resulting in thermal rollover at higher pump power levels. Other than this aspect, the output performance is much better without the LARC. Although the out-coupling is not optimized for the OPSL device with the LARC, it is unlikely that it can reach the same output power level as the OPSL without the LARC even when an optimized out-coupling is used.

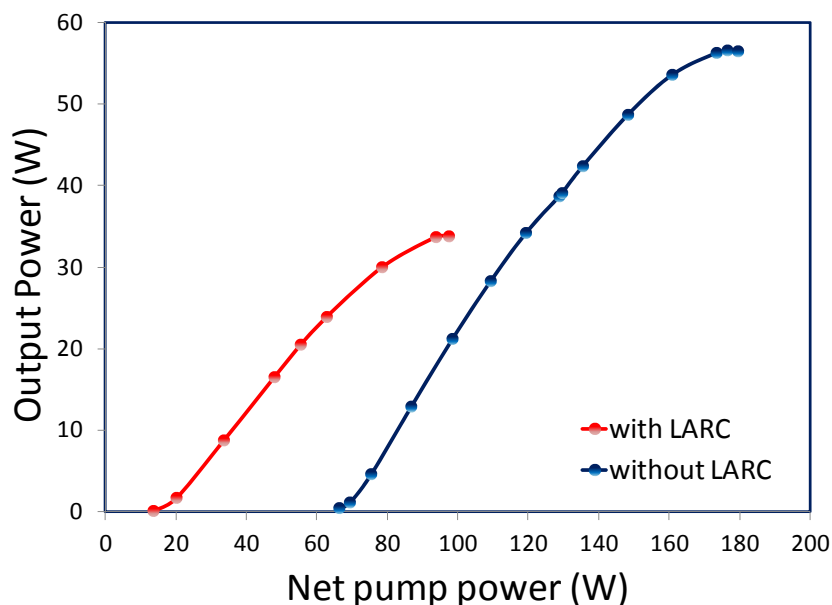


FIGURE 5.5 Input-output curves of an OPSL device with and without a LARC.

The reduction of the reflection at pump wavelength is the most important positive influence the LARC will usually have, other than improving the effect of spectral misalignment between the micro-cavity resonance and the QW gain. The reduction of the pump reflection at the semiconductor-air interface leads to an improved external efficiency. To maintain the benefit of effective gain enhancement and improve the external efficiency at the same time, we apply a specially designed anti-reflection coating for the 808-nm pump wavelength at the semiconductor surface. As we mentioned earlier, a conventional anti-reflection coating is achieved by depositing a layer of material of quarter wave thickness at the target wavelength. By doing so, not only the pump reflection is eliminated but also the reflectivity at the laser wavelength is diminished leading to the reduction of the micro-cavity resonance effect and thus the effective gain.

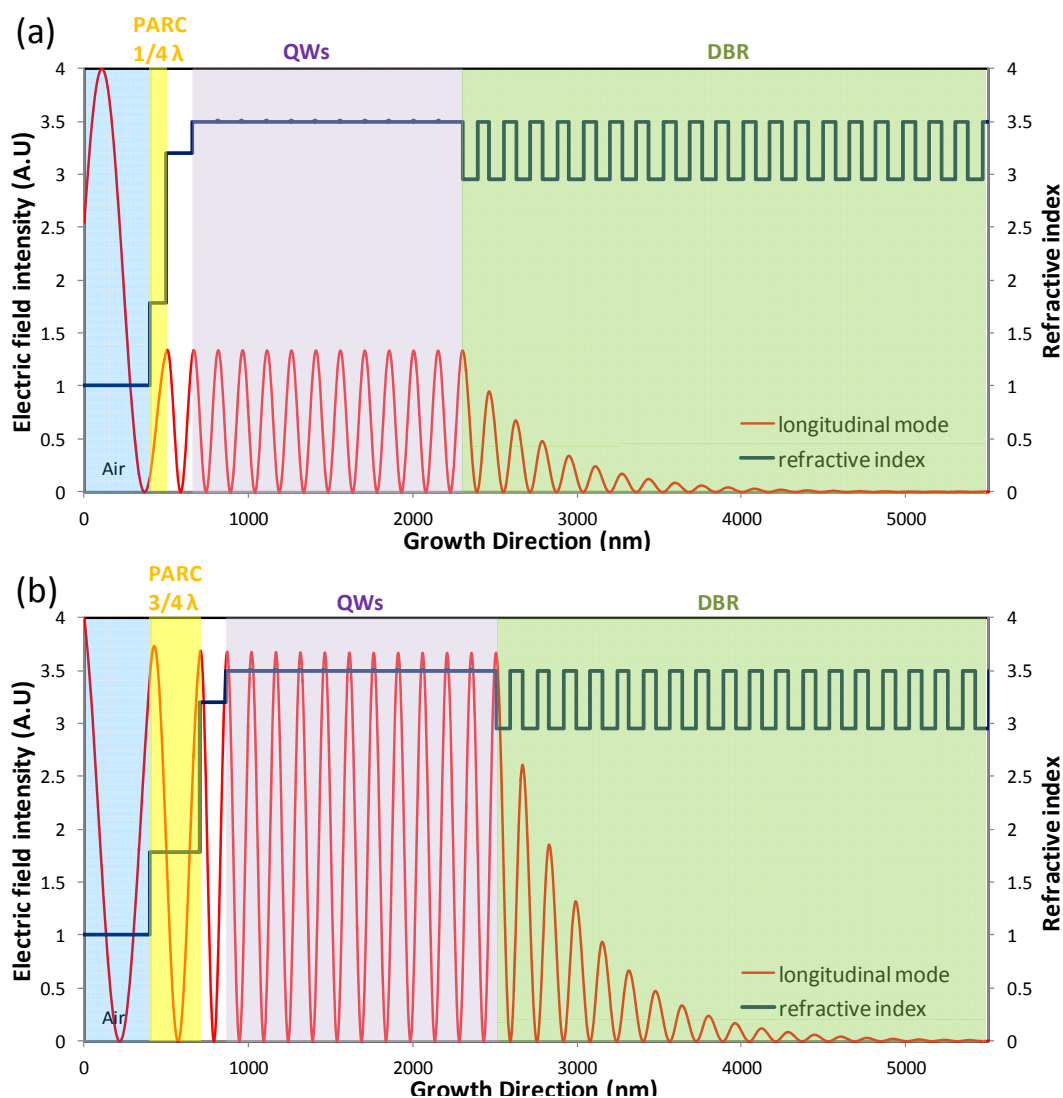


FIGURE 5.6 Refractive index profile (blue) and 1040nm lasing mode (red) for an OPSL operating at 1040 nm at 375 K (a) with a quarter wavelength thick anti-reflection coating for the pump wavelength at 808 nm (b) with three quarter wavelength thick anti-reflection coating for the pump wavelength at 808 nm (the new PARC).

In contrast, the new pump anti-reflection coating (PARC) is based on a lower index material with an optical thickness of three fourths of the pump wavelength, corresponding to nearly half of the lasing wavelength. Thus, the new PARC eliminates

only the pump reflection and the laser mode still has its maximum at the semiconductor-air interface. Fig. 5.6 shows the refractive index profile and the laser standing wave pattern for (a) a 1040 nm OPSL with conventional Si_3N_4 anti-reflection coating at the pump wavelength (808 nm) and (b) with the new PARC which has a thickness of three fourths of the pump wavelength. Like the LARC, the optical intensity is low when the conventional anti-reflection coating is applied to the OPSL surface. Furthermore, the laser mode has its minimum at the semiconductor-air interface so the resulting configuration no longer has high mode selectivity. On the other hand, the OPSL device with the new PARC design has similar optical intensity to the uncoated device inside the active region. The lasing mode which has its maxima at the QWs experiences an enhanced gain and hence is preferred during laser operation.

To investigate the effect of the new PARC design, we compare the TDR and the output performance of an OPSL device processed from structure B. In the TDR shown in Fig. 5.7, the absorption dip of the OPSL device with the PARC has similar reflectivity compared to the same device before coating. This indicates that the micro-cavity effect is not reduced much so the absorption is still enhanced at the resonant wavelength. We also find that the detuning of the OPSL device with the PARC is larger than it was without the PARC. The deepest absorption dip now occurs at 110 °C instead of 90 °C and the spectral position of the dip is now at a longer wavelength. This is due to the additional optical path in the PARC layer and can be corrected by using a thinner cap layer. Overall, the TDR does not change significantly before and after applying the PARC. The micro-cavity effect is retained so we expect a similar output power can be obtained from the

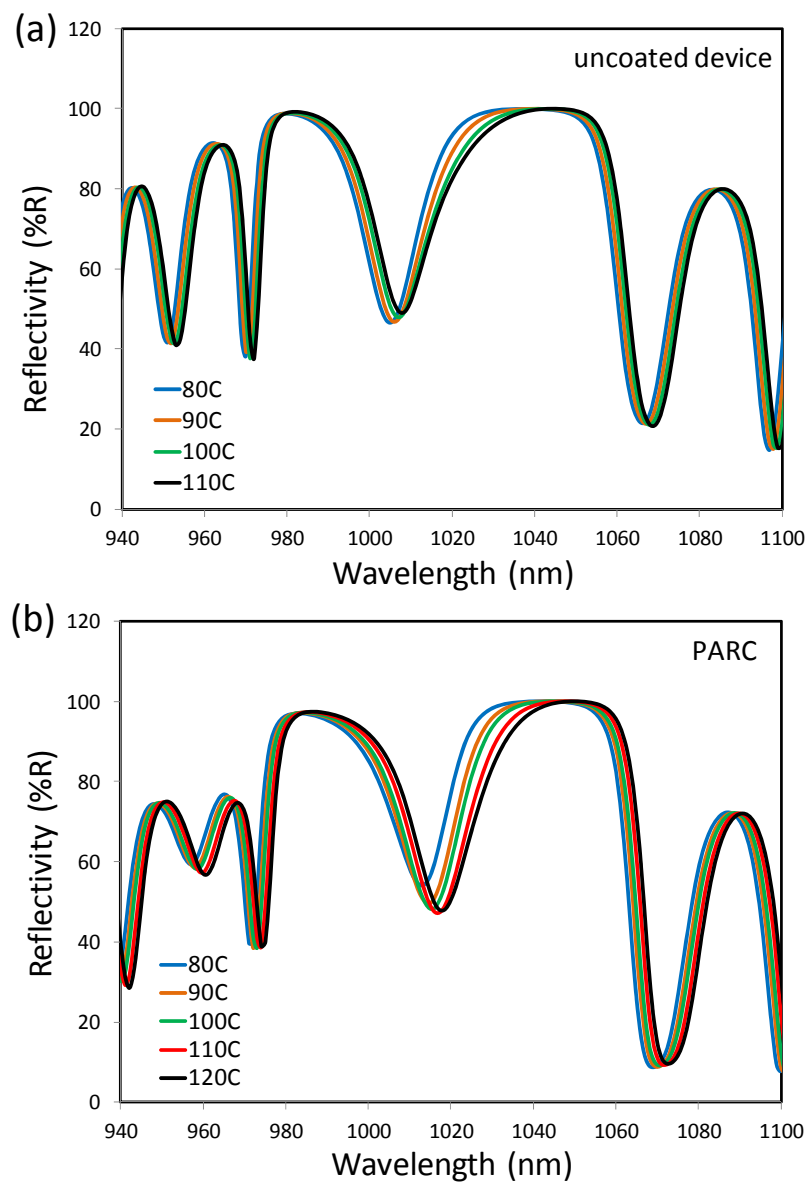


FIGURE 5.7 TDR of the OPSL device with and without the $\frac{3}{4} \lambda$ PARC.

device with the PARC.

In the laser experiment, we found that the reflectivity of the pump decreased from about 30 % to 3 % after the PARC was applied. Thus, more net power actually enters and

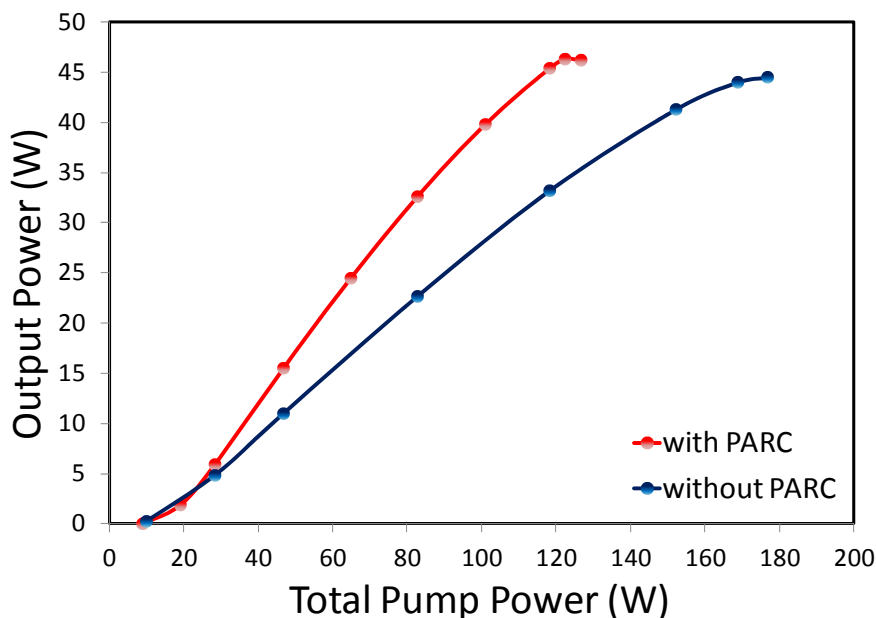


FIGURE 5.8 Output characteristics versus total pump power for an OPSL device with and without the $\frac{3}{4} \lambda$ PARC. The device was tested by using an 8 cm-linear cavity with a concave output mirror with 10 cm radius of curvature. The pump spot was 820 μm in diameter and the heat sink temperature was 10 $^{\circ}\text{C}$.

pumps the device for a given amount of gross pump, leading to higher external efficiency. The total pump power-output power curves are shown in Fig. 5.8. Both curves were measured from the same spot on the OPSL device. The pump spot was 820 μm in diameter and the heat sink temperature was 10 $^{\circ}\text{C}$. The maximum achieved output power was about 45 W for both devices with 4.5 % output coupling. The same optimal output coupling found in the OPSL device with the PARC indicates that the micro-cavity is still maintained. We expected a lower threshold to be required for the OPSL device with the PARC. However, a similar threshold power was measured in the experiment. The changes we found in the micro-cavity resonance from the TDR might be the major cause

of the higher threshold found in the PARC device. Since the detuning is found to be larger, more heating is needed to align the QW gain and the remaining micro-cavity resonance for reaching sufficient gain for threshold. Above threshold, the OPSL device with the PARC consistently has a higher output power at the same gross pump power compared to the OPSL without the PARC. 39% maximum optical-to-optical efficiency was achieved with respect to the total incident power whereas it was 28% without the PARC. From these results, the PARC demonstrates its ability for improving the external efficiency without deteriorating the effective gain and thus the maximum achievable output power.

CHAPTER 6 HIGH PEAK POWER OPERATION OF OPSLS

In Chapter 4, we demonstrated high power OPSLs in continuous wave (CW) operation. The major limitation to the maximum achievable output power is device heating. By pulsed pumping the OPSL device, output peak power can be significantly increased because of a reduction in the average heating power. In this chapter, the strategies for generating high peak power are discussed and the output performance of the OPSL under different operating conditions is compared.

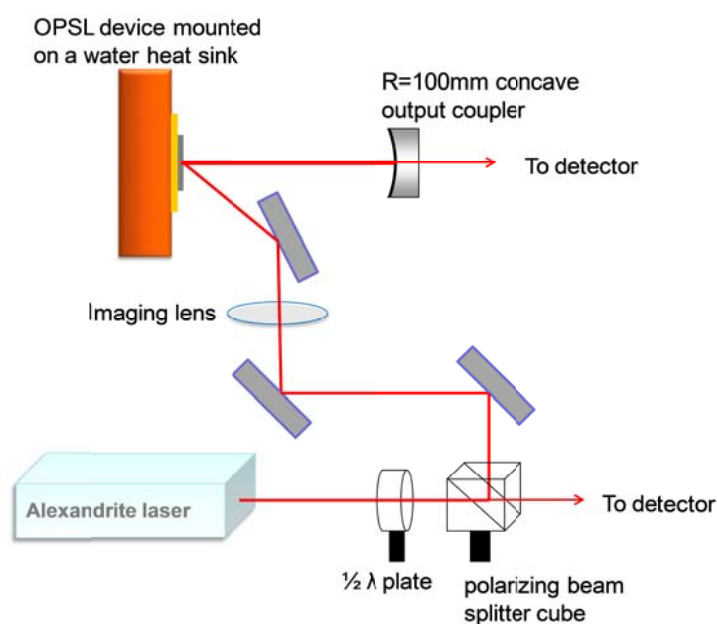


FIGURE 6.1 Experimental setup for the OPSL pumped by an alexandrite laser.

6.1 Experimental Setup

OPSL devices used in pulsed operation use structure B, which has 18 nm of room temperature detuning as we discussed in Chapter 4. Such detuning indicates a good match of the intrinsic QW gain and the micro-cavity resonance at a temperature of about 90 °C. The OPSL chip was soldered to 500 μm -thick CVD diamond for heat spreading and a water-cooled copper heat sink was used to control the heat sink temperature. As in OPSL experiments mentioned earlier, a simple linear cavity was used in this experiment. The output mirror transmission is 4 % at the laser wavelength at 1040 nm. We have two different pump sources available for generating pulsed OPSLs. One is the DILAS diode laser operated in a pulsed mode, with the available pulse width in this operation mode ranging from 40 μs to 32 ms. The pulse period can be set from 200 μs to 65 ms. To minimize the generated heating during laser operation, the smallest pulse duration (40 μs) is used in this experiment. With a pulse period of 64 ms, the pump laser repetition rate is about 15 Hz. Under this operating condition, the DILAS laser is able to deliver up to 180 mW of average power and 288 W of corresponding peak power. The pump spot size from the DILAS laser on the OPSL chip is about 800 μm in diameter and the pump intensity profile is shown in Chapter 4. The other pump source is a lamp-pumped alexandrite laser operating at 755 nm with a repetition rate of 3 Hz. This low duty cycle ensures sufficient time for OPSLs to dissipate heat before each new pump pulse. The pulse duration can be varied by changing the pump rate of the alexandrite rod. Higher pump rates generate shorter pulses which are ideal for reducing device heating. However, higher order transverse modes are generated at higher pump rates and make the pulse trains unstable.

To obtain stable pulse trains, the alexandrite laser was operated at a pump rate close to the lasing threshold. For this condition, the pulse duration is varied from 1 μs to 700 ns depending on the pump rate. Fig. 6.1 shows the experimental setup with the alexandrite laser as the pump laser. The output from the alexandrite laser first propagates through a half wave plate and a polarizing beam splitter cube. The pump power from the alexandrite laser is adjusted by rotating the half wave plate. The pump beam is then focused by an imaging lens to form a 1 mm-diameter spot on the OPSL surface. Since the alexandrite laser operates in TEM_{00} mode near the threshold, the transverse intensity profile is of Gaussian distribution.

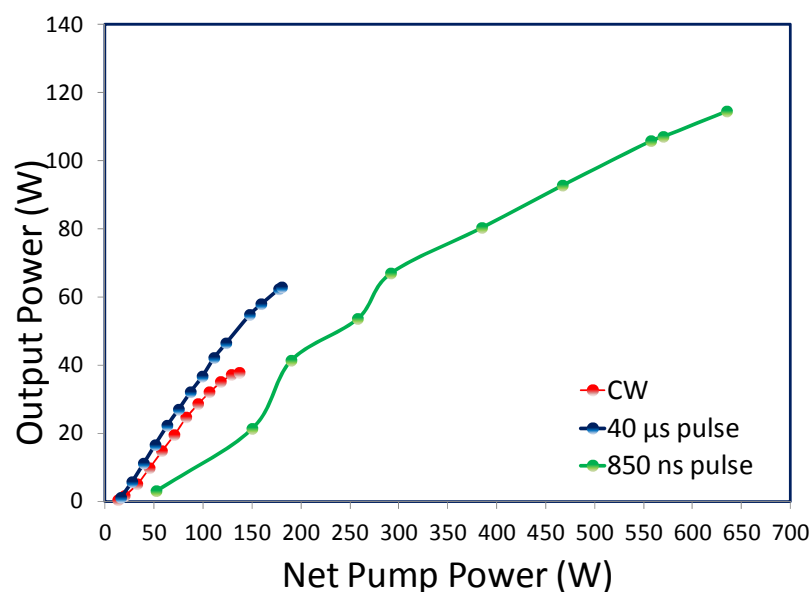


FIGURE 6.2 Power performance of OPSL in CW and pulsed operation.

6.2 Results and Discussion

The input-output power curves of the OPSL in CW and pulsed operation are shown in Fig. 6.2. For this experiment, a 75 mm linear cavity was used and the heat sink temperature was set at 20 °C. The red and the blue curve are respectively the OPSL output generated for the DILAS laser pumping in both CW mode and 40 μ s-pulse mode. The green curve is the output from the OPSL pumped by the alexandrite laser with 850 ns pulse width. The output performance for 40 μ s pulse pumping shows similar slope efficiency compared to CW pumping, but it shows no sign of thermal roll-over for a (peak) pump power of 150 W where CW output starts decreasing. A reduction of heating by using 40- μ s pump pulses leads to pump limited output power of 62 W. The heating reduction is even more significant when the 850 ns alexandrite pump pulse is used. A maximum peak power over 110 W is reached without thermal roll-over for peak pump power of 635 W indicating a minimum heating among the three curves. Indeed, simulation of the maximum temperature rise in the active region shows over 15 °C of temperature reduction for a pump peak power of 1-kW when decreasing pump pulse duration from 850 ns to 750 ns [75]. From the results shown above and the simulation, the output power should be improved if a shorter pulse is used to pump the OPSL device.

As observed before with a 2 μ m GaSb based device [33], the use of shorter cavity length leads to a shorter laser build-up time. Moreover, higher peak power is obtained from a shorter cavity length. To investigate this, we compared the pulse shapes and the output power from 45 mm and 75 mm cavities (shown in Fig. 6.3). The alexandrite laser pump pulse with 850 ns pulse width is used for both cavity configurations. The pulse

shapes observed from an oscilloscope show no obvious difference in the output threshold. Output pulses from both cavity configurations follow the pump pulse without significant delay indicating that the OPSL reaches threshold very early in the pump pulse (shown in the inset of Fig. 6.3). However, slightly better performance is observed from the shorter cavity as observed in ref. [33]. This effect might be attributed to an increase in the photon lifetime and thus of the intra-cavity photon saturation number, which leads to a longer build-up time. We noted that although a larger pump/laser mode size ratio is preferred in CW, multi-transverse mode operation, this preference is not obvious for pulsed operation.

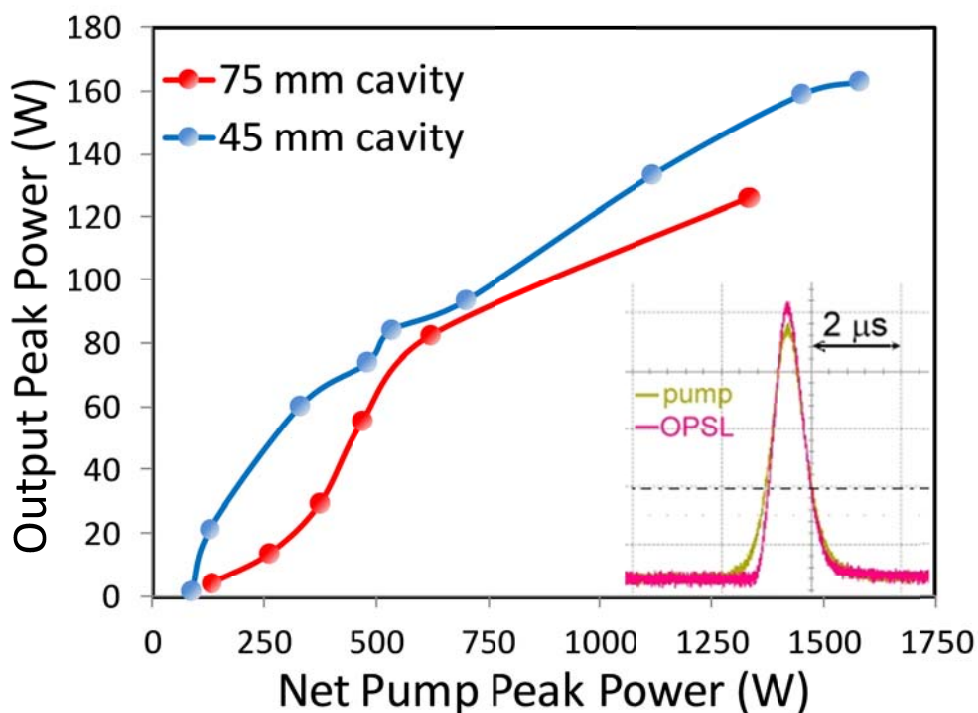


FIGURE 6.3 OPSL performances for different cavity configuration. Inset: 830 ns (FWHM) pump pulse (olive), the OPSL pulsewidth is 750 ns (pink).

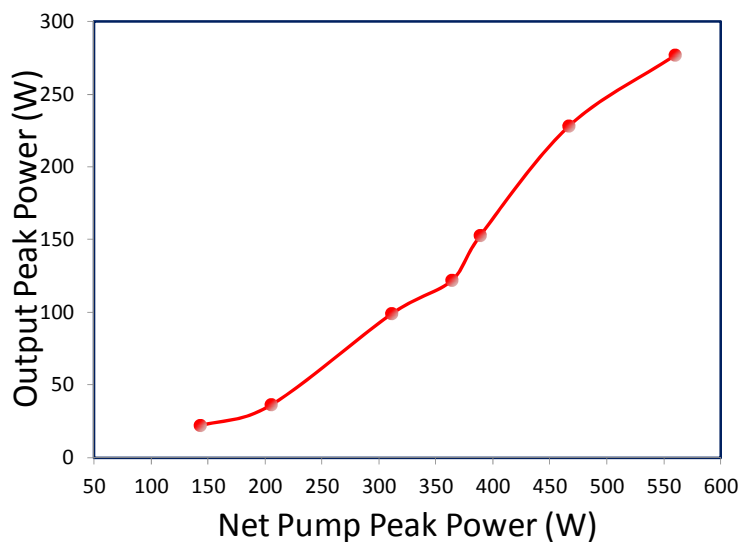


FIGURE 6.4 OPSL output with over 270 W peak power.

For another OPSL device which has a maximum output power of 61 W in CW operation, a maximum peak power of over 270 W was achieved using 750 ns pump pulses (Fig. 6.4). The cavity length used in this experiment is about 4 cm giving a fundamental mode about 255 μm diameter on the OPSL device. Although the device did not show thermal roll-over, permanent damage occurred when further increasing the pump power. Since the pump average power is low, the damage should not be heating-induced. One possibility would be a microscopic defect inside the pump area so that the damage threshold is much lower than the typical damage threshold. We also suspect that the unstable output of the alexandrite laser at a higher pump rate leads to an inhomogeneous pump intensity across the pump area. High intensity spikes from the unstable pump laser can cause local heating and result in partial melting or cracking of the OPSL surface. To solve the stability issue, an intra-cavity aperture was inserted in the

alexandrite laser cavity to force the laser to operate in the TEM₀₀ mode without fluctuation. Using an 820 ns pump pulse, a maximum peak power of 355 W was obtained [75]. Further improvement in the output performance to a peak power of 400 W was achieved by reducing the pump pulse width to 400 ns [75]. The maximum achieved power is still limited by laser induced permanent damage, and the next possible improvement will result from improving the surface quality of the OPSL device to increase the damage threshold.

CHAPTER 7 HIGH POWER TEM₀₀ MODE OPERATION

It has been a big challenge for conventional semiconductor lasers to achieve high power while simultaneously maintaining near-diffraction-limited beam quality. For edge-emitters or VCSELs, the output power is restricted to a few hundred milliwatts due to the small output beam diameter which easily causes facet damage. Although the external output mirror allows a NECSEL to operate at a larger mode diameter, the highest output reported is less than 1 W owing to the difficulty of uniform current injection over a large area. OPSLs have features of semiconductor lasers but do not suffer from limitations in the pump or mode area as conventional semiconductor lasers do. Uniform and scalable optical pumping together with the controllable cavity mode size of the external cavity configuration enables OPSLs to achieve more than 20 W of CW power in the fundamental transverse mode [76][24]. Here we demonstrate an OPSL providing 27 W CW power with beam quality M^2 1.1 and 34.5 W with $M^2 < 1.4$. To our knowledge, this is the highest output power ever reported for OPSLs in near fundamental mode operation.

7.1 Optical Resonator Design

For OPSLs, the optical pump beam spot serves as a soft aperture constraining the maximum allowable laser mode size on the OPSL device. The fundamental transverse mode (TEM₀₀) size is determined by the geometry of the external cavity of the OPSL. When the size of the pump aperture on the OPSL is larger than the size of the TEM₀₀ mode, the OPSL will tend to operate in a multi-transverse mode. On the contrary, single

transverse mode operation is preferred when the pump aperture is about the same size as the TEM_{00} mode. In order to achieve high power and single mode operation, the pump aperture and the mode size should be scaled simultaneously. In this way, the heat load per unit area decreases while the large fundamental mode size on the OPSL device ensures a high mode-discrimination between the TEM_{00} mode and higher order modes.

In Chapter 4, a simple linear cavity was used for high power OPSLs operating in multi-transverse modes. This cavity can also be used for fundamental transverse mode operation by properly choosing the mirror curvature and the cavity length to match the TEM_{00} mode size to the pump spot size. However, a very large curvature mirror and a long cavity are required to fulfill the need of a mode size near 1 mm for power scaling, leading to an inconveniently long system. Furthermore, the large curvature mirror plus the flat OPSL increases the difficulty of aligning the cavity. A common approach to increase the cavity mode volume but maintain a compact system size is to use a folded cavity. A V-shaped cavity is often used for OPSLs operating in the fundamental transverse mode [73, 77]. When using a concave mirror as the folding mirror in a V-cavity to create a large laser mode, the system will have substantial astigmatism, which gives an elliptical mode shape on the OPSL surface. Using a large curvature folding mirror may solve this problem but again, the system will be difficult to align and be more sensitive. One can also use the OPSL chip itself as the folding mirror to eliminate the astigmatism. In this way, the OPSL is passed twice in a round trip resulting in higher gain so a higher optimal out-coupling is expected. In addition, the laser now propagates with an angle inside the OPSL structure so the DBR reflectivity and the micro-cavity

resonance will shift and hence affect the output performance. On the other hand, a Z-shaped telescopic cavity provides a large laser mode with a small amount of astigmatism with a laser propagation direction normal to the OPSL surface. This cavity can be designed to minimize thermal lensing and mode size fluctuation on the OPSL device for maintaining stable TEM₀₀ mode operation over a range of operating conditions. Furthermore, a design concept discussed below offers the ideal mode-selectivity characteristics of a confocal resonator [78].

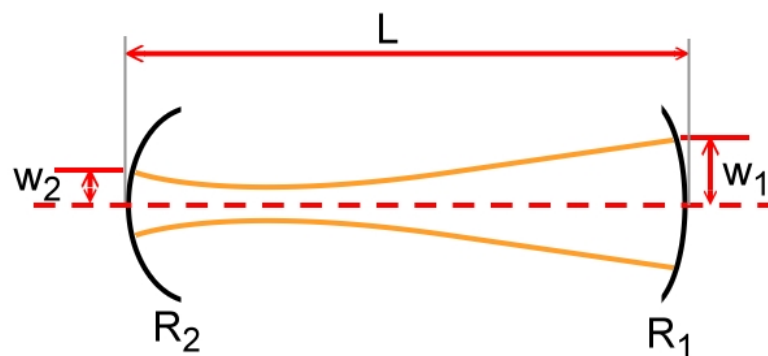


FIGURE 7.1 Linear optical resonator.

The standard expression for laser mode sizes w_1 and w_2 at mirrors 1 and 2 (with curvatures R_1 and R_2 , respectively) of an optical resonator, as shown in Fig. 7.1 is [79]:

$$w_1^2 = \frac{L\lambda}{\pi} \left(\frac{g_2}{g_1(1 - g_1g_2)} \right)^{\frac{1}{2}} \quad (7.1)$$

$$w_2^2 = \frac{L\lambda}{\pi} \left(\frac{g_1}{g_2(1-g_1g_2)} \right)^{\frac{1}{2}} \quad (7.2)$$

where L is the cavity length, $g_1=1-L/R_1$, and $g_2=1-L/R_2$. Assuming mirror 2 is the OPSL device, it can be shown from eq. (7.2) that the fractional change of spot size on the OPSL (dw_2/w_2) due to a fractional change (dg_2/g_2) is given by

$$\frac{dw_2}{w_2} = \frac{1}{4} \frac{(2g_1g_2 - 1)}{1 - g_1g_2} \frac{dg_2}{g_2} \quad (7.3)$$

When $g_1g_2=0.5$, the laser mode size on the OPSL becomes insensitive to variations of g_2 . This method is often used for compensating thermal lensing in solid state lasers. Although the thermal lensing effect is very small in the thin OPSL device, the Z-cavity design can not only minimize the mode size fluctuation but also achieve the confocal resonator characteristic, increasing mode selectivity.

Fig. 7.2 illustrates the telescopic Z-shaped cavity and its equivalent linear cavity. Mirror 2 is a distance l away from telescope mirror 2 and the end mirror (mirror 1) is a distance L away from telescope mirror 1. The two mirrors of the telescope are spaced by $d+\delta$ where d is the summation of the focal length of the telescope mirrors, f_{T1} and f_{T2} (Fig. 7.2) and δ is the telescope defocusing. The ABCD matrix for the telescope is expressed as

$$\begin{bmatrix} M - \frac{\delta}{f_1} & d + \delta \\ \frac{\delta}{f_1 f_2} & \frac{1}{M} - \frac{\delta}{f_2} \end{bmatrix} \quad (7.4)$$

This matrix can be rewritten as

$$\begin{bmatrix} 1 & -f_{T2} \\ 0 & 1 \end{bmatrix} \begin{bmatrix} 1 & 0 \\ -1/f_T & 1 \end{bmatrix} \begin{bmatrix} M & 0 \\ 0 & 1/M \end{bmatrix} \begin{bmatrix} 1 & -f_{T1} \\ 0 & 1 \end{bmatrix} \quad (7.5)$$

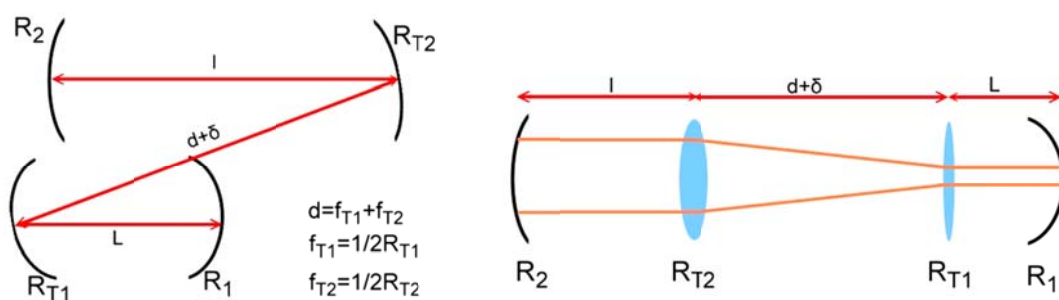


FIGURE 7.2 Left: Z-shaped telescopic resonator. Right: equivalent linear resonator.

The first and the last matrices in (7.5) represent the transfer matrix for space $-f_{T2}$ and $-f_{T1}$. The second matrix in (7.5) represents a thin lens with focal length f_T while the third matrix represents a thin telescope with magnification M where

$$M = -\frac{f_{T2}}{f_{T1}} \quad (7.6)$$

and the thin lens focal length

$$f_T = \frac{\delta}{f_{T2}^2} \quad (7.7)$$

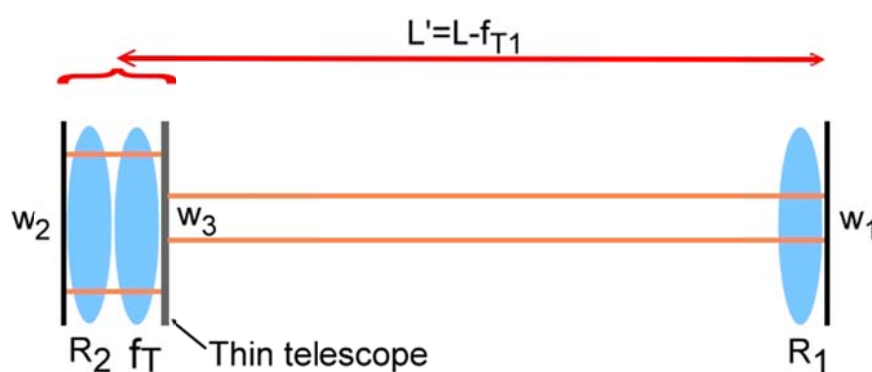


FIGURE 7.3 The equivalent telescopic resonator with a thin telescope and a thin lens f_T located at the mirror 2.

The end mirror in the optical resonator shown in Fig. 7.2 can be treated as a combination of a thin lens with focal length R_1 or R_2 plus a plane mirror. By choosing $l=f_{T2}$, the second telescope lens is adjacent to the end mirror 2 as shown in Fig. 7.3. The two lenses are treated as one compound lens of focal length R_2' where $1/R_2' = 1/f_T + 1/R_2$. Again, we

assume the OPSL device is mirror 2. In most cases, $1/R_2=0$ since thermal lensing effects are very small for OPSLs. This leads to $R_2'=f_T$.

We now have the equivalent linear telescopic resonator so we can write the single-pass ABCD matrix and find the g_1, g_2 parameter as:

$$g_1 = M\left(1 - \frac{L'}{R_1}\right) \quad (7.8)$$

$$g_2 = \frac{1}{M}\left(1 - \frac{M^2 L'}{R_2'}\right) \quad (7.9)$$

Also, the mode size on the OPSL device is given by [78]:

$$w_2^2 = \frac{\lambda}{\pi} \left(-\frac{AB}{CD}\right)^{1/2} = \frac{\lambda}{\pi} \left(\frac{g_1 M^2 L'^2}{g_2 (1 - g_1 g_2)}\right)^{1/2} \quad (7.10)$$

where A,B,C,D are elements in the single-pass ABCD matrix of the telescopic resonator and $L'=L-f_{T1}$. Since M, R_1 , f_{T1} , and f_{T2} are known the relationship between L and w_2 can be obtained from (7.10). Then, δ can be obtained by applying the condition, $g_1 g_2=0.5$ to equation (7.8) and (7.9) so the distance between the two telescope elements can be obtained accordingly.

The red curve in Fig. 7.4 shows the relation between the distance L and the mode diameter ($2 \times w_2$) on the OPSL device and the blue curve is the corresponding distance between the two telescope mirrors for each distance L for the condition $g_1 g_2 = 0.5$. The radius of curvature R_{T1} of the first mirror of the telescope is 50 mm and the radius of curvature R_{T2} of the second mirror of the telescope is 350 mm. Both mirrors have high reflectivity at the laser wavelength at 1040 nm. The end mirror R_1 is a flat mirror with 4% transmission at 1040 nm. For each pump spot size, we chose a proper L to match the mode size to the pump size and then the distance between the two telescope mirrors is decided based on the blue curve.

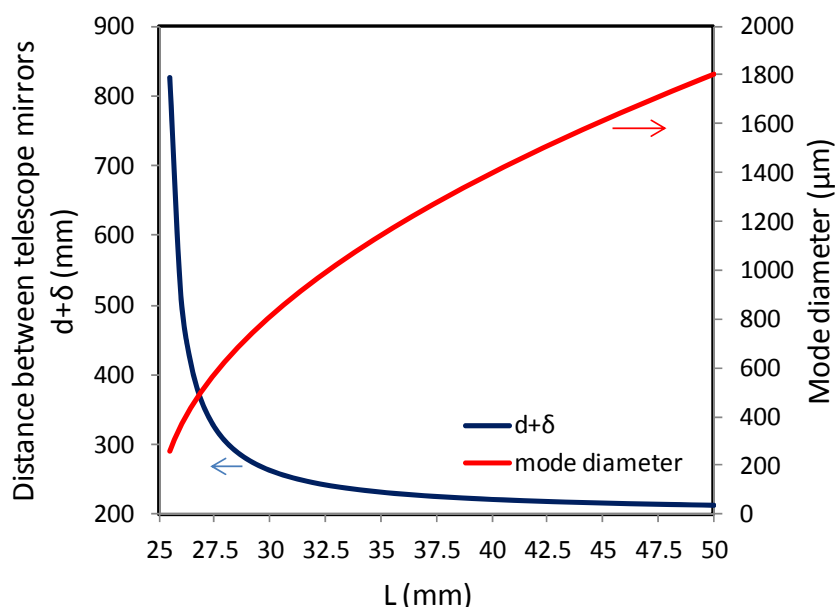


FIGURE 7.4 The telescope mirror spacing and corresponding mode diameter vs. L for $g_1 g_2 = 0.5$. The radii of curvature for R_{T1} , R_{T2} and R_1 are 50 mm, 350 mm, and infinity, respectively.

7.2 Experimental Setup

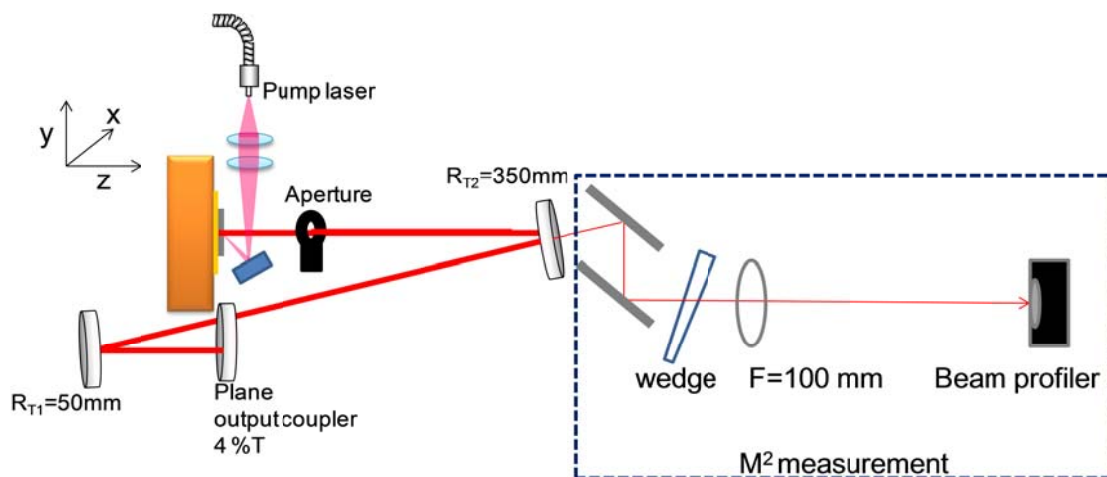


FIGURE 7.5 Experimental setup for the OPSL in TEM₀₀ mode operation

Fig. 7.5 shows the experimental setup used in this experiment. The chiller temperature was set at 10 °C. The optical resonator configuration follows the design concept described above. Three pump spot diameters, 590 μm, 730 μm and 880 μm were used. The folding angle at the telescope mirrors was about 15°. This folding angle introduces small amounts of astigmatism so the resulting mode size in the x-direction (sagittal) is slightly larger than that in the y-direction (tangential). In order to match the elliptical mode shape, we make the pump spot diameter larger in the x-direction. Fig. 7.6 shows the pump spot diameter in two directions at the image plane/OPSL surface and also the designed mode diameter. The pump diameter ($1/e^2$) is about the same size as the designed mode diameter in the x-direction while the pump is slightly larger than the

mode size in the y-direction. From Fig. 7.4, a mode size below 600 μm requires over 30 cm spacing between the two telescope mirrors. In order to decrease the length of the cavity, we use $R_{T2}=200$ mm to match the pump spot size of 590 μm .

The laser light leaking from the second telescope mirror is focused by a 100 mm focal length for an M^2 measurement. The M^2 factor is a parameter for determining the degree of beam divergence. A perfect TEM_{00} beam has an $M^2=1$. It can be calculated from the measured evolution of the beam widths ($D4\sigma$ beam widths) along the propagation direction [80]. We use a Spiricon beam profiler to determine the $D4\sigma$ beam widths. Half of the data points were measured within a Rayleigh length and half of the measurement points were more than two Rayleigh lengths away from the beam focus. In the experiment, we observed a second peak appearing in the laser spectrum at high pump power, indicating the presence of higher order modes although there was no obvious change in beam profile observed from the beam profiler. In order to eliminate the higher order mode, a hard aperture was placed inside the cavity as shown in Fig. 7.5.

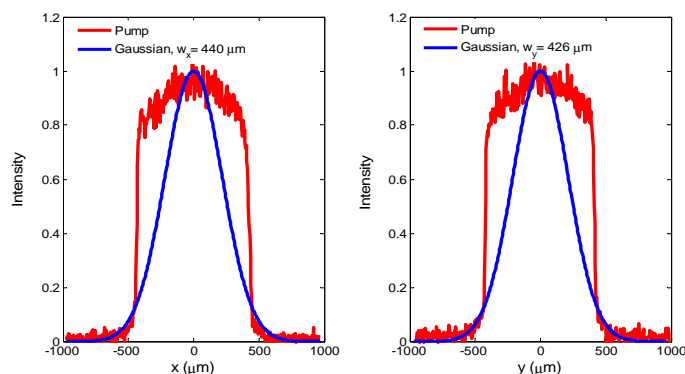


FIGURE 7.6 Left: pump and the cavity mode profile in the x-direction. Right: pump and the cavity mode profile in the y-direction.

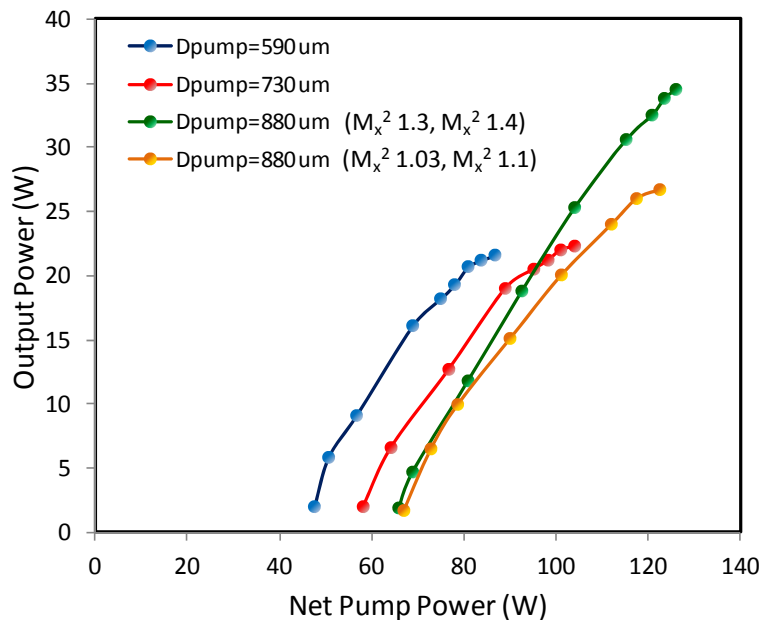


FIGURE 7.7 Input-output curves of the OPSL device with pump diameter $D_{\text{pump}}=590$, 730 and 880 μm .

7.3 Results and Discussion

In the experiment, the beam quality was determined by observing the laser spectrum and the beam profile at one Rayleigh length away from the focus of the laser light leaking from the folding mirror. The CW output power curves for the OPSL with the three mode sizes are shown in Fig. 7.7. Since the OPSL device is processed from structure C which has a fairly large detuning between the QW gain and the micro-cavity resonance, the threshold pump power is high. For the 590 μm pump spot, the threshold is about 45 W and it is about 67 W for the 880 μm pump spot. The maximum achieved output power is 22 W, 23 W and 27 W for the OPSL with 590, 730 and 880 μm pump spot. The power scalability of the OPSL in TEM_{00} mode operation is fairly poor. The

pump area is increased more than twice but the output power only increases 23%, heating issues seem to be more significant in TEM₀₀ mode operation. Since the intensity maximum of the TEM₀₀ mode is at the center of the pump spot, the temperature is highest there. In Chapter 3, we showed that the central temperature of the pump area inside the active region increases with the pump spot size. For a large pump area, the center reaches the roll-over temperature at a much lower pump power density and the power of TEM₀₀ mode stops increasing. On the other hand, the output power of the OPSL operating in multi-transverse mode can keep increasing while the center part has already shut-off.

With a hard aperture inside the cavity, the M² of the 27 W OPSL is 1.03 in the x-direction and 1.1 in the y-direction as shown in Fig. 7.8. This is a very high quality beam, M²=1 is almost never achieved in practice. By enlarging the aperture, the output power increases to 34.5 W at a pump power of 126 W where the OPSL with a hard aperture has 27 W output power. This pump power is also very close to the pump limit. The M² of this 34.5 W beam is about 1.3 and 1.4 for the x and y-direction. Although the OPSL did not show thermal roll-over at 34.5 W, we did not try to pump it harder. From Fig. 7.8, the two power curves for the 880 μm pump spot overlap each other below 10 W of output power. Beyond this point, the output power difference between the two conditions increases indicating that more and more power from higher order modes is contributed to the output power of the OPSL with a larger aperture. A much higher M² is expected for the OPSL output when thermal roll-over occurs.

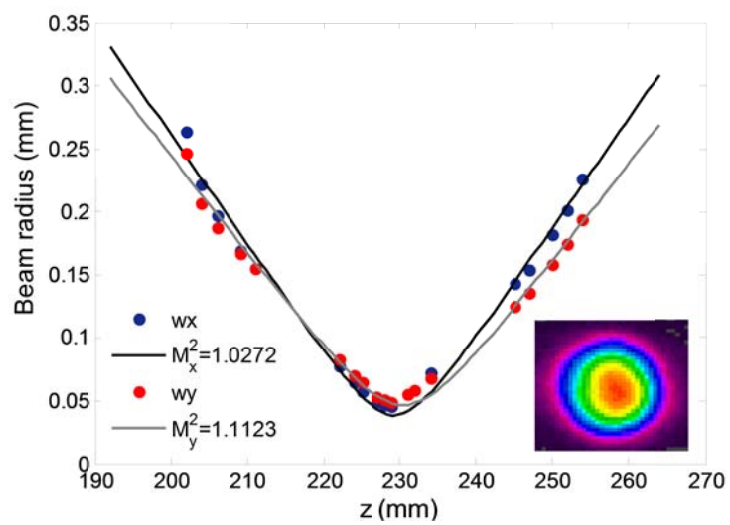


FIGURE 7.8 M^2 fitting of the 27 W OPSL beam. Inset: intensity profile of the OPSL beam.

CHAPTER 8 CONCLUSION AND OUTLOOK

Optimized high-power operation of OPSLs for targeted wavelengths requires proper wafer design, precise wafer growth, careful device fabrication and good thermal management. Strategies for improving thermal management and laser efficiency were realized in this thesis. Record output power performance was achieved in CW and pulsed operation.

The OPSL structure used in this thesis is a barrier pumped, bottom emitter. The design concept of this structure is to achieve effective gain enhancement by placing QWs at the standing wave antinodes of the designed laser wavelength and matching the micro-cavity resonance to the QW gain peak at the designed wavelength. For improving thermal management, we established an advanced bonding facility and technique. A 6 μm thick evaporated indium layer was used to bond the OPSL chip on a diamond heat spreader in a vacuum chamber. A near void-free solder junction was achieved with this bonding technique. We also developed a reliable chemical etching process to ensure a uniform and smooth surface for power scaling.

We utilized the concept of power scaling by increasing the pump area while maintaining a constant power density to obtain a higher output power. However, the power scalability is limited by device heating. The temperature rise inside the active region increases with the pump spot size for a constant power density. To improve the thermal management, a systematic thermal analysis was performed in this thesis. First, we improved the heat sinking by decreasing the nozzle diameter inside the impinging jet

heat sink. More than 20% increase in the heat transfer coefficient was obtained and this improvement reflects a 3~4 °C reduction of the device temperature. Second, the influence of the pump intensity profile on the temperature rise was investigated. The simulation showed a much lower temperature in the active region for the device pumped by a top-hat like beam. In the experiment, improved output performance was achieved from the altered pump laser profile by bending its output fiber. This causes the beam to be more top-hat like. Then, we also optimized the dimensions of the diamond heat spreader and the copper submount. With an increase of the diamond thickness/width, the degree of heat spreading increases and a lower temperature rise is calculated. We found that the copper submount also has a heat-spreading function, so a lower temperature rise was obtained from a thicker copper submount. Finally, we analyzed a new design of the copper submount which allows for side cooling the OPSL device, with 8 °C of temperature reduction predicted by the simulation.

One strategy we used to obtain high output power was to use the OPSL structure with a larger negative detuning at room temperature. A larger negative detuning at room temperature requires higher threshold pump power because of the spectral misalignment between the QW gain and the micro-cavity of the cold device. A larger negative detuning also leads to a higher optimal operation temperature and a higher roll-over temperature. This increases the high-temperature tolerance of the device so a higher output power is expected. We investigated this influence by comparing the output performance of three OPSL devices with different amounts of negative detuning, specifically 12 nm, 18 nm and 34 nm. The maximum achieved output power obtained from the 3 devices was 23 W,

57 W and 73 W, respectively. The OPSL structure with 34 nm negative detuning demonstrated better high-temperature tolerance and output performance so this structure was used for the power scaling experiment. We scaled the pump spot diameter from 750 μm to 1170 μm ($1/e^2$), but the laser cavity mode was fixed at about 217 μm . Therefore, the OPSL operated in multi-transverse mode. With the improved thermal management, 103 W of output power from a single OPSL device was achieved using a 1170 μm pump spot. This is the first demonstration of OPSLs with an output power over 100 W. For fundamental mode operation, we used a z-shaped telescopic resonator to increase the cavity mode volume to $880 \times 852 \mu\text{m}$ for matching the pump spot diameter of $880 \times 866 \mu\text{m}$. With the intra-cavity aperture, 34.5 W output power was achieved with beam quality $M^2 \approx 1.4$ in the tangential and 1.3 in the sagittal direction. By reducing the aperture, the output beam quality was improved to 1.1 in the tangential and 1.03 in the sagittal direction, with 27 W CW output power was achieved.

To improve optical efficiency, we utilized a double pass pump scheme without increasing the complexity in the design and the growth. An Au-In alloy layer was deposited on the back of the DBR which is transparent to the pump, to reflect the pump back through the structure for a second pass. Optical efficiency was improved from 25 % without double-passing the pump to 42 % with the double-pass pump design. The double pass pump strategy not only increases optical efficiency but also reduces the temperature of the device since there is less heating due to absorption of the pump in the DBR or the Cr layer. Therefore, over 100 % improvement in output power was achieved in the experiment. We also designed a new pump anti-reflection coating which has an optical

thickness of three fourths of the pump wavelength to eliminate the pump reflection and retain the micro-cavity effect. With respect to the total incident power, 39% maximum optical-to-optical efficiency was achieved.

The output performance of OPSLs in pulsed operation was also investigated. By pulsed pumping the OPSL device, output power was significantly increased because of reduction of the average heating power. A maximum peak power over 270 W was achieved using 750 ns pump pulses from the alexandrite laser.

In this thesis, we have demonstrated a high power OPSL as a pathway to developing kilowatt-level high-brightness, high-power semiconductor lasers. However, the strategies for the improvement in output power and in efficiency were realized separately. The next step of OPSL optimization should integrate these strategies together, including optimization of detuning, double pass pump design and the PARC. The technique of over-etching the cap lay to shift the micro-cavity resonance could also be used to optimize the detuning between the QW gain and the micro-cavity resonance. With the increase of optical efficiency, we hope the threshold pump power can be reduced. Another possible optimization would be beam-shaping the pump beam to generate a donut-shaped profile. From a thermal management point of view, a donut-shaped profile can compensate for the overheating at the center of the pump beam and extend the power scalability of OPSLs. The trade-off of this strategy would be the reduction of the carrier density at the center of the pump area. This may affect the output performance of the OPSL in the fundamental transverse mode operation. Therefore, careful optimizations of the central intensity and the size of the donut hole are extremely

important to realize benefit from this strategy.

REFERENCES

1. R. N. Hall, G. E. Fenner, J. D. Kingsley, T. J. Soltys, and R. O. Carlson, "Coherent Light Emission From GaAs Junctions," *Phys. Rev. Lett.* **9**, 366-368 (1962).
2. H. Kroemer, "A proposed class of hetero-junction injection lasers," *Proceedings of the IEEE* **51**, 1782-1783 (1963).
3. Alferov, Zh. I., V. M. Andreev, D. Z. Garbuzov, Yu. V. Zhilyaev, E. P. Morozov, E. L. Portnoi, and V. G. Triofim, "Investigation of the Influence of the AlAs-GaAs Heterostructure Parameters on the Laser Threshold Current and the Realization of Continuous Emission at Room Temperature," *Sov. Phys. Semicond.* **4**, 1573 (1971).
4. U.S. Patent 3,982,207, Raymond Dingle, and Charles Howard Henry, "Quantum effects in heterostructure lasers," (1975).
5. N. Peyghambarian, S. W. Koch, and A. Mysyrowicz, *Introduction to semiconductor optics* (Prentice-Hall, Inc, 1993).
6. C. H. Henry, P. M. Petroff, R. A. Logan, and F. R. Merritt, "Catastrophic damage of $\text{Al}_x\text{Ga}_{1-x}\text{As}$ double-heterostructure laser material," *Journal of Applied Physics* **50**, 3721-3732 (1979).
7. Hassaun A. Jones-Bey, "NECSEL technology unveiled at OFC," *Laser Focus World*, published May 1st, 2001.
8. J. G. McInerney, A. Mooradian, A. Lewis, A. V. Shchegrov, E. M. Strzelecka, D. Lee, J. P. Watson, M. Liebman, G. P. Carey, B. D. Cantos, W. R. Hitchens, and D. Heald, "High-power surface emitting semiconductor laser with extended vertical compound cavity," *Electronics Letters* **39**, 523-525 (2003).
9. M. Kuznetsov, F. Hakimi, R. Sprague, and A. Mooradian, "High-power (>0.5-W CW) diode-pumped vertical-external-cavity surface-emitting semiconductor lasers with circular TEM_{00} beams," *Photonics Technology Letters, IEEE* **9**, 1063-1065 (1997).
10. A. Garnache, A. A. Kachanov, F. Stoeckel, and R. Planel, "High-sensitivity intracavity laser absorption spectroscopy with vertical-external-cavity surface-emitting semiconductor lasers," *Opt. Lett.* **24**, 826-828 (1999).

11. E. Bertseva, A. A. Kachanov, and A. Campargue, "Intracavity laser absorption spectroscopy of N₂O with a vertical external cavity surface emitting laser," *Chemical Physics Letters* **351**, 18-26 (2002).
12. J. Paul, Y. Kaneda, T. Wang, C. Lytle, J. V. Moloney, and R. J. Jones, "Doppler-free spectroscopy of mercury at 253.7 nm using a high-power, frequency-quadrupled, optically pumped external-cavity semiconductor laser," *Opt. Lett.* **36**, 61-63 (2011).
13. B. Cocquelin, G. Lucas-Leclin, P. Georges, I. Sagnes, and A. Garnache, "Design of a low-threshold VECSEL emitting at 852 nm for Cesium atomic clocks," *Optical and Quantum Electronics* **40**, 167-173 (2008).
14. E. Esposito, S. Keatings, K. Gardner, J. Harris, E. Riis, and G. McConnell, "Confocal laser scanning microscopy using a frequency doubled vertical external cavity surface emitting laser," *Rev. Sci. Instrum.* **79**, 083702 (2008).
15. J. Chilla, H. Zhou, E. Weiss, A. Caprara, Q. Shou, S. Govorkov, M. Reed, and L. Spinelli, "Blue and green optically pumped semiconductor lasers for display," *Proc. SPIE* **5740**, 41-7 (2005).
16. M. Y. A. Raja, S. R. J. Brueck, M. Osinski, C. F. Schaus, J. G. McInerney, T. M. Brennan, and B. E. Hammons, "Resonant periodic gain surface-emitting semiconductor lasers," *Quantum Electronics, IEEE Journal of* **25**, 1500-1512 (1989).
17. M. Kuznetsov, "VECSEL Semiconductor Lasers: A Path to High-Power, Quality Beam and UV to IR Wavelength by Design," in *Semiconductor Disk Lasers*, Anonymous (Wiley-VCH Verlag GmbH & Co. KGaA, 2010), pp. 1-71.
18. Y. Kaneda, J. M. Yarborough, L. Li, N. Peyghambarian, L. Fan, C. Hassenius, M. Fallahi, J. Hader, J. V. Moloney, Y. Honda, M. Nishioka, Y. Shimizu, K. Miyazono, H. Shimatani, M. Yoshimura, Y. Mori, Y. Kitaoka, and T. Sasaki, "Continuous-wave all-solid-state 244 nm deep-ultraviolet laser source by fourth-harmonic generation of an optically pumped semiconductor laser using CsLiB₆O₁₀ in an external resonator," *Opt. Lett.* **33**, 1705-1707 (2008).
19. M. Fallahi, Li Fan, Y. Kaneda, C. Hassenius, J. Hader, Hongbo Li, J. V. Moloney, B. Kunert, W. Stolz, S. W. Koch, J. Murray, and R. Bedford, "5-W Yellow Laser by Intracavity Frequency Doubling of High-Power Vertical-External-Cavity Surface-Emitting Laser," *Photonics Technology Letters, IEEE* **20**, 1700-1702 (2008).

20. L. E. Hunziker, C. Ihli, and D. S. Steingrube, "Miniaturization and Power Scaling of Fundamental Mode Optically Pumped Semiconductor Lasers," *Selected Topics in Quantum Electronics, IEEE Journal of* **13**, 610-618 (2007).
21. J. Chilla, S. Butterworth, A. Zeitschel, J. Charles, A. Caprara, M. Reed, and L. Spinelli, "High-power optically pumped semiconductor lasers," *Proc. SPIE* **5332**, 143-8 (2004).
22. Ki-Sung Kim, Jaeryung Yoo, Gibum Kim, Sangmoon Lee, Soohaeng Cho, Junyoun Kim, Taek Kim, and Yongjo Park, "920-nm Vertical-External-Cavity Surface-Emitting Lasers With a Slope Efficiency of 58% at Room Temperature," *Photonics Technology Letters, IEEE* **19**, 1655-1657 (2007).
23. J. Chilla, Q. Shu, H. Zhou, E. Weiss, M. Reed, and L. Spinelli, "Recent advances in optically pumped semiconductor lasers," *Proc. SPIE* **6451**, 645109-10 (2007).
24. B. Rudin, A. Rutz, M. Hoffmann, D. J. H. C. Maas, A. - Bellancourt, E. Gini, T. Suidmeyer, and U. Keller, "Highly efficient optically pumped vertical-emitting semiconductor laser with more than 20 W average output power in a fundamental transverse mode," *Opt. Lett.* **33**, 2719-2721 (2008).
25. F. Demaria, S. Lorch, S. Menzel, M. C. Riedl, F. Rinaldi, R. Rosch, and P. Unger, "Design of Highly Efficient High-Power Optically Pumped Semiconductor Disk Lasers," *Selected Topics in Quantum Electronics, IEEE Journal of* **15**, 973-977 (2009).
26. L. Fan, M. Fallahi, J. Hader, A. R. Zakharian, J. V. Moloney, J. T. Murray, R. Bedford, W. Stolz, and S. W. Koch, "Multichip vertical-external-cavity surface-emitting lasers: a coherent power scaling scheme," *Opt. Lett.* **31**, 3612-3614 (2006).
27. E. J. Saarinen, A. Harkonen, S. Suomalainen, and O. G. Okhotnikov, "Power scalable semiconductor disk laser using multiple gain cavity," *Opt. Express* **14**, 12868-12871 (2006).
28. L. Hunziker, Q. Shu, D. Bauer, C. Ihli, G. Mahnke, M. Rebut, J. Chilla, A. Caprara, H. Zhou, E. Weiss, and M. Reed, "Power-scaling of optically pumped semiconductor lasers," *Proc. SPIE* **6451**, 64510A-6 (2007).
29. H. Lindberg, M. Strassner, E. Gerster, and A. Larsson, "0.8 W optically pumped vertical external cavity surface emitting laser operating CW at 1550 nm," *Electronics Letters* **40**, 601-602 (2004).

30. J. Rautiainen, J. Lyytikäinen, A. Sirbu, A. Mereuta, A. Caliman, E. Kapon, and O. G. Okhotnikov, "2.6 W optically-pumped semiconductor disk laser operating at 1.57 μm using wafer fusion," *Opt.Express* **16**, 21881-21886 (2008).
31. M. Rattunde, N. Schulz, C. Ritzenthaler, B. Rösener, C. Manz, K. Köhler, E. Wörner, and J. Wagner, "High brightness GaSb-based optically pumped semiconductor disk lasers at 2.3 μm ," *Proc. SPIE* **6479**, 647915-10 (2007).
32. T. J. Rotter, J. Tatebayashi, P. Senanayake, G. Balakrishnan, M. Rattunde, J. Wagner, J. Hader, J. V. Moloney, S. W. Koch, L. R. Dawson, and D. L. Huffaker, "Continuous-Wave, Room-Temperature Operation of 2- μm Sb-Based Optically-Pumped Vertical-External-Cavity Surface-Emitting Laser Monolithically Grown on GaAs Substrates," *Applied Physics Express* **2**, 112102 (2009).
33. Yi-Ying Lai, J. M. Yarborough, Y. Kaneda, J. Hader, J. V. Moloney, T. J. Rotter, G. Balakrishnan, C. Hains, and S. W. Koch, "340-W Peak Power From a GaSb 2- μm Optically Pumped Semiconductor Laser (OPSL) Grown Mismatched on GaAs," *Photonics Technology Letters, IEEE* **22**, 1253-1255 (2010).
34. M. Rahim, M. Fill, F. Felder, D. Chappuis, M. Corda, and H. Zogg, "Mid-infrared PbTe vertical external cavity surface emitting laser on Si-substrate with above 1 W output power," *Appl. Phys. Lett.* **95**, 241107 (2009).
35. A. Khiar, M. Rahim, M. Fill, F. Felder, F. Hobrecker, and H. Zogg, "Continuously tunable monomode mid-infrared vertical external cavity surface emitting laser on Si," *Appl. Phys. Lett.* **97**, 151104 (2010).
36. G. B. Kim, J. Kim, J. Lee, J. Yoo, K. Kim, S. Lee, S. Cho, S. Lim, T. Kim, and Y. Park, "End-pumped green and blue vertical external cavity surface emitting laser devices," *Applied Physics Letters* **89**, 181106-181106-3 (2006).
37. V. Ostroumov, C. Simon, H. Schwarze, R. von Elm, W. Seelert, and J. Lindfors, "1 W 488 nm cw air-cooled optically pumped semiconductor laser," *Proc. SPIE* **6871**, 687118-7 (2008).
38. L. Fan, M. Fallahi, J. Hader, A. R. Zakharian, J. V. Moloney, J. T. Murray, R. Bedford, S. W. Koch, and W. Stolz, "Tunable High-Power Blue-Green Laser Based on Intracavity Frequency Doubling of a Diode-Pumped Vertical-External-Cavity Surface-Emitting Laser," in *Advanced Solid-State Photonics*, Anonymous (Optical Society of America, 2007), pp. MD5.

39. A. V. Mule, E. N. Glytsis, T. K. Gaylord, and J. D. Meindl, "Electrical and optical clock distribution networks for gigascale microprocessors," *Very Large Scale Integration (VLSI) Systems*, IEEE Transactions on **10**, 582-594 (2002).
40. E. Cassan, D. Marris, M. Rouviere, L. Vivien, and S. Laval, "Comparison between electrical and optical global clock distributions for CMOS integrated circuits," *Opt. Eng.* **44**, 105402 (2005).
41. D. A. B. Miller, "Rationale and challenges for optical interconnects to electronic chips," *Proceedings of the IEEE* **88**, 728-749 (2000).
42. S. Hoogland, S. Dhanjal, A. C. Tropper, J. S. Roberts, R. Haring, R. Paschotta, F. Morier-Genoud, and U. Keller, "Passively mode-locked diode-pumped surface-emitting semiconductor laser," *Photonics Technology Letters*, IEEE **12**, 1135-1137 (2000).
43. M. Scheller, T. -. Wang, B. Kunert, W. Stolz, S. W. Koch, and J. V. Moloney, "Passively modelocked VECSEL emitting 682 fs pulses with 5.1W of average output power," *Electronics Letters* **48**, 588-589 (2012).
44. D. J. H. C. Maas, A. -. Bellancourt, B. Rudin, M. Golling, H. J. Unold, T. Südmeyer, and U. Keller, "Vertical integration of ultrafast semiconductor lasers," *Applied Physics B: Lasers and Optics* **88**, 493-497 (2007).
45. B. Rudin, V. J. Wittwer, D. J. H. C. Maas, M. Hoffmann, O. D. Sieber, Y. Barbarin, M. Golling, T. Südmeyer, and U. Keller, "High-power MIXSEL: an integrated ultrafast semiconductor laser with 6.4 W average power," *Opt. Express* **18**, 27582-27588 (2010).
46. P. Yeh, *Optical waves in layered media* (Wiley, 2005).
47. S. -. Beyertt, M. Zorn, T. Kubler, H. Wenzel, M. Weyers, A. Giesen, G. Trankle, and U. Brauch, "Optical in-well pumping of a semiconductor disk laser with high optical efficiency," *Quantum Electronics*, IEEE Journal of **41**, 1439-1449 (2005).
48. S. -. Beyertt, U. Brauch, F. Demaria, N. Dhidah, A. Giesen, T. Kubler, S. Lorch, F. Rinaldi, and P. Unger, "Efficient Gallium–Arsenide Disk Laser," *Quantum Electronics*, IEEE Journal of **43**, 869-875 (2007).
49. N. Schulz, M. Rattunde, C. Ritzenthaler, B. Rösener, C. Manz, K. Köhler, J. Wagner, and U. Brauch, "Resonant optical in-well pumping of an (AlGaIn)(AsSb)-based vertical-external-cavity surface-emitting laser emitting at 2.35 μm ," *Appl. Phys. Lett.* **91**, 091113-3 (2007).

50. J. Hader, J. V. Moloney, S. W. Koch, and W. W. Chow, "Microscopic modeling of gain and luminescence in semiconductors," *Selected Topics in Quantum Electronics, IEEE Journal of* **9**, 688-697 (2003).
51. J. Hader, S. W. Koch, and J. V. Moloney, "Microscopic theory of gain and spontaneous emission in GaInNAs laser material," *Solid-State Electronics* **47**, 513-521 (2003).
52. W. W. Chow, A. Knorr, S. Hughes, A. Girndt, and S. W. Koch, "Carrier correlation effects in a quantum-well semiconductor laser medium," *Selected Topics in Quantum Electronics, IEEE Journal of* **3**, 136-141 (1997).
53. SimuLase Software, Nonlinear Control Strategies, Inc., [Online]. Available: <http://www.nlcstr.com>.
54. S. Calvez, A. H. Clark, J. - Hopkins, R. Macaluso, P. Merlin, H. D. Sun, M. D. Dawson, T. Jouhti, and M. Pessa, "1.3 μm GaInNAs optically-pumped vertical cavity semiconductor optical amplifier," *Electronics Letters* **39**, 100-102 (2003).
55. A. Garnache, A. A. Kachanov, F. Stoeckel, and R. Houdre, "Diode-pumped broadband vertical-external-cavity surface-emitting semiconductor laser applied to high-sensitivity intracavity absorption spectroscopy," *J Opt Soc Am B* **17**, 1589-1598 (2000).
56. J. Hader, G. Hardesty, Tsuei-Lian Wang, M. J. Yarborough, Y. Kaneda, J. V. Moloney, B. Kunert, W. Stolz, and S. W. Koch, "Predictive Microscopic Modeling of VECSELs," *Quantum Electronics, IEEE Journal of* **46**, 810-817 (2010).
57. M. Schafer, W. Hoyer, M. Kira, S. W. Koch, and J. V. Moloney, "Influence of dielectric environment on quantum-well luminescence spectra," *J Opt Soc Am B* **25**, 187-195 (2008).
58. M. Kira, F. Jahnke, and S. W. Koch, "Quantum Theory of Secondary Emission in Optically Excited Semiconductor Quantum Wells," *Phys. Rev. Lett.* **82**, 3544-3547 (1999).
59. J. Hader, A. R. Zakharian, J. V. Moloney, T. R. Nelson, W. J. Siskaninetz, J. E. Ehret, K. Hantke, M. Hofmann, and S. W. Koch, "Quantitative prediction of semiconductor laser characteristics based on low intensity photoluminescence measurements," *Photonics Technology Letters, IEEE* **14**, 762-764 (2002).

60. A. C. Tropper and S. Hoogland, "Extended cavity surface-emitting semiconductor lasers," *Progress in Quantum Electronics* **30**, 1-43 (2006).
61. W. W. Chow and S. W. Koch, *Semiconductor-Laser Fundamentals: Physics of the Gain Materials* (Springer, 1999).
62. O. G. Okhotnikov, *Semiconductor Disk Lasers: Physics and Technology* (John Wiley & Sons, 2010).
63. A. Haug, "Relations between the T_0 values of bulk and quantum-well GaAs," *Applied Physics B: Lasers and Optics* **44**, 151 (1987).
64. J. Hader, J. V. Moloney, and S. W. Koch, "Temperature Dependence of Radiative and Auger Losses in Quantum Wells," *Quantum Electronics, IEEE Journal of* **44**, 185-191 (2008).
65. A. Haug, "Auger recombination in direct-gap semiconductors: band-structure effects," *Journal of Physics C: Solid State Physics* **16**, 4159 (1983).
66. C. Long, *Essential Heat Transfer* (Longman, 1999).
67. F. P. Incropera, *Liquid cooling of electronic devices by single-phase convection* (Wiley, 1999).
68. B. Elison and B. W. Webb, "Local heat transfer to impinging liquid jets in the initially laminar, transitional, and turbulent regimes," *Int. J. Heat Mass Transfer* **37**, 1207-1216 (1994).
69. R. Gardon and J. C. Akfirat, "The role of turbulence in determining the heat-transfer characteristics of impinging jets," *Int. J. Heat Mass Transfer* **8**, 1261-1272 (1965).
70. M. Chaudhari, B. Puranik, and A. Agrawal, "Heat transfer characteristics of synthetic jet impingement cooling," *Int. J. Heat Mass Transfer* **53**, 1057-1069 (2010).
71. B. W. Webb and C. - . Ma, "Single-Phase Liquid Jet Impingement Heat Transfer," in James P. Hartnett and Thomas F. Irvine, eds. (Elsevier, 1995), pp. 105.
72. T. - . Wang, B. Heinen, C. Dineen, M. Sparenberg, A. Weber, B. Kunert, S. W. Koch, J. V. Moloney, M. Koch, and W. Stolz, "Quantum Design Strategy pushes High-Power Vertical External Cavity Surface Emitting Lasers beyond 100W," submitted (2012).

73. Tsuei-Lian Wang, Y. Kaneda, J. M. Yarborough, J. Hader, J. V. Moloney, A. Chernikov, S. Chatterjee, S. W. Koch, B. Kunert, and W. Stolz, "High-Power Optically Pumped Semiconductor Laser at 1040 nm," *Photonics Technology Letters, IEEE* **22**, 661-663 (2010).
74. B. Heinen, T. -. Wang, M. Sparenberg, A. Weber, B. Kunert, J. Hader, S. W. Koch, J. V. Moloney, M. Koch, and W. Stolz, "106 W continuous-wave output power from vertical-external-cavity surface-emitting laser," *Electronics Letters* **48**, 516-517 (2012).
75. A. Laurain, Tsuei-Lian Wang, M. J. Yarborough, J. Hader, J. V. Moloney, S. W. Koch, B. Kunert, and W. Stolz, "High Peak Power Operation of a 1- μ m GaAs-Based Optically Pumped Semiconductor Laser," *Photonics Technology Letters, IEEE* **24**, 380-382 (2012).
76. B. J.D., A. D.W., C. A., C. J.L., G. S.V., L. A.Y., M. W., S. Q.-Z., and S. L., "20 Watt CW TEM₀₀ intracavity doubled optically pumped semiconductor laser at 532 nm," in *Society of Photo-Optical Instrumentation Engineers (SPIE) Conference Series*, Anonymous (, 2012).
77. A. Harkonen, S. Suomalainen, E. Saarinen, L. Orsila, R. Koskinen, O. Okhotnikov, S. Calvez, and M. Dawson, "4 W single-transverse mode VECSEL utilising intra-cavity diamond heat spreader," *Electronics Letters* **42**, 693-694 (2006).
78. D. C. Hanna, C. G. Sawyers, and M. A. Yuratich, "Telescopic resonators for large-volume TEM₀₀-mode operation," *Optical and Quantum Electronics* **13**, 493-507 (1981).
79. H. KOGELNIK and T. LI, "Laser Beams and Resonators," *Appl. Opt.* **5**, 1550-1567 (1966).
80. A. E. Siegman, "How to (Maybe) Measure Laser Beam Quality," in *DPSS (Diode Pumped Solid State) Lasers: Applications and Issues*, Anonymous (Optical Society of America, 1998), pp. MQ1.